STRUCTURE-FUNCTION ANALYSIS OF VASCULAR TETHERING MOLECULES USING ATOMIC FORCE MICROSCOPE

A Thesis
Presented to
The Academic Faculty

by

Tao Wu

In Partial Fulfillment
of the Requirements for the Degree
DOCTOR OF PHILOSOPHY IN BIOENGINEERING in the
School of MECHANICAL ENGINEERING

Georgia Institute of Technology
DECEMBER 2008

STRUCTURE-FUNCTION ANALYSIS OF VASCULAR TETHERING MOLECULES USING ATOMIC FORCE MICROSCOPE

Approved by:

Dr. Cheng Zhu, Advisor
Department of Biomedical Engineering
Georgia Institute of Technology

Dr. Rodger P. McEver
Cardiovascular Biology Research Program
Oklahoma Medical Research Foundation

Dr. Bridgette Barry
School of Chemistry and Biochemistry
Georgia Institute of Technology

Dr. Larry V. McIntire
Department of Biomedical Engineering
Georgia Institute of Technology

Dr. Barbara D. Boyan
Department of Biomedical Engineering
Georgia Institute of Technology

Date Approved: Nov 14, 2008

ACKNOWLEDGEMENTS

I would like to thank Dr. Cheng Zhu, my advisor, for his patient guidance, strong support, and encouragement, without which I would not be here. I would also like to acknowledge the support and suggestions of my reading committee, Dr. Bridgette Barry, Dr. Barbara Boyan, Dr. Rodger McEver, and Dr. Larry McIntire. Special thanks are directed towards Dr. Rodger McEver, Dr. Larry McIntire, Dr. Jóse Lopéz, Dr. Miguel Cruz, and Dr. Jingfei Dong for providing reagents and insight necessary for this thesis. I would like to thank Dr. Jizhong Lou for many valuable and interesting discussions with him. I would like to thank Dr. Jeffrey Donnell for the proofreading. I would also like to thank Fang Kong for his help with the AFM force clamp program and Jiangguo Lin for his help with the ADAMTS13 cleavage data analysis.

I would like to thank my wife and my parents for their love and constant support being with me through these years.

I enjoyed my years as a grad student in Zhu lab because of all the incredible people around me. I would like to thank all my labmates and friends in IBB for making the AFM lab a place I enjoyed coming to every day.

TABLE OF CONTENTS

LIST OF FIGURES

LIST OF SYMBOLS

T	Temperature
F	Force
K_{off}	Reverse rate OR off-rate
K_{off}^{o}	Reverse rate with no force applied
t	Lifetime of bond or structure strength

LIST OF ABBREVIATIONS

GSP	Glycosulfopeptide
PNAd	Peripheral Node Addressin
PSGL-1	P-selectin Glycoprotein-1
GPIb	Glycoprotein Ib
VWF	von Willebrand Factor
VWD	von Willebrand Disease
ULVWF	Ultra-large von Willebrand Factor
AFM	Atomic force microscope
Ab	Antibody
SEM	Standard error of the mean
WLC	Worm-like-chain
PZT	Piezoelectric translator
EGF	Epidermal growth factor
TNF-α	Tumor necrosis factor-α
IL-1β	Interleukin-1β
TM	Transmembrane
CR	Consensus repeat
HEV	High endothelial venule
PBS	Phosphate buffered saline
TSA	Tris-saline azide
BSA	Bovine saline albumin
DPBS	Dulbecco's phosphate buffered saline

GOF	Gain-of-function
LOF	Loss-of-function
ADAMTS13	A Disintegrin And Metalloprotease with a ThromboSpondin type 1
TTP	Thrombotic thrombocytopenic purpura

SUMMARY

During human hemostatic and inflammatory responses, cell adhesion molecules play a major role in regulating the way that leukocytes and platelets adhere to vascular surfaces in the hydrodynamic environment of blood circulation. Flow requirements have been reported for these cell adhesion events in vivo. Shear threshold and catch bonds have a close relationship for adhesion events, but need to be further elucidated. The structural basis to explain the mechanism by which catch bonds work is mostly hypothetical and also needs further investigation.

By studying the structure-function relationship of vascular adhesion molecules, such as L-selectin, GPIb-VWF, and ADAMTS13, which are involved in regulation of leukocyte and platelet adhesion to the vascular wall, we quantify the effects of three specific point mutations on L-selectin on its interaction kinetics with 2-GSP-6 and 6-sulfo-sLe^x, we characterize the kinetics of GPIbα as it interacts with the VWF A1 domain, and we characterize the kinetics of ADAMTS13 as it interacts with the VWF A1A2A3 tri-domain and we characterize its cleavage effects on A1A2A3. The overall project goal is to study how mechanical force regulates the binding kinetics of these proteins. These novel results are crucial in that they provide kinetics information on the single molecule level unlike the traditional biochemical binding assays. The biophysical measurements that are obtained using the single molecule technique help us to better understand how individual molecules behave in this mechanically stressful environment. The structural mutants of these proteins, which have been found to alter binding kinetics, suggest a possible molecular mechanism for either cell adhesion behavior (such as flow-

enhanced adhesion), or certain diseases (such as VWD and TTP). Understanding the molecular mechanism is crucial for disease diagnosis and treatments.

Selectin-ligand interactions (bonds) mediate the way leukocytes roll on vascular surfaces. The molecular basis for differential ligand recognition by selectins is poorly understood. Atomic force microscopy is used to compare the kinetics of wild-type L-selectin with the kinetics of three mutants of L-selectin interacting with 2-GSP-6; these mutants are a synthetic glycosulfopeptide modeled after the binding site of PSGL-1, and 6-sulfo-sLe^x, and a synthetic glycan prototypical of PNAd. Rather than first prolong (catch) and then shorten (slip) bond lifetimes, increasing force monotonically shortened the lifetimes of L-selectin MutI (A108H+H110A) and MutIA (A108H) bonds with 2-GSP-6. MutIB (H110A) exhibited an augmented catch bond. L-selectin also formed catch-slip transitional bonds with 6-sulfo-sLe^x. In sharp contrast, MutI, MutIA and MutIB had no effect on the bond lifetimes. These results distinguish molecular mechanisms for L-selectin to bind to PSGL-1 and PNAd.

Although catch bonds have been observed for selectins interacting with their ligands, it is still not clear whether other cell adhesion molecules also exhibit catch bond behavior. The interaction between glycoprotein Ib (GPIb) and the von Willebrand Factor (VWF) mediates platelet translocation at the vascular vessel damage sites, which plays a critical role in initiating platelet adhesion and thrombus formation. Similar to L-selectin-mediated tethering and rolling of leukocytes, translocation of platelets on VWF requires a shear threshold, suggesting a possible catch bond at work there. We characterized the kinetics of GPIbα interacting with the VWF A1 domain, confirming that the catch bond existed. Two type 2B VWD A1 mutants eliminated the catch bond and gave longer low

force lifetimes. The prolonged lifetimes at low force resulted in more agglutination of platelets with A1 coated microspheres in flow. Three type 2M VWD A1 mutants showed shifted catch-slip transitional bonds that exhibited shorter lifetimes at low force but longer lifetimes at high force level. A2A3 domains affected the GPIbα-A1 catch bond quantitatively. Type III collagen's capturing of A1 or A1A2A3 also quantitatively shifted their bond lifetimes with GPIbα, indicating that A1 could have different conformational states.

During the process of hemostasis, the size of prothrombotic ULVWF affects the affinity of VWF to platelets bearing GPIbα on the membrane. Seven years ago, ADAMTS13 was identified and characterized as a multi-domain metalloprotease that can cleave at the Tyr1605-Met1606 bond of VWF, thus regulating the size of ULVWF. We studied how force regulated the binding and cleavage of ADAMTS13 on VWF. The full length ADAMTS13 molecule formed catch-slip transitional bonds with A1A2A3 while CUB domains (CUB1&2) only formed slip bonds, suggesting that shear force may play a role in facilitating the enzyme's binding to its substrate. By utilizing the analysis of two force drop events, we found the cleavage effects could only be observed after the catastrophic structural change of A1A2A3. The putative uncoupling of A1 from the A2 domain could only have 14nm contour length increment and would not favor cleavage before A2 unfolding. The putative unfolding of the A2 domain would have much longer contour length increment capacity, depending on how many β-sheets would be pulled out of the A2 domain. Unfolding the A2 domain exposed the ADAMTS13 cleavage site and favored the cleavage. Two protocols using different stretching molecules (GPIbα and CR1) and A1A2A3 immobilization methods (physical adsorption and anti-His capturing

A3) revealed that the cleavage effects diminished with increases in stretching force. Regardless of single bond kinetics, time-to-unfold exhibited catch bond behavior for both stretching protocols, suggesting that catch bonds could also be observed during the domain internal structural change.

This study elucidated mechanisms of the binding kinetics of L-selectin with different structural components from PSGL-1 and PNAd by structural variants. It also provided new insights into our current knowledge of the dynamic adhesion and regulation of GPIbα-VWF interaction *in vivo*. Using the single molecule method, the chemical catalytic reaction between enzyme and substrate has been targeted. The results help characterize this important enzyme-substrate interaction involved in hemostasis.

CHAPTER 1

OBJECTIVES

The following aims were proposed to investigate the structure-function relationship of vascular tethering molecules' binding kinetics, including L-selectin vs. PSGL-1/PNAd, GPIbα vs. VWF, ADAMTS13 vs. VWF, and ADAMTS13's cleavage effects on VWF.

Aim 1: Quantify the effects of three specific point mutations on L-selectin on the interaction kinetics with 2-GSP-6 and 6-sulfo-sLe^x

This task will compare the kinetics of three mutants (MutI, MutIA, and MutIB) of L-selectin interacting with 2-GSP-6, a synthetic glycosulfopeptide modeled after the binding site of P-selectin glycoprotein ligand 1 (PSGL-1), and 6-sulfo-sLe^x (sialyl Lewis x), a synthetic glycan prototypical of peripheral node addressin (PNAd), with the kinetics of wild-type (WT) L-selectin. MutI (A108H and H110A), MutIA (A108H), and MutIB (H110A) are predicted to affect the off-rate and the catch bond between L-selectin and PSGL-1 but not to affect PNAd. The force regulation of off-rate will be measured using atomic force microscopy (AFM). This aim is designed to answer the following question:

- How do the structural variations in L-selectin affect the catch bond observed in WT L-selectin dissociating from PSGL-1 and from PNAd?

Aim 2: Characterize the kinetics of GPIbα as it interacts with VWF A1 domain

Although catch bonds have been observed for selectins interacting with their ligands, it is still not clear whether other cell adhesion molecules also exhibit catch bond behavior. The interaction between glycoprotein Ib (GPIb) and von Willebrand Factor (VWF) mediates platelet translocation at vascular vessel damage sites, which plays a

critical role in initiating platelet adhesion and thrombus formation. Similar to L-selectin-mediated tethering and rolling of leukocytes, translocation of platelets on VWF requires a shear threshold, suggesting a possible catch bond at work there. Type 2B and type 2M von Willebrand Disease A1 mutants have different affinities with GPIb, indicating different binding kinetics. In the VWF molecule, A2A3 domains may also potentially affect A1's binding with GPIb, in the presence or absence of collagen immobilization. This aim will address the following questions:

- Do interactions of GPIb with VWF A1 domain exhibit catch bond behavior?
- How do the type 2B and type 2M VWD A1 mutants affect the binding kinetics of A1 interacting with GPIb?
- How does A2A3 domain and collagen immobilization affect the binding kinetics of A1 interacting with GPIb?

Aim 3: Characterize the kinetics of ADAMTS13 interacting with VWF A1A2A3 domain triplet and its cleavage effects on A1A2A3

ADAMTS13 has been identified as an important enzyme for binding and processing the VWF molecule in blood plasma. The cleavage of VWF plays a vital role in controlling the size and amount of prothrombotic ULVWF in the plasma. The mechanism of this enzyme-substrate interaction is not clearly understood yet. Shear stress enhances the cleavage of ADAMTS13, and it is hypothesized that shear stress favors the unfolding of the A2 domain and that it exposes the cleavage site for ADAMTS13. To test the role of force in regulating the enzyme cleavage, we will address the following questions in this aim:

- How does force regulate the binding kinetics of ADAMTS13 and its structural variant with A1A2A3?
- How does force induce the unfolding of A2 domain and regulate the cleavage of A1A2A3 by ADAMTS13?

CHAPTER 2

BACKGROUND

Cell Adhesion in the Vascular System

Cell adhesion is essential for the development and maintenance of multicellular organisms(1). Cell adhesion is crucial to all developmental processes, but has a central role in the functions of the immune system throughout life(2). During the inflammation cascade, leukocytes tether to and roll on the activated endothelial cells of the inflammation site due to the interaction between PSGL-1 on leukocytes and P-selectin on activated endothelial cells and platelets(3). These adhesion events serve as the first step for the inflammation site to recruit patrolling leukocytes in the blood. When lymphocytes are homing to the lymph nodes, they need first to adhere to the endothelial cells of HEV (High Endothelial Venue) by the interaction of L-selectin with PNAd (Peripheral Node Addressin). This initiates the rolling and subsequent firm adhesion and transmigration processes which involve integrin and receptors(1, 3-5).

As leukocyte adhesion is important for the inflammation response, platelet adhesion plays an important role in hemostasis. Patrolling platelets adhere to and roll on the subendothelium exposed after the endothelium lining is damaged by vascular injury(6, 7). Initial adhesion through GPIb (Glycoprotein Ib) expressed on platelets binding to immobilized VWF (von Willebrand Factor) slows down the platelets. GPIb-VWF binding also triggers signaling inside the platelets and initiates the following firm adhesion through integrin and receptors. Integrin-involved platelet-platelet adhesion helps bring more platelets to the injury site to form a thrombus(6).

Upon activation, endothelial cells express long strings of ULVWF (ultra-large von Willebrand factor) immobilized on their surface by P-selectin or collagen. The

adhesion of flowing platelets to the immobilized hyper-adhesive ULVWF applies stretching force and induces conformational change on the molecule, which could facilitate cleavage of ADAMTS13, making smaller pieces of VWF multimers(8). Endothelial cells and platelet-derived ADAMTS13 could be physiologically important in processing VWF molecules in the multiple binding events that are involved in thrombus formation during hemostasis(9, 10).

2D Binding Assays of Receptor-Ligand Interactions

Under physiological conditions, cell adhesion molecules interact in two rather than three dimensions. Among those techniques that can be employed to measure receptor-ligand interactions in two dimensions, AFM (atomic force microscopy) allows measurement of molecular interactions subjected to small forces in the pico-Newton range. AFM is an established method in the Zhu lab (11, 12). In AFM, a laser light is shot on a reflective surface (usually golden) of a cantilever tip; the reflected light is captured by a photodiode detector, which can monitor subtle shifts of the laser spot position and can transform such shifts to voltage changes and force by relating sensitivity (V/nm) and cantilever spring constant (pN/nm) (Figure 2.1).

In single molecule mechanics studies, actuated by the elongated piezo tube, a ligand-coupled cantilever tip is brought into contact with a receptor, usually coated on the Petri dish or incorporated into a lipid bilayer on a cover slip. A binding event can be detected when the cantilever is retracted away from the surface because a tensile force, applied to the molecular interaction, causes the cantilever to bend. Dissociation of the binding interaction causes the cantilever to spring back and return to the force-free condition. The lifetime of the bond under constant force provides information about the bond dissociation rate: the longer the mean bond lifetime, the lower the bond dissociation rate. The ascending phase for loading the bond with force (Figure 2.1 right panel)

provides information regarding molecular mechanical properties including the bond's spring constant. The measurement distributions from hundreds of such binding events on different force scales provide information about the force-dependent lifetimes (off-rates), rupture forces, and molecular elasticity of single receptor-ligand interactions.

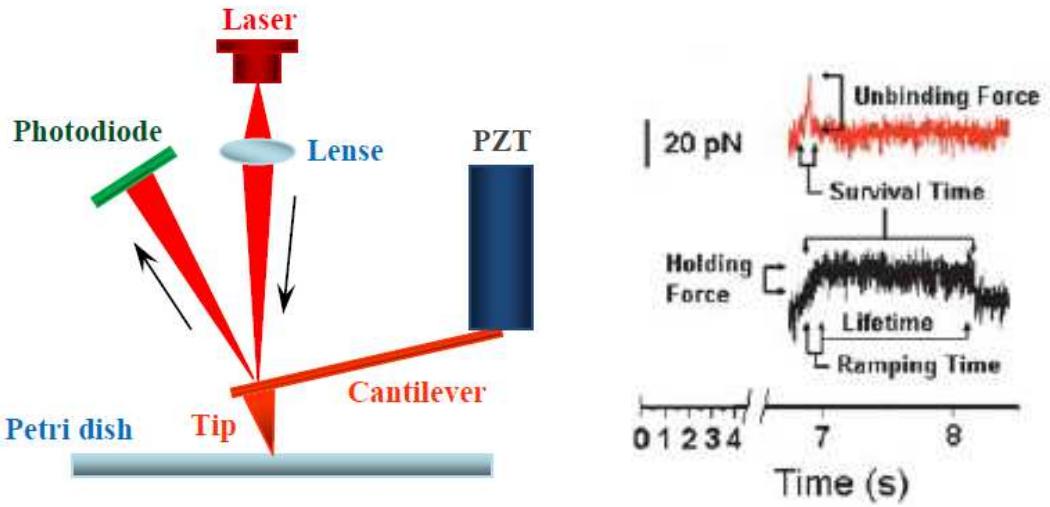

Figure 2.1: Schematic of AFM system (left) and force scan curves (right). Initially, the approach tracing was flat (zero mean force) but bent downward (negative force) when the tip was pressed onto the Petri dish. After touching the Petri dish surface, AFM cantilever was retracted to a distance above the surface and held there for 0.5 seconds to fish adhesion events. Then the PZT was retracted further to load the bond, if there was one, with predetermined force, i.e., 20pN. In this case, the retraction tracing was bent upward, indicating a tensile force that was applied to the tip through a molecular bond linked to the protein coated on Petri dish. In the rupture force experiment, the cantilever was continuously retracted until the bond broke and the tip sprang back to the unbent position (right red tracing). In the bond lifetime experiment, once it reached a predetermined adhesion force, the PZT would stop to hold the cantilever position and would apply a constant force to the bond until rupture (right black tracing). (11, 13)

Another important technique that complements AFM experiments uses the flow chamber. The flow chamber methods use a parallel-plate flow chamber in which purified molecules or cultured cell monolayers can be incorporated on the chamber floor(14, 15). Resembling the initial tethering and rolling of patrolling leukocytes/platelets in the vasculature, cells or microspheres with ligands expressed or coupled on the surface are

perfused through the chamber at various flow rates. Adhesion events can be visualized by video microscopy and can be further analyzed by software to get more details. Adhesion parameters that can be obtained include tether lifetimes (rates) and rolling velocities, etc.

Force Regulation of Bond Kinetics

Cell-surface ligands interact with selectins or GPIb to mediate tethering and rolling of flowing leukocytes or platelets on vascular surfaces; they act in response to infection or tissue injury(4, 7, 16). In this mechanically stressful environment, different forces are applied to receptor-ligand bonds at various rates. The relationship between off-rate and force partly determines how efficiently tethers produce rolling and how rapidly and stably cells roll(15).

Bell was the first to suggest that force could influence the dissociation of adhesive receptor-ligand bonds(17). Published work to date has revealed that the bond dissociation rate (off-rate) depends not only on the instantaneous force level(17-19), but also on the history of the force loading on the bonds(20). These observations have become the basis for different measurements determining off-rate regulation by forces applied on the bonds. One such measurement focuses on bond lifetimes recorded in a range of constant forces. Bond lifetime measurements have been made using flow chambers (14, 15, 21-27), atomic force microscopy (AFM)(11, 12, 28, 29), and biomembrane force probes (BFP)(30). Another type of measurement records bond rupture forces under a range of constant loading rates, and data can be further analyzed by dynamic force spectroscopy (DFS)(19, 31-33).

Catch Bonds and Shear Threshold

In 1988, Dembo was the first to hypothesize the existence of catch bonds, where increasing force prolonged bond lifetime (decreased bond off-rate)(18). It was not until

fifteen years later that this counter-intuitive mechamism for force regulated bond dissociation was first experimentally observed(11). Using AFM and transient tether lifetime measurements in the flow chamber, P- and L-selectin both showed catch bonds in lower force regimes when interacting with (s)PSGL-1(11, 12). At higher force ranges, the bond behaved as a slip bond. The specificity of catch bond behavior in P- and L-selectin/(s)PSGL-1 was confirmed by comparison with P-selectin/G1 and L-selectin/DREG56, antigen/antibody interactions showing only slip bonds, which can be well described by the Bell model. Catch-slip transitions were also observed for L-selectin interacting with endoglycan, a newly identified PSGL-1-like ligand(34, 35).

Under physiological conditions in the vascular system, selectins require a threshold shear to support cell adhesion(22, 36, 37). As shear drops below the threshold level, fewer flowing cells tether, the cells roll more rapidly and irregularly, and they begin to detach. Similarly, platelets also require arterial flow rates to adhere to the von Willebrand factor, immobilized on damaged vascular surfaces(7, 38). It is counterintuitive that the application of increased shear force on adhesion bonds actually stabilizes the tethering and rolling of the platelets. It has been hypothesized that flow increases the bonds' on-rates thus facilitating bond formation. That is, flow rate increases could improve the transport of adhesion molecules to their ligands so that more bonds will form before they dissociate(36, 39, 40). Another factor for shear-enhanced adhesion could be from increased cell surface contact area, which brings more adhesion molecules to the contact area(41, 42). An alternative hypothesis concerning the catch bond mechanism is that force prolongs bond lifetime and thus stabilizes rolling. Yago et al. measured the independent effects of transport, tether force, and contact area on transient tether and rolling of L-selectin-bearing microspheres or cells on PSGL-1 below and above the shear optimum(15). These results demonstrated that rolling below optimal shear was governed by catch bonds, whereas slip bonds govern rolling above optimal shear. By these carefully designed experiments, it was also found that tether force, not

shear rate, governed rolling velocity and rolling regularity below and above the flow optimum. Thereby, it was concluded that force-induced prolongation of L-selectin bond lifetime is essential for flow-enhanced cell adhesion.

However, Evans and colleagues used a biomembrane force probe showing that off-rates depend on precisely how the force is applied(33, 43). They found that the L-selectin-PSGL-1 bond is a slip bond, and with the molecules displaying two separate energy barriers to dissociation. From this point of view, the mechanism for catch bonds lies in how precisely the forces are applied to the molecules, with an overlap between different energy barriers leading to apparent catch bond behavior(33, 44). These works provide several possible different explanations of the shear threshold phenomenon, and the problem requires further investigation.

CHAPTER 3

MATERIALS AND METHODS

Proteins and Glycoconjugates

To study the force regulated binding kinetics of L-selectin with its ligands (PSGL-1 and PNAd derivatives), we used the following proteins and glycoconjugate constructs. L-selectin-Ig containing the lectin domain, EGF domain, and both consensus repeats of human L-selectin fused to the Fc moiety of human IgG that was described previously(12). The L-selectin-Ig chimera was purified from supernatants by protein G affinity chromatography and sent to us generously by Dr McEver's lab. The blocking antibody DREG56 for L-selectin (45) and PL1 for 2-GSP-6 (46) have been described previously. Goat anti-human IgG Fc polyclonal antibody was purchased from Chemicon (Temecula, CA). L-selectin lectin domain mutants were also sent to us by Dr McEver's lab. MutI has two point residue replacements at A108H and H110A; MutIA and MutIB have only a single point residue replacement, at A108H and H110A, respectively. As important ligands to bind L-selectin, biotinylated human P-selectin glycoprotein ligand-1 (PSGL-1) N-terminus peptide 2-GSP-6 and monomeric 6-sulfo-sialyl Lewis X (6-sulfo-sLe^x) as PNAd binding surrogate was described previously(47, 48). GPIbα molecules were expressed and purified from CHO (Chinese Hamster Ovary) cells by the labs of Dr Lopez and Dr Dong. Gain-of-function and loss-of-function VWF-A1 mutants as well as VWF A1A2A3 tridomain constructs were provided by Dr Cruz's lab. Type III collagen from human placentas was purchased from Sigma. Recombinant ADAMTS13 and CUB (CUB1 & CUB2) domains are provided by Dr Dong. Anti-6-Histidine antibody was purchased from Sigma. A1 domain monoclonal antibody CR1 was a generous gift from Dr Berndt. EDTA was purchased from Sigma.

Coupling of Proteins to Surface

WT/Mutant L-selectin-Ig was captured by 10μg/ml of goat-anti-human Fc IgG, 10μl of which was incubated on the Petri dish at 4 ^{o}C overnight. The labeled incubation spot was washed three times by TSA (Tris Saline Azide) buffer to remove excess IgG from the surface. Then 5μl of WT/Mutant L-selectin-Ig (5μg/ml) was added on the spot for one hour incubation under room temperature. Using DPBS (with Ca^{2+} and Mg^{2+}) containing 1% BSA (bovine serum albumin) without IgG, the incubation spot was washed once, then a Petri dish was filled with 8ml of this buffer.

Cantilever tips were incubated overnight at 4^{o}C in 10μg/ml Streptavidin (Pierce). After rinsing once by PBS, the coated cantilevers were incubated for 30 min at room temperature in DPBS (with Ca^{2+} and Mg^{2+}) containing 1% BSA (without IgG) to block nonspecific adhesion. Streptavidin-coated cantilevers were further functionalized by incubation in 10μl of 100ng/ml biotinylated 2-GSP-6 or 6-sulfo-sLe^{x} for 20 min at room temperature for specific adhesion experiments.

For studying the GPIb/VWF interaction, spots on the Petri dish were incubated by 10μl of 10ug/ml VWF-A1 (WT or mutant) or A1A2A3 tridomain overnight at 4^{o}C. Excess protein was removed after incubation by rinsing with PBS. PBS with 1% BSA buffer was added to the Petri dish to block non-specific binding. The AFM tip was incubated by 10μl of 10ug/ml glycocalicin, which is the extracellular domain of GPIbα. When using collagen capturing, 10μl of 15ug/ml type III collagen was incubated first on the Petri dish, then VWF-A1 or A1A2A3 (5μl 5ug/ml) was incubated secondarily to be captured by collagen.

When studying the ADAMTS13/A1A2A3 interaction, 10μl of 10ug/ml ADAMTS13 or CUB protein was incubated on the AFM tip; 10μl of 10ug/ml A1A2A3 was incubated on a Petri dish. A GPIb or CR1 coated tip was used to stretch the A1A2A3 tridomain. ADAMTS13 (5ug/ml) with/without EDTA (5mM) was added in the buffer during the cleavage experiments.

CHAPTER 4

BINDING KINETICS OF L-SELECTIN WITH STRUCTURAL VARIANTS OF PSGL-1

Introduction

The interactions of selectins with cell-surface ligands initiate rolling of leukocytes on activated endothelial cells or on activated platelets (Figure 4.1). The homing of lymphocytes into lymph nodes and the recruitment of leukocytes to sites of inflammation are multistep processes; selectins are essential in regulating the critical rolling phase of leukocyte adhesion (49). Named by the cell types they are expressed on, L-selectin is expressed on most leukocytes and binds ligands on endothelial cells and other leukocytes; P-selectin is expressed on activated platelets and endothelial cells, and it binds ligands on leukocytes and, in some cases, on endothelial cells; E-selectin is expressed on activated endothelial cells and binds ligands on leukocytes(3, 4).

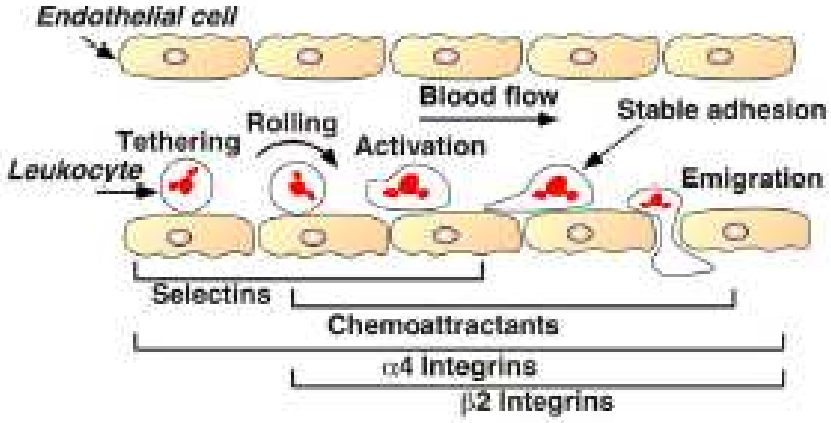

Figure 4.2: Interactions of selectins with cell-surface ligands initiate rolling of leukocytes to activated endothelial cells and thereby trigger the adhesion cascade. (Adapted from (4, 5))

Whereas L-selectin is constitutively and exclusively expressed on leukocyte membranes, the expression of P- and E-selectins is induced by inflammatory mediators such as thrombin or histamine(4). P-selectin is constitutively synthesized by megakaryocytes and endothelial cells, where it is sorted into the α-granules in platelets and Weibel-Palade bodies in endothelial cells. Upon cellular activation by mediators, P-selectin is redistributed to the cellular membrane. E-selectin is synthesized by activated endothelial cells induced by the inflammatory mediators such as TNF-α, IL-1β, or LPS and then transported to the cell surface(1, 3-5).

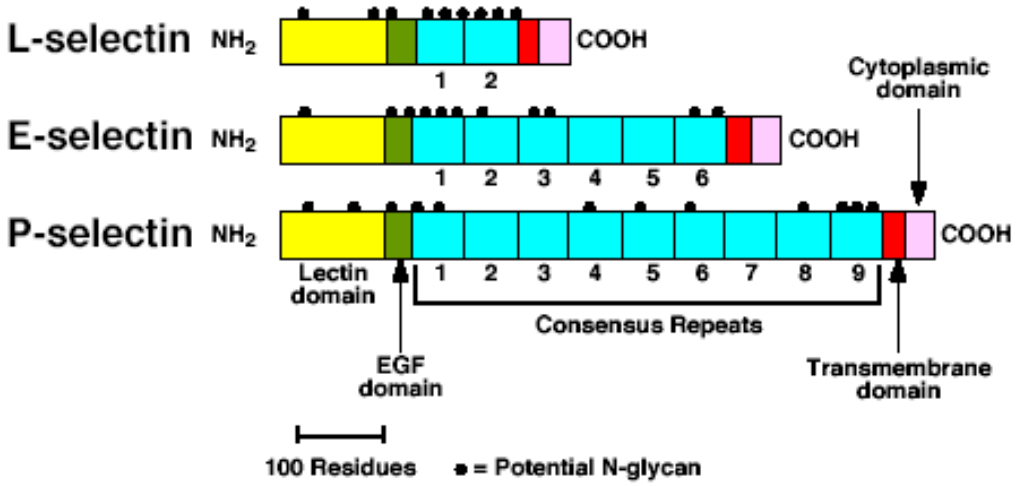

Figure 4.3: Domain organization of the selectins. Each selectin contains an N-terminal lectin domain, followed by an EGF-like motif, a series of consensus repeats similar to those in complement-regulatory proteins, a transmembrane domain and a cytoplasmic tail. Each molecule is extensively glycosylated with N-linked oligosaccharides (Adapted from (4)).

Regarding the molecular structure, each selectin has an N-terminal carbohydrate recognition lectin domain, followed by an EGF domain, a series of consensus repeats, a transmembrane domain, and a short cytoplasmic tail (Figure 4.2). P-selectin has 9 consensus repeats while E- and L-selectin have 6 and 2, respectively. The lectin and EGF domains of the three selectins share over 60% identity of the amino acid sequence(50, 51). The similarities maintain important secondary and tertiary structure features, but the

differences are also important, as they allow selectins to recognize subtle but critical distinctions in ligands, and thus to differentiate their biological functions.

It is important to determine which glycoconjugates mediate cell adhesion to selectins under physiological flow. All three selectins bind with low affinity to glycans with terminal components that include α2,3-linked sialic acid and α1,3-linked fucose, typified by the sialyl lewis x (sLe^x) determinant (Figure 4.3)(5). Sialyl lewis x (sLe^x) and P-selectin glycoprotein ligand-1 (PSGL-1) are important selectin ligands that bind to selectins with different affinities. PSGL-1 is the best characterized glycoprotein ligand for selectin, which has a transmembrane and homodimeric structure with multiple O-glycans on its serine and threonine residues (Figure 4.3)(3, 5). Antibody-blocking and gene-knockout studies in mice have shown that PSGL-1 is the key leukocyte ligand for P- and L-selectin(52, 53).

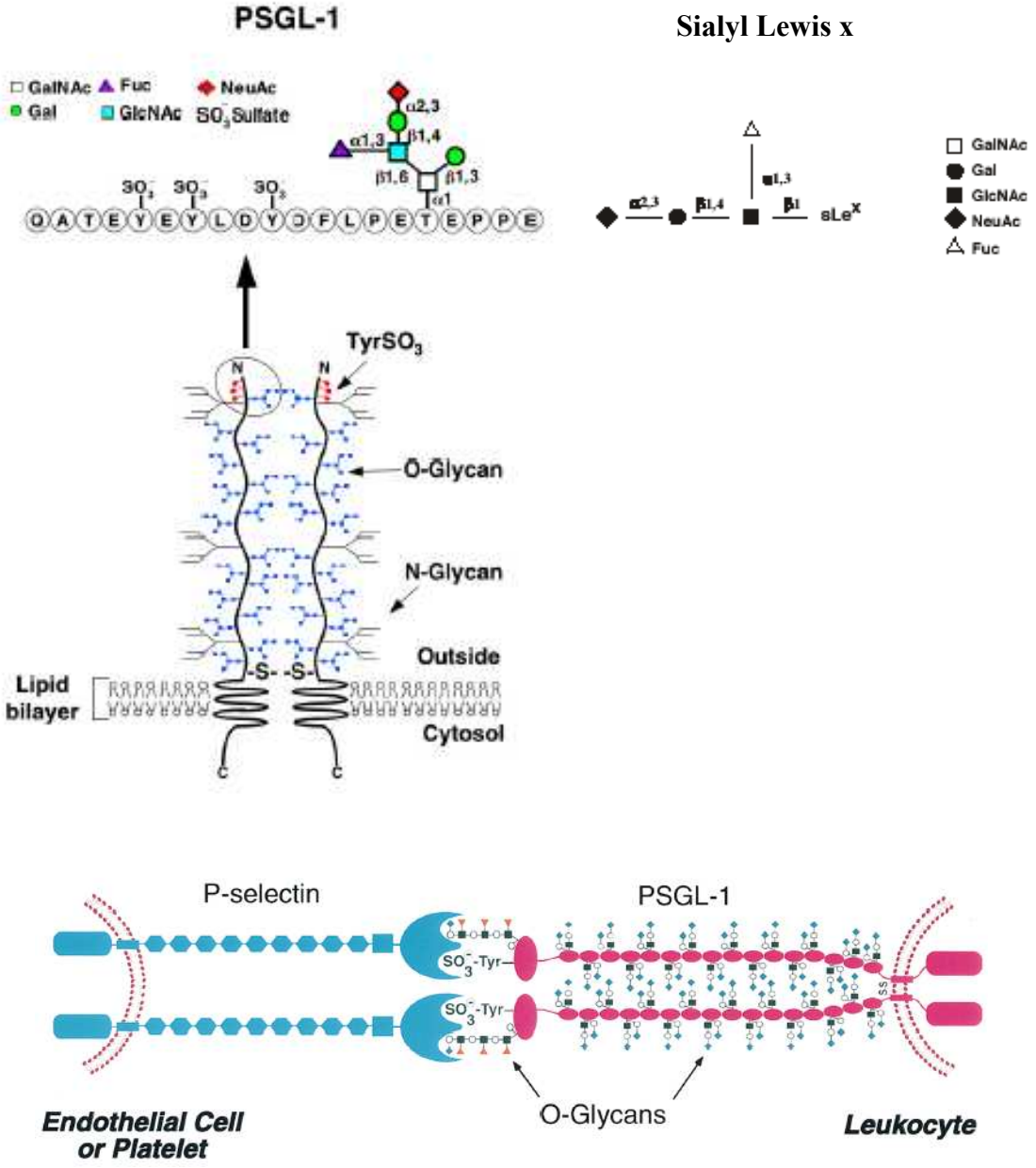

Figure 4.4: Structure of PSGL-1 and a tetrasaccharide Sialyl Lewis x (sLe^x). The lectin domain of P-selectin makes contact with the PSGL-1 N-terminal containing sLe^x, core-2 O-glycan and a nearby tyrosine sulfate residue. The symbols on the O-glycans of PSGL-1 represent sialic acid (NeuAc), galactose (Gal), N-acetylglucosamine (GlcNAc), and fucose (Fuc). (Adapted and modified from (3))

PSGL-1 is a dimmer having two identical subunits that associate non-covalently through the transmembrane domains, and form a disulfide bond just outside the membrane(54). Each subunit of PSGL-1 is decorated by many O-glycans linked to serine and threonine residues. In sharp contrast to most other mucins, PSGL-1 presents only a single N-terminal high-affinity binding site for both P- and L-selectin (Figure 4.3). The binding site consists of a short peptide sequence that is decorated with a specific core 2 O-glycan capped with sLe^x and with three sulfated tyrosine. Glycan, peptide, and sulfate components of PSGL-1 function cooperatively in a stereochemically precise array when binding with the lectin domain of P- or L-selectin(55-58). Although the binding site for P- and L-selectin is the same on PSGL-1, the binding kinetics and affinity differ significantly (5, 21, 22) (15, 57).

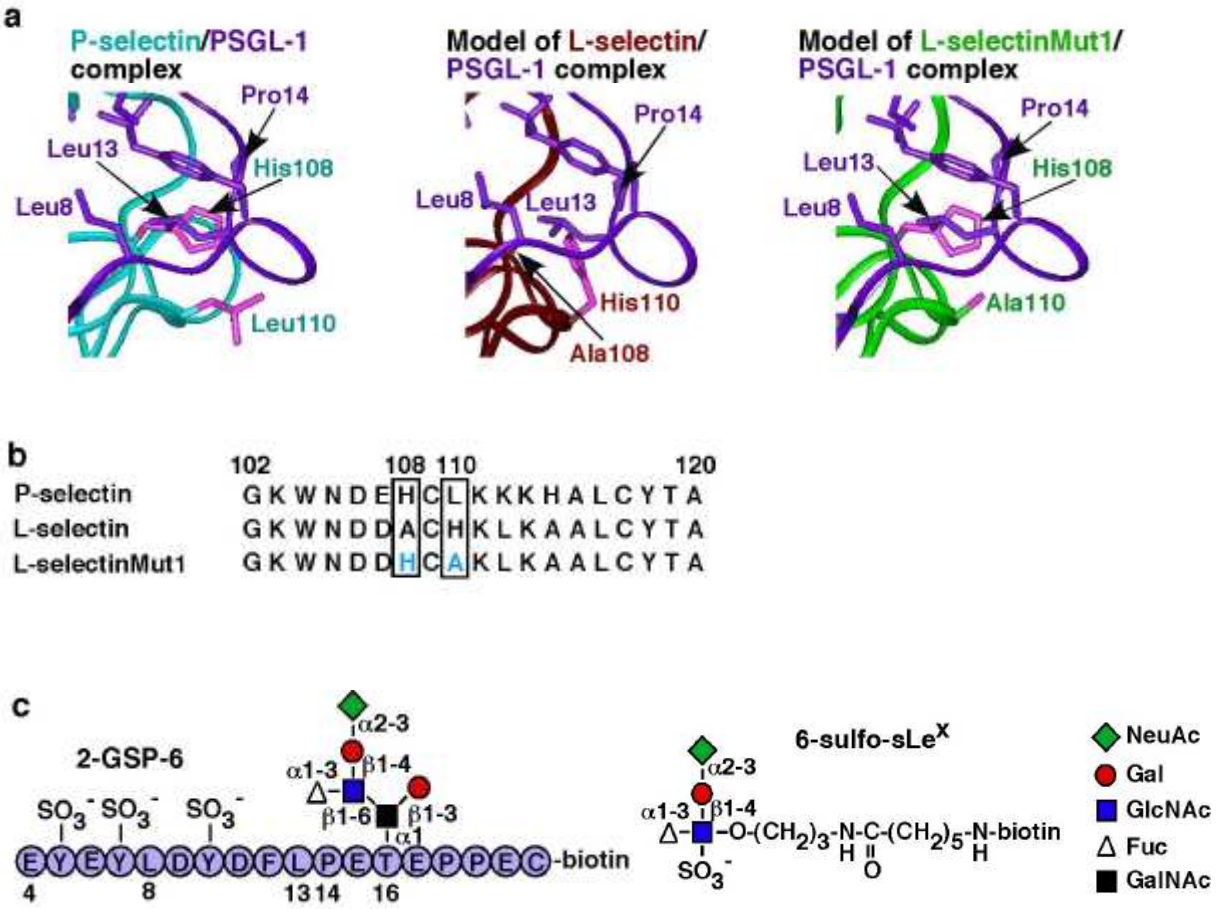

Figure 4.5: Model of L-selectin binding with PSGL-1. a, ***Left*, co-crystal structure of the P-selectin lectin domain in complex with an N-terminal glycosulfopeptide of PSGL-1. *Middle*, model of the L-selectin lectin domain in complex with PSGL-1. *Right*, model of the L-selectinMut1 lectin domain in complex with PSGL-1. Residue Leu8, Leu13, and Pro14 are in the glycosulfopeptide. Residues 108 and 110 are in the lectin domains.** b, **Alignment of the amino acid sequences of the lectin domains surrounding residues 108 and 110 (boxed), where substitutions were made to generate L-selectinMut1.** c, **Schematics of glycoconjugates used as selectin ligands. The glycosulfopeptide 2-GSP-6 was sequenced based on the N-terminal region of PSGL-1. A C-terminal cysteine was introduced to enable coupling of a single biotin by a spacer group (not shown). The 6-sulfo-sLe^x is a glycan determinant on O-glycans attached to PNAd. A spacer group links a biotin to the glycan as a molecular handle. (Adapted from (28))**

Besides PSGL-1, L-selectin also binds to several mucins from lymph node high endothelial venules (HEV), collectively called peripheral node addressin (PNAd). Sialylation, fucosylation and sulfation are necessary on PNAd molecular for its function to bind L-selectin optimally(59). These mucins are decorated with N- and O-glycans capped with 6-sulfo-sLe^x, a form of sLe^x with a sulfate ester attached to the C-6 position of GlcNAc(28). More detailed structural information is needed to thoroughly understand how sulfate, sialic acid, and fucose are optimally coordinated to interact with P- and L-selectin. Although there are >60% identical amino acid sequences of the lectin domains, the molecular basis for differential recognition of specific ligands by the selectins is largely unknown.

P- and L-selectin have been shown to form catch bonds with PSGL-1(11, 12). But the molecular mechanism for catch bonds is largely unknown. It is also unclear how the force-regulated binding kinetics are affected and modified by the structural components in the binding interfaces of selectins and ligands. Using the co-crystal structure of a human P-selectin-PSGL-1 complex as template, hints were possibly given for answering the above questions based on the model of N-terminal glycosulfopeptide from human PSGL-1 docking on the lectin domain of human L-selectin. One notable difference between P-selectin and L-selectin complexed with PSGL-1 is that there are more atomic level peptide interactions between P-selectin and PSGL-1 than L-selectin. Specifically, His108 of P-selectin stacks through hydrophobic contacts against Leu8, Leu13, and Pro14 of PSGL-1, while the corresponding Ala108 in L-selectin has a short side chain and is not predicted to make similar contacts with PSGL-1. Additionally, in L-selectin, steric interference from a bulky His110 side chain might also prevent stacking. Thereby, the model predicts that a mutant L-selectin that replaces Ala108 with His, for more atomic level interaction, and His110 with Ala (A108H/H110A, or MutI), for less steric

hindrance, would interact better with the peptide region of PSGL-1. This L-selectin MutI potentially would make L-selectin more like P-selectin in binding with PSGL-1.

L-selectin binds to the 6-sulfo-sLe^x determinant on PNAd but is not known to bind directly to the peptide backbones of these heterogeneous glycoproteins. Therefore, the model predicts that the amino acid substitutions in L-selectin MutI would alter binding to PSGL-1 but not to PNAd. To test the model and hypothesis, we used 2-GSP-6, a glycosulfopeptide modeled after the N-terminal region of PSGL-1, and 6-sulfo-sLe^x that recapitulates PNAd as ligands for P- and L-selectin. It is also predicted that 2-GSP-6 will form catch bonds with WT L-selectin and that the L-selectin MutI would affect the catch bond. Similarly, the prediction is that L-selectin MutI would not affect the catch bond when binding with 6-sulfo-sLe^x. Two single point mutants of L-selectin, A108H (MutIA) and H110A (MutIB) were both tested to further characterize and complement the mutant effects of MutI binding with PSGL-1 and PNAd.

Results

Binding Specificity Control by Proper Distance

In our experiment protocol, physical adsorption was used to coat the AFM tip and the Petri dish surface with proteins. Wild-type (WT) or mutant L-selectin (MutI, MutIA or MutIB) Ig chimera was captured by goat-anti-human Fc IgG (Figure 4.5). The capturing antibody was incubated on the Petri dish at 4 ^{o}C overnight, with the concentration of 10µg/ml in PBS. Parafilm was used to seal the Petri dish to keep the protein from drying out. On the day of the experiment, the Petri dish was washed three times by TSA to remove unadsorbed protein from the surface. Then 5µl of WT/Mutant L-selectin-Ig (10µg/ml) purified protein was added on the labeled spot for one-hour secondary incubation at room temperature. Damp tissue was covered on the Petri dish during incubation to preserve moisture. Using DPBS (with Ca^{2+} and Mg^{2+}) containing 1% bovine serum albumin (BSA without essential IgG), the incubation spots were washed once, then the Petri dish was filled with 5ml of this buffer.

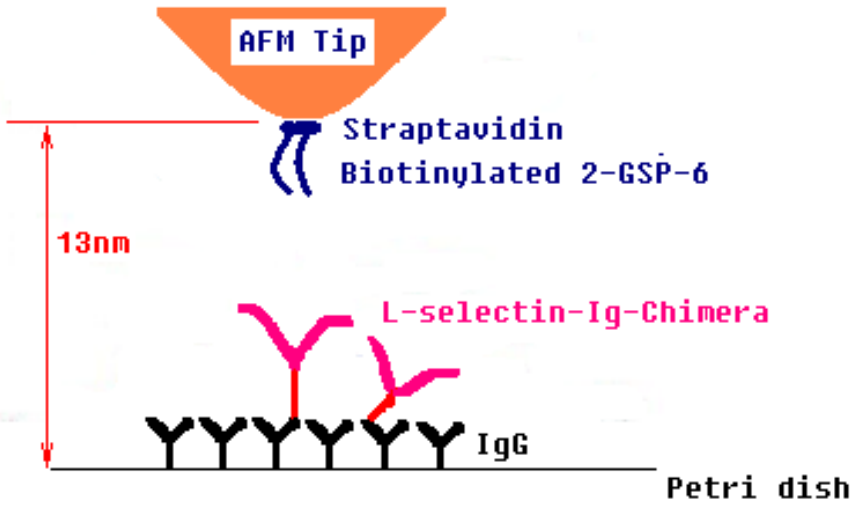

Figure 4.6: Experimental set-up of AFM assay to study L-selectin/mutants interaction with 2-GSP-6 or 6-sulfo-sLe^{x}

Cantilever tips were incubated overnight at 4°C in 10μg/ml streptavidin (Pierce) in PBS. After rinsing by PBS, the streptavidin coated cantilevers were blocked for non-specific adhesion by 1% BSA in PBS at room temperature for 30 min. The AFM tips were used either to test non-specific binding frequency, or for secondary functionalization by incubation in 8μl of 500ng/ml biotinylated 2-GSP-6 or 6-sulfo-sLe^x for 20 min at room temperature for specific adhesion experiments.

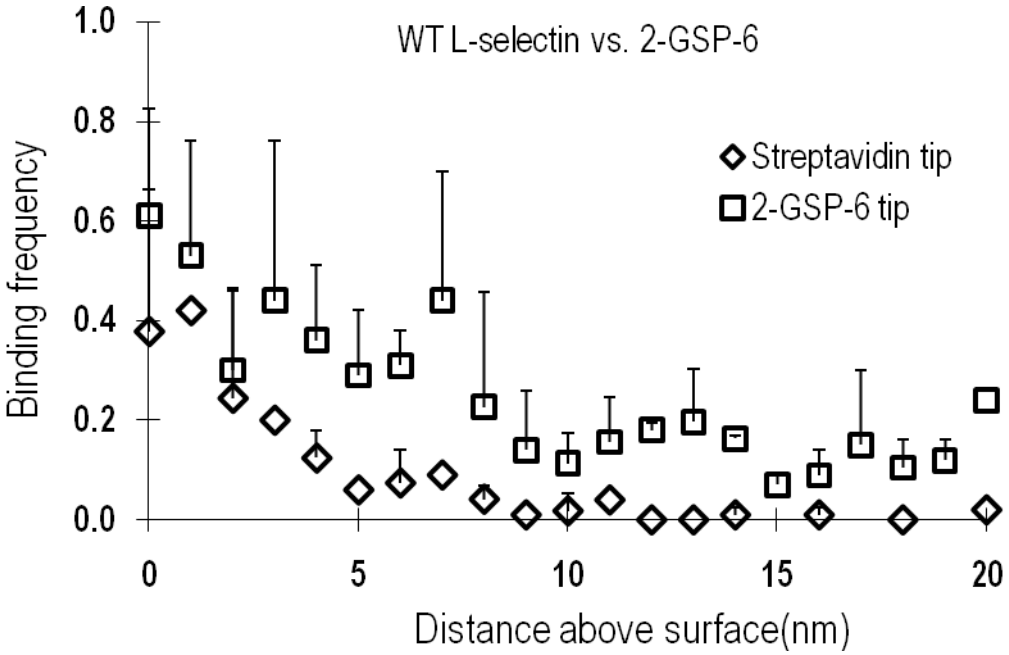

Figure 4.7: Binding frequency dependence on the distances between AFM tip and Petri dish surface. Proper distance was used to suppress non-specific binding frequency <5% (diamond) while getting ~20% specific binding frequency (square).

We started our experiments by first quantifying the proper distance to suppress the non-specific binding while still maintaining high enough specific binding. The dependence of the binding frequencies on the distances from the Petri dish surface has been characterized for both non-specific binding, wherein a streptavidin coated tip (blocked by BSA) interacts with WT/Mutant L-selectin-Ig, and for specific binding, wherein a 2-GSP-6/6-sulfo-sLe^x coated tip interacts with WT/Mutant L-selectin (Figure 4.6). The results revealed that the non-specific binding frequencies decreased rapidly below 5% when the distance increased to 10 nm. In contrast, the specific binding

frequency showed a flatter curve and could still maintain ~15% binding frequency when the distance was larger than 10 nm. These results manifest the effectiveness of controlling the interaction specificity through distance. Nonspecific interaction is essentially electrostatic interaction between two surfaces.

From these results, we set 13nm as a predetermined distance above the Petri dish surface, at which distance the non-specific binding frequency was low enough, but the specific binding frequency was much higher, ~20%, such that we could continue for single bond lifetime measurements. At the beginning of each experiment, the non-specific binding frequency would first be tested at 13 nm distance from the surface by using the BSA tip to assess the quality of sample preparation, that is, the protein coating on the Petri dish. Once we confirmed that non-specific binding was less than 5%, a tip functionalized with L-selectin ligands would be loaded for the specific binding test. If the specific binding frequency was high enough for lifetime capturing, usually between 15-30%, the force clamp program would be started to harvest lifetimes. Sometimes 13nm would not be enough to suppress non-specific binding below 5%. Then the distance would be increased by 1nm increments for the assessment again until satisfied. If the distance was too great, such that there was no detectable level of specific binding, we would change the protein coated spots or change the sample.

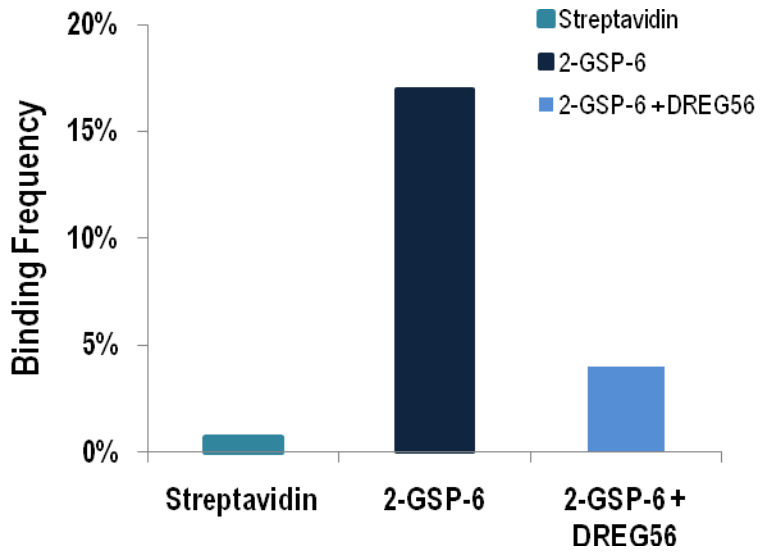

Figure 4.8: Specificity test of 2-GSP-6 coated AFM tip binding with wild-type L-selectin.

Binding specificity was also verified through EDTA wash, DREG56 and PL1 blocking experiments. Figure 4.7 shows the effect of DREG56 blocking. DREG56 is a monoclonal antibody that can block L-selectin's binding site for 2-GSP-6(12). Compared with a streptavidin coated tip, loading a 2-GSP-6 coated tip increased binding frequency, evidently because of specific interaction. To confirm that this increase came from the 2-GSP-6/L-selectin interaction, we added mAb DREG56 (10ug/ml) to the working buffer and gently shook for 10 minutes, bringing down the binding frequency to the non-specific level, which indicated that L-selectin lost its ability to bind 2-GSP-6. EDTA chelates the Ca^{2+} required for L-selectin binding with 2-GSP-6 and 6-sulfo-sLe^x. Binding frequency decreased immediately after addition of 5mM EDTA in the buffer (DPBS with 1% BSA). Binding frequency recovered after providing Ca^{2+} again through adding DPBS (with Ca^{2+} and Mg^{2+}) buffer in the system (data not shown). PL1 is a monoclonal antibody targeted for 2-GSP-6 and inhibits its binding with L-selectin. The observation was similar to DREG56 and EDTA's effect, and thereby confirmed the binding specificity (data not shown).

As force increases wild-type L-selectin forms catch bonds and then slip bonds with 2-GSP-6 and 6-sulfo-sLe^x, but MutI and MutIA L-selectin form only slip bonds with 2-GSP-6

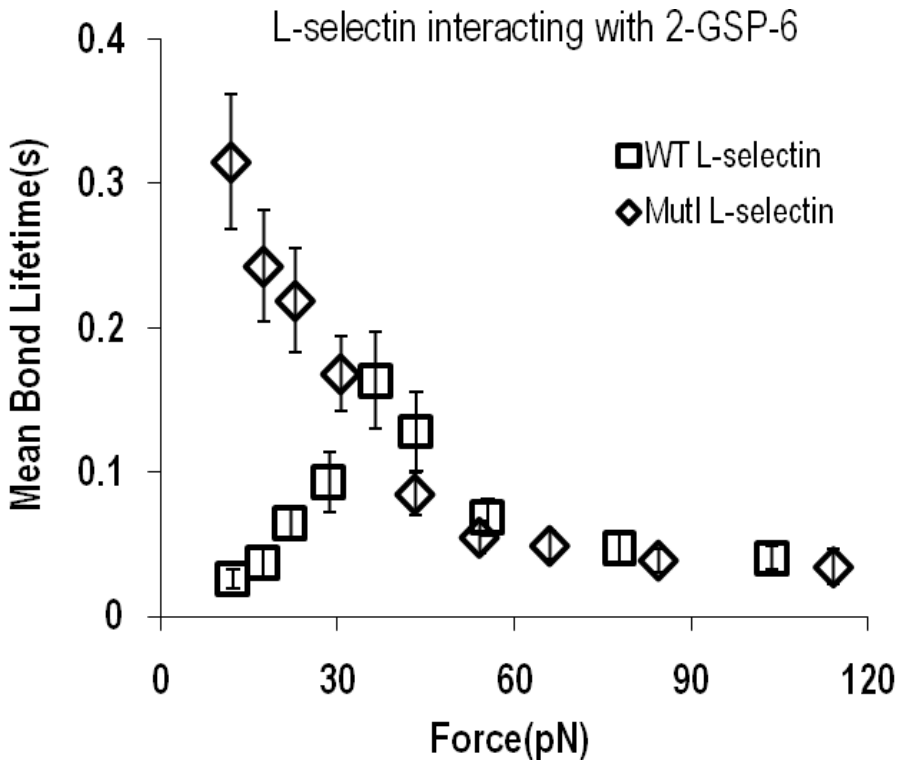

Figure 4.9: Mean bond lifetime measurement vs. force for WT/MutI L-selectin interacting with 2-GSP-6. MutI L-selectin eliminates the catch bonds at low forces regime.

Figure 4.8 shows the lifetime comparison of WT/MutI L-selectin binding with 2-GSP-6, confirming that WT L-selectin forms catch bonds with 2-GSP-6, while binding with PSGL-1. The lifetime peaks at ~37pN and gives ~0.17 seconds lifetime. This peak lifetime value is comparable to that of the L-selectin-PSGL-1 bond but with lower peak force(12). After the peak, the bonds' lifetimes decrease with increasing force, exhibiting slip bond behavior. In sharp contrast, MutI L-selectin totally eliminates the catch bond regime, giving monotonously decreasing lifetimes with increasing forces. The slip bond

regime collapses with that of WT L-selectin. The elimination of catch bonds by MutI generates maximum difference of bond lifetimes at near-zero force level.

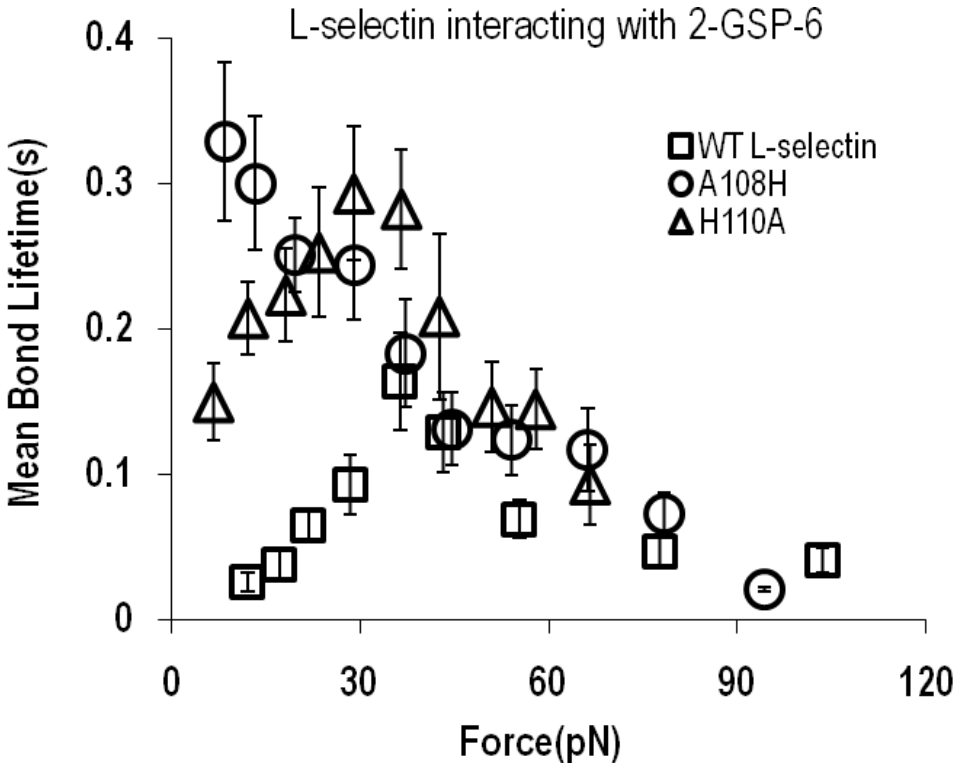

Figure 4.10: Mean bond lifetime measurement vs. force for MutIA/MutIB L-selectin interacting with 2-GSP-6, compared with WT L-selectin data from Figure 4.8 (square). MutIA (A108H) L-selectin (circle) eliminates catch bonds at low forces regime as MutI; MutIB (H110A) L-selectin (triangle) quantitatively shifts the catch-slip bond as MutII (N138G). (30)

After studying MutI, we continued to test the two point mutants: MutIA (A108H) and MutIB (H110A) to further characterize the mutant effects (Figure 4.9). Interestingly, MutIA exhibits behavior similar to MutI in that it also eliminates the catch bond regime at low force, with monotonously decreasing lifetimes with increasing forces. MutIB showed enhanced catch bonds at low force, giving longer lifetimes at the catch bonds regime than the WT L-selectin. Lifetimes peak at ~0.3 seconds and shift toward lower force (~30pN). When forces are larger than 30pN, the bonds transit to slip bonds with decreasing lifetimes until approximating the slip bond curve of WT L-selectin.

WT L-selectin forms catch-slip bonds with 6-sulfo-sLe^x, L-selectin mutants MutI, MutIA and MutIB have no effects on bond lifetimes with 6-sulfo-sLe^x

After characterizing WT L-selectin and mutant effects on their binding kinetics with PSGL-1 surrogate 2-GSP-6, we further tested whether amino acid residue replacements on the peptide backbone affect L-selectin's binding with PNAd surrogate 6-sulfo-sLe^x. Figure 4.10 illustrates the lifetime measurements of WT L-selectin interacting with 6-sulfo-sLe^x, in comparison with two mutants A108H and H110A.

In marked contrast to the lifetime data of L-selectin interacting with 2-GSP-6 (Figure 4.9), interactions between L-selectin and 6-sulfo-sLe^x also exhibit catch-slip transitional bonds as force increases. Neither MutIA nor MutIB changed the WT L-selectin's catch-slip transitional bonds with 6-sulfo-sLe^x, confirming our hypothesis that the amino acid residue substitutions in L-selectin alter the force dependent kinetics of L-selectin bonds in a ligand-specific manner as predicted by the structure model. That is, the A108H and H110A mutations are located at the 2-GSP-6 binding interface but not in direct atomic level interactions with 6-sulfo-sLe^x; therefore these two point mutations affected L-selectin binding with the PSGL-1 surrogate but not with the PNAd surrogate.

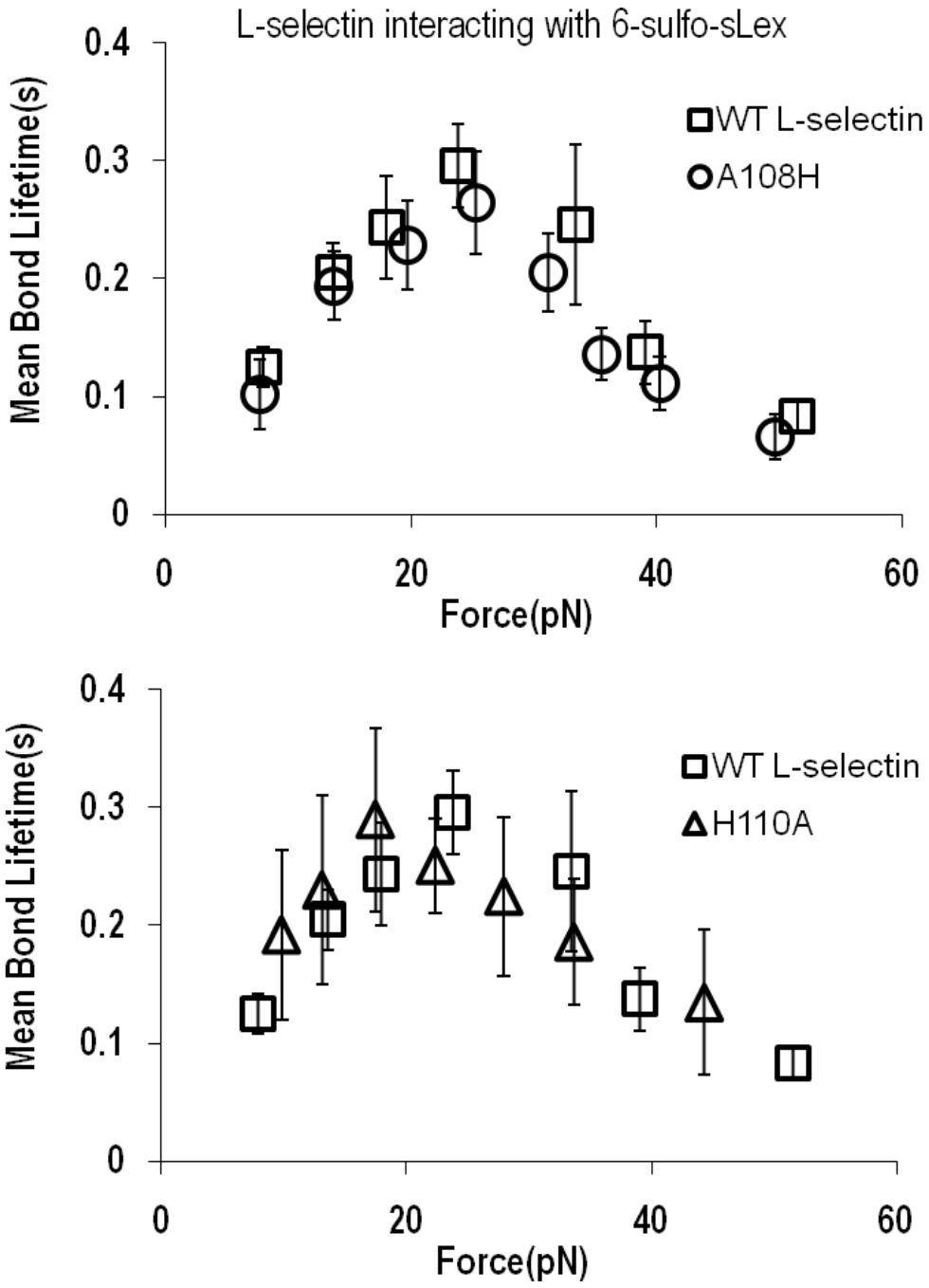

Figure 4.11: Mean bond lifetime vs. force measurements for MutIA/MutIB L-selectin interacting with 6-sulfo-sLe^x, compared with WT L-selectin data (square). MutIA (A108H, circle) and MutIB (H110A, triangle) mutants haven't changed the catch-slip bonds of WT L-selectin/6-sulfo-sLe^x.

Discussion

The mean bond lifetime measurements obtained by using AFM are in good agreement with the flow chamber experimental data (Figure 4.11). In the flow chamber experiments, microspheres were coated with selectin-Ig chimeras captured by anti-human Fc antibody and perfused at various shear rates (thus different wall shear stresses) over low densities of 2-GSP-6 or 6-sulfo-sLe^x captured by streptavidin on the flow chamber floor. Transient tether lifetimes were measured by high-speed video microscopy(28).

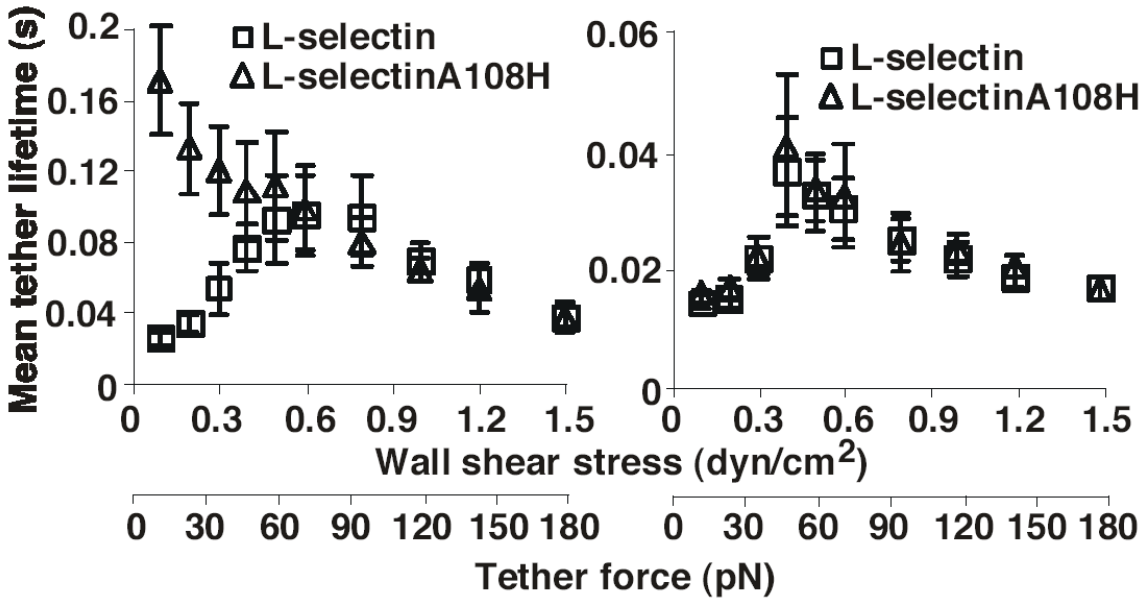

Figure 4.12: WT and MutIA L-selectin tether lifetime measurements by flow chamber experiments, showing single-residue substitution in L-selectinA108H converts catch bonds to slip bonds with 2-GSP-6 (left panel) but not with 6-sulfo-sLe^x (right panel). (Adapted from (28))

Previous studies have demonstrated that the rolling of L-selectin-bearing microspheres or cells on PSGL-1 below optimal shear was governed by catch bonds, whereas rolling above optimal shear was governed by slip bonds(15). To determine whether eliminating catch bonds affects the shear threshold requirement for L-selectin-dependent rolling, microspheres bearing L-selectin were perfused over higher densities of 2-GSP-6 or 6-sulfo-sLe^x. Rolling motions were recorded and analyzed based on high-

speed video microscopy as a function of wall shear stress. The results show that the amino acid substitutions of L-selectin as in MutI and MutIA eliminate the shear threshold for rolling on 2-GSP-6 but not on 6-sulfo-sLe^x, and further document that catch bonds govern flow-enhanced neutrophil adhesion through L-selectin(28).

It has not been explained why circulating leukocytes do not aggregate with each other even though they express both L-selectin and its ligand PSGL-1. One possible explanation is that the bonds formed between randomly colliding leukocytes through L-selectin/PSGL-1 interaction have lifetimes at small forces (the relative velocity between circulating leukocytes is low) that are too short for stable adhesion because of catch bond formation. To test this hypothesis, neutrophils or mixtures of neutrophils and microspheres bearing L-selectin were flown in a shear field to promote collisions at a wall shear stress of 1 dyn/cm^2. To quantify the aggregation effects, mixtures of neutrophils (labeled with red dye PKH26) and microspheres (labeled with green dye FITC) were perfused and fixed after they exited the flow chamber. Flow cytometry and fluorescence microscopy revealed very few particles containing fluorescence markers for both neutrophils and L-selectin microspheres. However, it showed many particles labeled for both neutrophils and L-selectin MutI/MutIA microspheres, confirming that aggregates developed through engagement of L-selectin MutI/MutIA (Yago *et al.*, unpublished data). These data suggest that these two mutants prolong lifetimes by eliminating catch bonds between PSGL-1 and L-selectin and that they cause aggregation of flowing leukocytes. The catch bond mechanism shortens lifetimes under small forces that link cell aggregates but lengthens lifetimes under large forces that act on those bonds that support cell rolling. Therefore, this mechanism would allow leukocyte rolling on vascular surfaces but not aggregation of circulating leukocytes.

The prolonged lifetimes of MutI/MutIA L-selectin with 2-GSP-6 at very low forces suggest that the “better stacking” mutant A108H provides additional atomic level interactions to peptide components of PSGL-1 such that the binding is stronger than WT

L-selectin at lower forces. The molecular mechanism of the catch bonds between WT L-selectin and PSGL-1 still requires further study. One possible explanation for the elimination of the catch bond is that the replacement of Ala by His at 108 changes the possible path during dissociation along the binding interface.

The similarities between MutI and MutIA interacting with 2-GSP-6 and 6-sulfo-sLe^x indicate that A108H substitution causes the elimination of catch bonds; this was also confirmed by H110A data showing a catch bond that was shifted instead of being eliminated. MutIB exhibits augmented catch bonds with longer lifetimes at smaller forces, which is similar to the L-selectin MutII N138G(30). Unlike the allosteric mutation at the hinge linking the L-selectin EGF domain and the lectin domain, H110A is located at the direct binding interface of the receptor-ligand. Therefore, it is more likely that the decreased steric hindrance would allow more new interactions during forced dissociation along the binding interface. Again, because this change will most likely affect the peptide interaction, the binding kinetics with 6-sulfo-sLe^x are not affected, as is confirmed by the lifetime data.

It is interesting to find WT, MutIA and MutIB L-selectin form similar catch bonds with 6-sulfo-sLe^x. There must be another mechanism by which force enhances interacts with this ligand, which has no peptide components. The interaction of L-selectin and its mutants binding with 6-sulfo-sLe^x includes hydrogen bonds and ionic bonds involved in the calcium coordination. Each individual bond could be derived as following the Bell model(17). In this regard, the sliding-rebinding model could also be applied, thus generating the catch bonds(60).

The residue substitutions A108H and H110A of L-selectin were designed to make it more like P-selectin when interacting with PSGL-1. Although much longer lifetimes were obtained from elimination of catch bonds at low forces, MutI and MutIA exhibit no detectable catch bonds with PSGL-1, while P-selectin displays catch-slip transitional bonds with PSGL-1 and has even longer bond lifetimes at all forces. These data suggest

that other differences between P- and L-selectin also contribute to the off-rate differences. These factors could be allosteric regulation, as discussed previously(30). These results offer insights into the structural basis for the catch bonds, and they show how force affects interaction kinetics among adhesion molecules.

CHAPTER 5

BINDING KINETICS OF GPIBA WITH VWF

Introduction

The primary function of hemostasis is to stop bleeding at sites of injury. Platelets' adhesive functions are necessary to limit blood loss at sites of vascular injury, including areas of the circulatory system with the highest levels of shear stress(7). Moreover, platelets are of vital importance in the process of acute occlusion of atherosclerotic arteries, ischemia-reperfusion injury, deep venous thrombosis, and inherited bleeding disorders(61-66). The formation of a platelet plug to staunch blood leaking from an injured vessel is a multistep process that involves many molecular interactions (Figure 5.1).

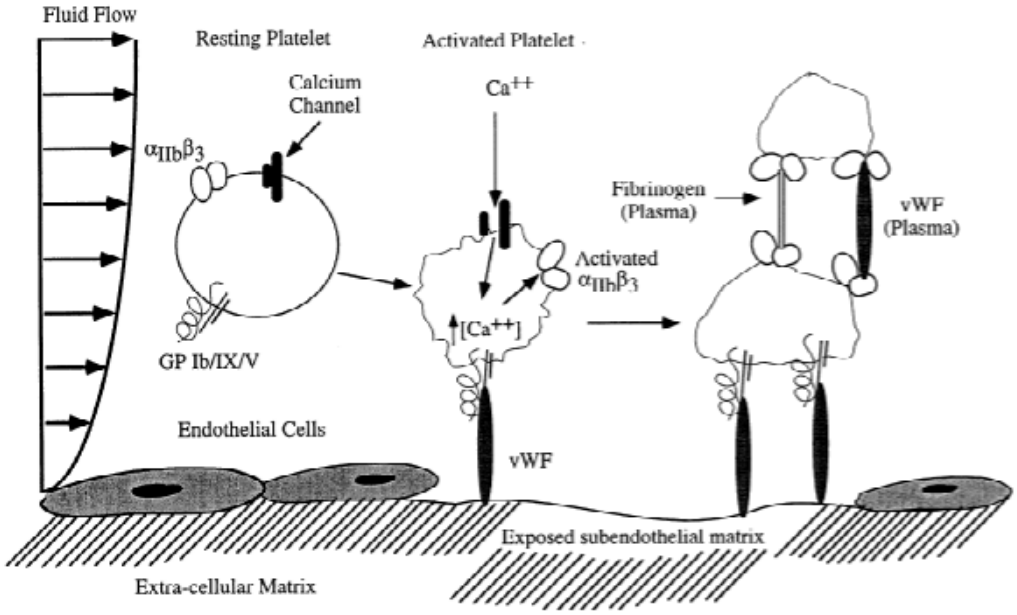

Figure 5.13: Schematics showing the multiple steps of hemostasis. (Adapted from (6))

The binding of platelet glycoprotein (GP) Ib-IX-V to its ligand immobilized on the exposed subendothelium surface, the von Willebrand factor (VWF), initiates the first step of hemostasis by recruiting patrolling platelets in the blood to the damaged vascular surface and also initiates the thrombi formation that underlies cardiovascular heart diseases and stroke (7). Glycoprotein Ibα (GPIbα) is the central component of the receptor complex expressed on the platelets' surface; it contains eight tandem leucine-rich repeats (LRRs) that wrap around one side of the von Willebrand Factor (VWF) A1 domain (67, 68) (Figure 5.2).

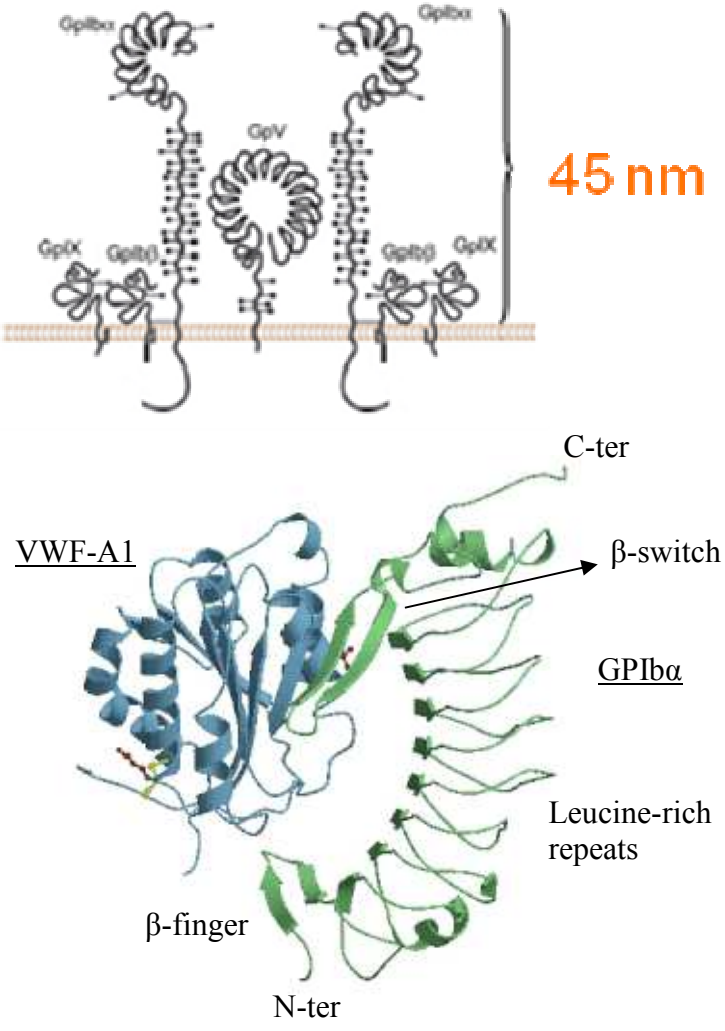

Figure 5.14: Schematics of GPIb-IX-V complex structure (adapted from (69)), and co-crystal structure of GPIbα-A1 complex. (Adapted from (68))

VWF, synthesized in megakaryocytes and endothelial cells as pre-pro-VWF, undergoes an extensive posttranslational process of cleavage, glycosylation, sulfation, multimerization and sorting in the endoplasmic reticulum, the Golgi apparatus and the trans Golgi network (70, 71). VWF is partitioned through two pathways, ~95% constitutively secreted and the rest stored in the tubular structures in the α-granules of megakaryocytes and in the Weibel-Palade bodies of endothelial cells, which release it upon activation (72, 73). After being released into the plasma, adhesive ultralarge VWF (ULVWF) multimers are cleaved by metalloprotease ADAMTS-13 at A2 domain into smaller circulating pieces which are less adhesive under normal shear (74, 75).

For binding with GP Ibα, VWF-A1 needs to be activated through high fluid shear, modulators (such as snake venom ristocetin or botrocetin), or through immobilization to extracellular matrix proteins (such as collagen) (76). Type 2B VWD mutations can also activate VWF-A1, possibly through changing the molecular conformation (76). There are three types of VWD resulting from qualitative or quantitative deficiency in VWF: type 1, 2 and 3 VWD. Type I refers to a partial quantitative deficiency of VWF; Type II is related to a qualitative VWF deficiency; while type III refers to total deficiency of VWF. Type II VWD can be further divided into four subtypes: Type 2A is characterized by the absence of a normal amount of ULVWF that leads to decreased platelet-dependent function; Type 2B VWD has been characterized in terms of a gain-of-function phenotype with increased affinity for GPIbα and removal of ULVWF from the circulation (77); Type 2M VWD patients have normal ULVWF counts but have decreased GPIbα binding affinity, thus these are so-called loss-of-function mutations; Type 2N refers to VWF with decreased affinity for factor VIII.

At least fourteen mutations, located mostly inside a disulfide loop C509-C695 of VWF-A1, have been found associated with type 2B VWD (78-80). From the secondary structure, these mutations are scattered throughout the A1 domain and its N- and C-terminal flanking peptides. While in the 3D crystal structure, these mutations cluster at

the bottom of the domain (Figure 5.2). Furthermore, type 2B mutations have been reported to induce the A1 conformational change at the GPIbα binding interface (81). The molecular mechanism for gain-of-function is not clear yet. In contrast, type 2M mutations scatter all over the 3D crystal structure of the A1 domain, with some mutations buried inside the Rasman fold but still essential for the A1 conformation. It is hypothesized that these mutants would result in a mis-folded structure for the A1 domain, thus affecting binding with GPIbα.

What makes the hemostatic and thrombotic processes remarkable is that platelets adhere and aggregate under dynamic conditions of blood flow, which transports platelets, and against hydrodynamic forces, which push platelets away. As key regulators, flow and force impact these processes in multiple ways (82). Circulating plasma VWF does not agglutinate flowing platelets under physiological conditions, but it does so when exposed to pathologically high shear flow (such as found in areas of stenosed arteries) in a process called shear-induced platelet aggregation (76). Platelets tether to, and roll on, immobilized VWF, but do not firmly adhere under arterial flow (83). Flow enhances rather than impedes platelet adhesion, despite the dislodging forces (7). Platelets usually do not tether at low flow, and rolling platelets detach if arterial flow is reduced (38, 84). Although counter-intuitive, these VWF-mediated adhesion properties may be biologically important. Disease-related mutations in VWF have been found to change the mechanical regulation of platelet adhesion. For example, a single-residue type 2B mutant I1309V in the VWF A1 domain (85) lowers the shear requirement for binding (38, 84).

The similarities between selectins and GP Ibα-VWF in promoting and sustaining cell adhesion in flow suggest that their receptor-ligand bond kinetic properties may also be similar. Kinetic studies have demonstrated a high rate of bond formation and dissociation between GPIbα and VWF-A1 (38, 68, 84, 86). The slow intrinsic binding kinetics of the GPIbα-VWF-A1 bond have also been reported to mediate rapid platelet adhesion (87). Using AFM and transient tether lifetime measurements in the flow

chamber, the catch bond has been revealed to govern the flow enhancement of L-selectin mediated leukocytes adhesion (15). Here we demonstrated that flow-dependent platelet adhesion is subject to catch-slip-transitional bonds, and that the mechanism of "gain-of-function" is due to slow off rate at low force. From the single molecular kinetics measurement, our studies are important to understand platelet function and related disease.

Results

Binding Specificity Control by Proper Distance

To test our hypothesis that a catch bond exists for the GPIbα-A1 interaction, we started by measuring the bond lifetime. To measure a specific interaction, the non-specific binding frequency needs to be controlled at a low enough level. Because we control the protein coating density to maintain the specific binding frequency at around 20% (mostly single bond based on Poission distribution), it is of equal importance to ascertain that non-specific binding is below 5%. As we did for controlling specificity of L-selectin/PSGL-1 binding, the distance between receptor/ligand coated surfaces was monitored to give optimal results.

As shown in Figure 5.3 below, we coated the Petri dish surface using 10ug/ml A1 protein. 10ul of protein in PBS buffer was coated on two labeled spots (blue spots in the figure) and kept overnight in a 4^{o}C refrigerator. On the day of the experiment, the coating spots were washed three times by PBS to remove excessive protein. Then 5ml 1% BSA in PBS was filled in the Petri dish to block non-specific binding, mainly from electrostatic interaction between bare surfaces. The AFM tip was coated by 10ug/ml glycocalicin (extracellular domain of GPIbα) overnight at 4^{o}C. Another tip was coated by 1% BSA in PBS solution as a control. On the day of the experiment, a glycocalicin coated (specific) tip was soaked in 1% BSA (in PBS) solution to block non-specific binding. Although small molecule BSA would cover most bare surfaces, there might still be non-specific binding from electrostatic or hydrophobic interactions between two opposing surfaces. To decrease the percentage and impact of such non-specific binding in our experiments, we separated further the AFM tip from the Petri dish to minimize their non-specific interaction. Therefore, before we measured the specific interaction, we quantified how increasing the distance between two surfaces would lower non-specific

and specific binding frequencies and whether we could find the proper distance at which to harvest specific binding data with minimum non-specific binding. As shown in Figure 5.3, three points were tested on either spot labeled on the Petri dish. Binding frequencies were counted for each point at various distances from the Petri dish surface. For each point, we built a binding frequency vs. distance curve. From these three points, an averaged curve was obtained as shown in Figure 5.5.

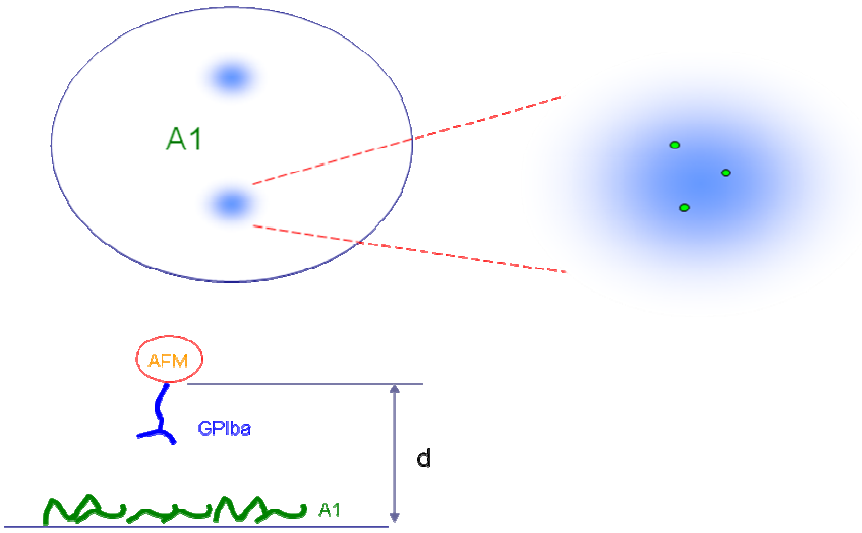

Figure 5.15: Diagram showing the experiment setup for physical adsorbed A1 protein on Petri dish and glycocalicin on AFM tip, distance d is controlled to suppress the non-specific interaction but still with enough specific binding frequency.

Both non-specific (BSA/A1) and specific (glycocalicin/A1) interactions were tested for the distance effects on binding frequency. Data show both the non-specific and specific binding frequency decreased with increasing distance of the AFM tip from the Petri dish surface. Distance is calculated from the piezo position of "500ms holding phase" subtracting the "zero distance" position. The "Zero distance" piezo position corresponds to the starting bending point at which the AFM tip and the cantilever just begin to push down on the Petri dish (Figure 5.4). A negative distance measurement means the AFM tip was still in contact with the surface and there was a downward bending of the cantilever causing an indent force on the Petri dish surface.

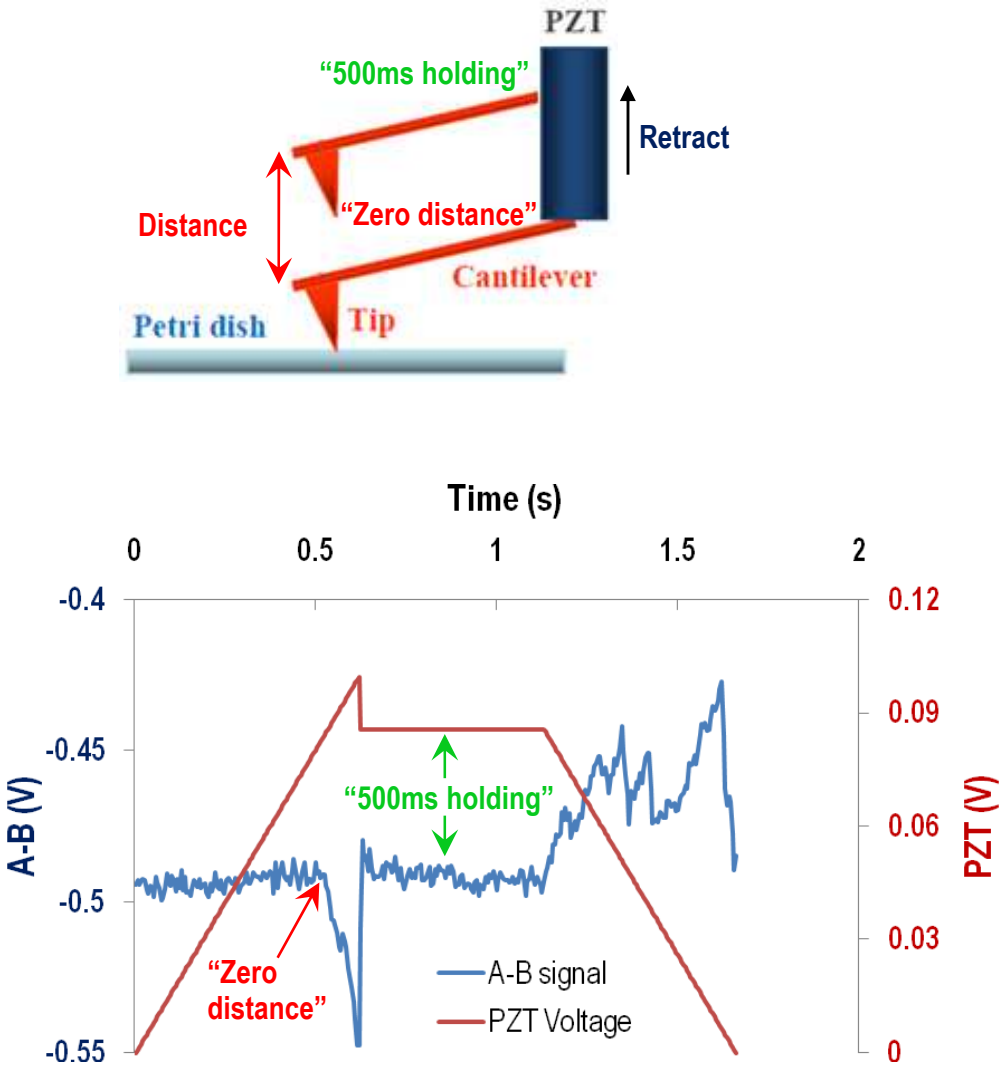

Figure 5.16: Distance calculation from A-B signal time trace. The piezo was retracted to a preset distance and held for 500ms ("500ms holding" phase, green arrows) before further retraction, to test whether there was any adhesion. The AFM tip contact point with the Petri dish was determined by the A-B signal's sudden decrease (red arrow), where "zero distance" position was used to determine AFM tip's distance from surface.

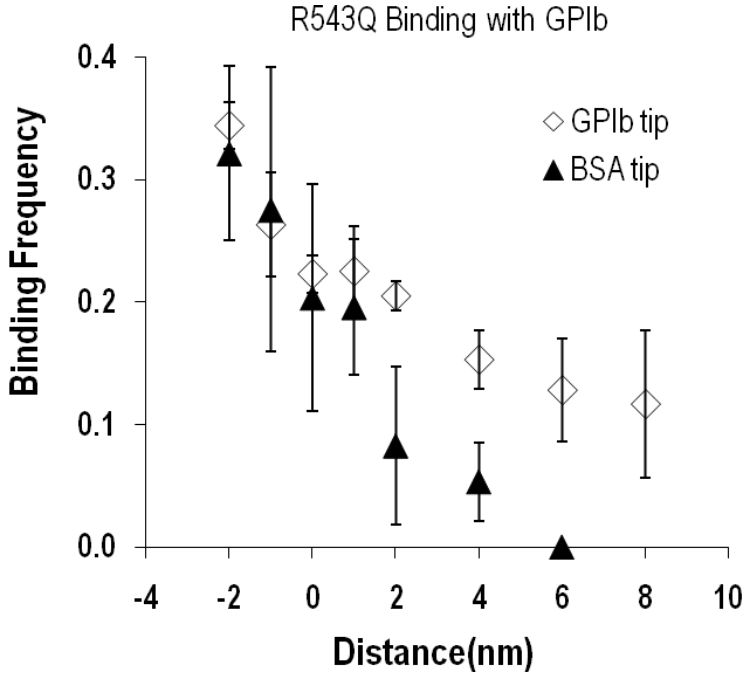

Figure 5.17: With the distance increase of AFM tip from Petri dish, the decrease of specific binding (A1-R543Q/GPIb interaction) frequency is slower than the decrease of non-specific binding (BSA/GPIb) frequency. Therefore, we take 4nm as starting distance to suppress non-specific binding while still can harvest specific binding. WT and R687E mutant A1 shows similar behavior.

Using the above method to quantify the non-specific binding frequency, the assumption is that if three points from one coated spot gave less than 5% binding frequency consecutively, then the spot would be deemed to have low enough non-specific binding. We found that coating concentration and protein length had very obvious effects in affecting the non-specific binding, that is, higher coating concentration would lead to higher non-specific binding frequency, and would need a longer distance to suppress; longer protein would also need longer suppressing distance. From Figure 5.5, we can also observe the much slower decrease of specific binding frequency compared with non-specific binding frequency. Non-specific interaction mainly came from the electrostatic and van der Waals interaction between the Petri dish surface and the AFM tip. This interaction is highly dependent on distance, as the van der Waals force has 10^{-6} dependence on distance. Coulomb's law gives a 10^{-2} dependence of attraction force on

distance between two opposite charges. In contrast, glycocalicin coated AFM tips would have longer range of effective binding distance because the molecules could assume different orientation and conformation in the buffer. On the other hand, glycocalicin molecules had much longer molecular lengths than BSA; this feature further increased the effective binding range. For our experiments, we could only control the distance between the AFM tip and the Petri dish surface. The goal is to diminish the electrostatic interaction between the AFM tip and the Petri dish because we believe that is the major reason for non-specific interaction. In our assumption, the possibility of glycocalicin binding to the Petri dish surface or A1A2A3 binding with an AFM tip (silicon nitride) is minimal.

Because the non-specific binding frequency was lower than 5% at 4nm distance, we would use 4nm distance as the starting value for every experiment. If the spot could give three consecutive points with less than 5% non-specific binding frequency in 50 contacts, we would assume the coating spot to be good enough for the subsequent specific measurement. Otherwise, we would increase the distance to decrease the non-specific binding until we found an appropriate distance. In some cases, the distance value was so high that we would not get enough specific binding. Then we would prepare the next sample.

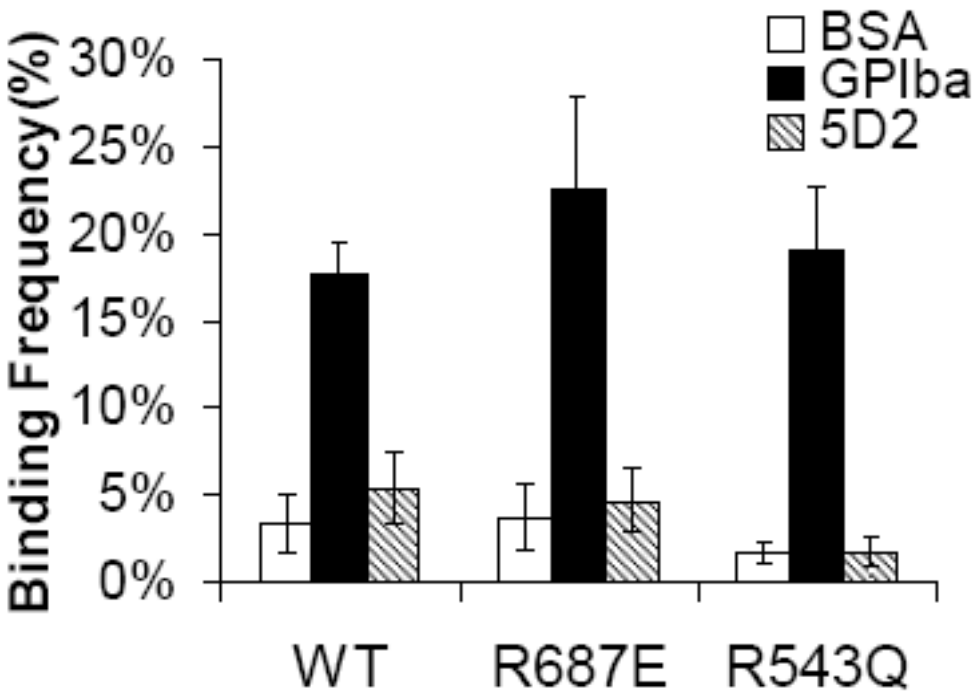

Figure 5.18: VWF-A1 mAb 5D2 blocks GPIb binding with WT, R687E and R543Q mutants. (5D2 was generous gift from Dr Robert Andrews of Monash University)

Besides distance control, we also tested the binding specificity by using antibody 5D2. The monoclonal antibody 5D2 is of the IgG1 subtype; it has been characterized as anti-VWF-A1 antibody that can strongly inhibit both ristocetin- and botrocetin-dependent binding (76, 88). For a control experiment, we tested the binding frequency of a BSA-coated AFM tip and glycocalicin-coated tip with VWF-A1 coated Petri dish surface. We added 25ug/ml 5D2 into buffer and the Petri dish was put on a lab rocker for 10 minutes' mixing to block VWF-A1. The glycocalicin coated AFM tip would then be applied to test the binding frequency again. As shown in Figure 5.6, glycocalicin coated AFM tips had much higher binding frequency than BSA coated tips. After adding the VWF-A1 blocking mAb, 5D2 inhibited all the binding between WT/R687E/R543Q and glycocalicin.

GPIbα Forms Catch Bonds with WT VWF-A1 but not with R543Q and R687E Mutants

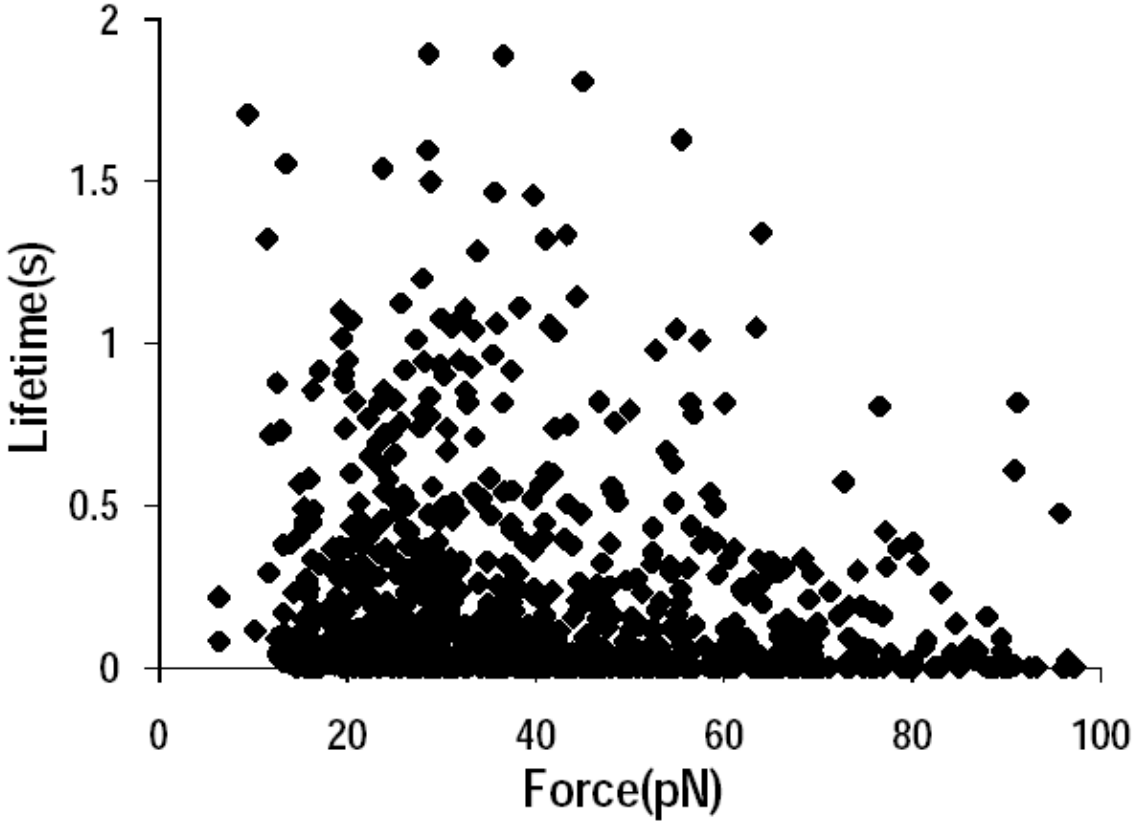

Figure 5.19: Scatter plot of over 800 lifetime measurements for GPIbα interacting with wild-type VWF-A1.

After confirming the binding specificity, we continued to use the force clamp routine to harvest lifetimes (Figure 5.7). The lifetimes of GPIbα/A1 bonds were measured in thousands of repeated test cycles. Each cycle consisted of moving the cantilever tip to touch the Petri dish for 0.02 s, retracting it ~4 nm above the surface and holding it for 1 s to allow for bond formation. It is then further retracted to a predetermined distance to see if binding occurs, and, if so, to determine if the bond survives ramping to the preset force and if it does, to measure how long the bond lasts at that force (i.e., bond lifetime). At the end of this process, the cantilever tip is finally retracted to the starting position. Suspending the cantilever tip ~4 nm above the surface in the bond formation phase

usually reduced nonspecific binding to <5% of the test cycles, whereas specific GPIb/A1 binding occurred at ~20% of the test cycles. A large number of mostly single-bond lifetimes were measured to derive the mean lifetime (which equals the reciprocal off-rate $1/k_{off}$ for first-order dissociation of single bonds) over a range of forces.

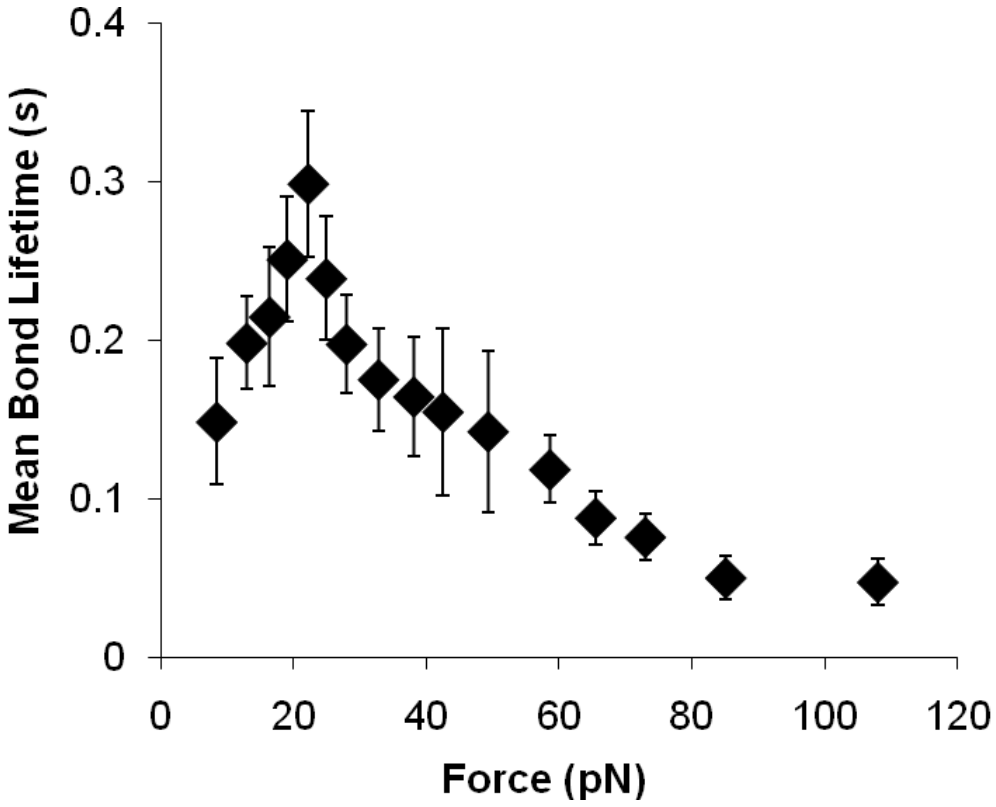

Figure 5.20: Mean bond lifetime vs. force data shows GPIbα forms catch-slip transitional bonds with WT VWF A1 as force increases.

Figure 5.8 shows the analysis results based on a different force bin. Interestingly, it shows a catch-slip transitional bond. The lifetimes of GPIbα/A1 bonds exhibited a biphasic pattern characteristic of transition from catch to slip bonds. The mean lifetime increased with increasing force, indicating the presence of catch bonds, until an optimal force ~23pN was reached where the lifetime reached a maximum value at around 0.3 seconds. Thereafter, the mean lifetime decreased with increasing force, indicating the presence of slip bonds. To confirm this catch bond behavior, we zoomed in using the low force range and did a strict examination of the bond lifetime, as shown in Figure 5.9. The

upper panel shows the scatter plot of lifetime raw data in different colors, representing different force bins. The continuity in distribution of lifetimes in each force bin suggested that the data was not biased by different populations. The ln[(# of measurements with a lifetime > t)/(total number of measurements)] in each force bin analysis also exhibited a decrease in –slope value with increasing force, suggesting the off-rate decrease with increasing force. Combined with the catch bond observation for selectin/PSGL-1 system, GPIbα/A1 is the second molecular system showing catch bond observation (29). As to P- and L-selectin/PSGL-1, the catch bond has been shown to help recruit leukocytes to the inflammation site; the L-selectin/PSGL-1 catch bond also helps prevent inappropriate aggregation of leukocytes. The GPIbα/A1 catch bond has been shown to be the molecular mechanism for flow enhanced adhesion of platelets to the site of vascular injury (29).

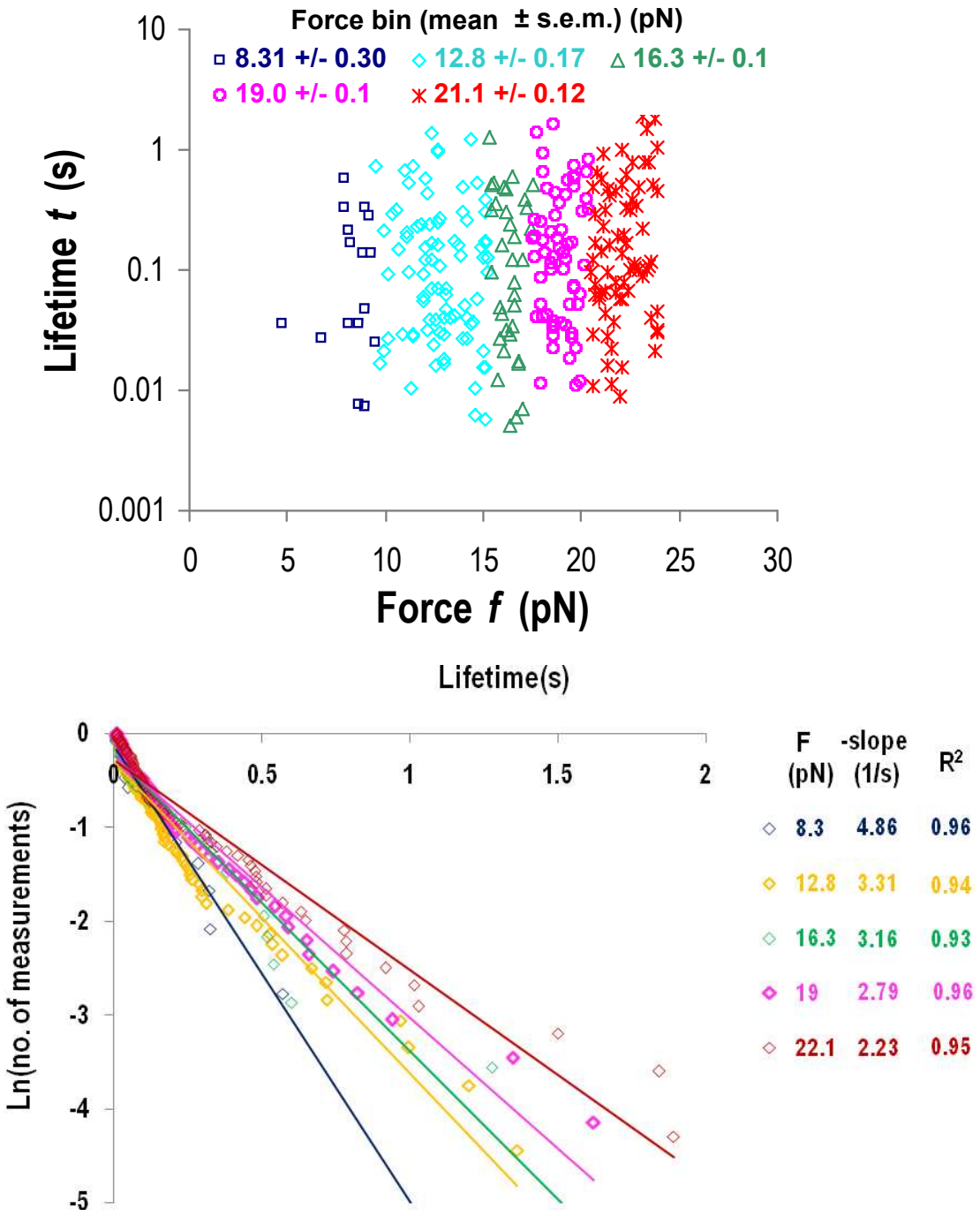

Figure 5.21: Scattergrams in the five force bins which were used to obtain the five average lifetime vs. average force data in the catch bond regime shown in Figure 5.8, and lifetime distributions, i.e., ln[(# of measurements with a lifetime > t)/(total number of measurements)] in each force bin measured by AFM.

After observing the catch bond for GPIbα/WT-A1 interaction, we continued measuring the lifetime for gain-of-function (GOF) A1 mutants R687E (or R687E) and R543Q (or R543Q). These two A1 mutants have been shown to be related to type 2B von Willebrand disease (VWD). The R543Q mutant naturally occurs in patients with type 2B VWD(89). Mutant R687E was designed to mimic the gain-of-function phenotype of type 2B VWD. GPIbα is thought to bind with higher affinity to these gain-of-function mutants of A1 than to WT A1. Figure 5.10 shows the mean bond lifetime vs. force curve for R543Q GOF A1 mutant.

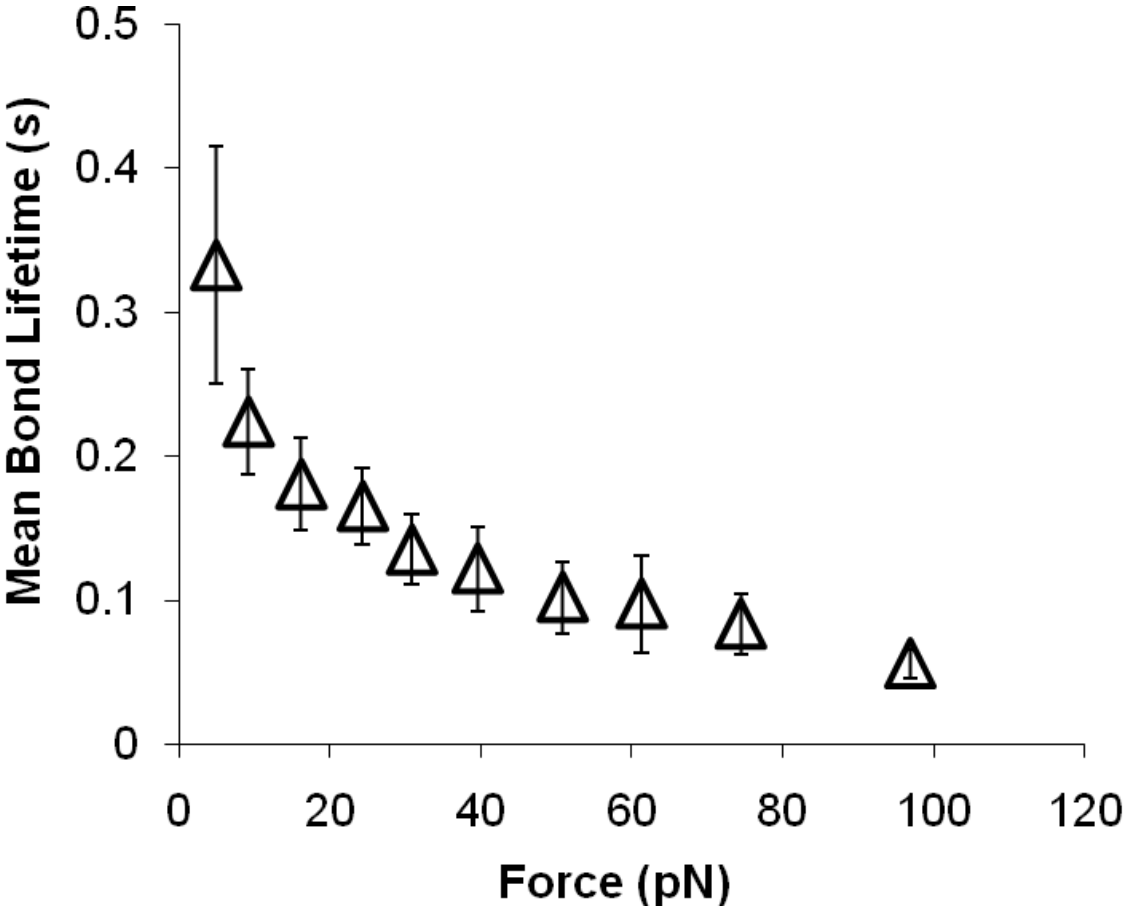

Figure 5.22: Mean bond lifetime vs. force for R543Q A1 mutant interacting with GPIbα. Error bars are standard error of the mean.

In sharp contrast to the catch-slip bond observed for WT-A1 interacting with GPIbα, R543Q totally eliminated the catch bond and only showed a monotonous decrease

of mean bond lifetime in the whole force range, indicating a slip bond behavior. The elimination of catch bonds resulted in longer bond lifetime at low force regime. At about 5pN, R543Q's mean bond lifetime was over 0.3 seconds, while WT-A1 gave only about 0.1 second bond lifetime, with possible extrapolation toward even lower force. With the continuous decrease, R543Q had lower bond lifetime than WT-A1 when the force value exceeded ~15pN. The difference between the two curves was maximal at the peak of WT-A1, giving a comparison of 0.75 seconds vs. 0.3 seconds for R543Q and WT-A1, respectively. This difference diminished when force kept increasing until finally the two curves collapsed after ~60pN. For R543Q, the three-fold higher lifetime at low force may explain the enhanced adhesion between platelets/GPIbα coated microspheres with A1 coated parallel plate flow chamber wall(29).

To confirm our observation of this elimination of catch bond for R543Q A1 mutant, we strictly scrutinized the low force lifetime measurements and compared with WT-A1 data, as shown in Figure 5.11. The scattergram shows a continuous decrease of value distribution, which forms a sharp contrast to the continuous value increase in the distribution of WT-A1/GPIbα lifetime value. The ln[(# of measurements with a lifetime > t)/(total number of measurements)] in each force bin analysis also exhibited an increase in –slope value with increasing force, suggesting an off-rate increase with increasing force, typical of slip bond behavior. The change in –slope value was not as obvious as for the WT-A1 case, suggesting a much smoother variation in the bond kinetics change with increasing force.

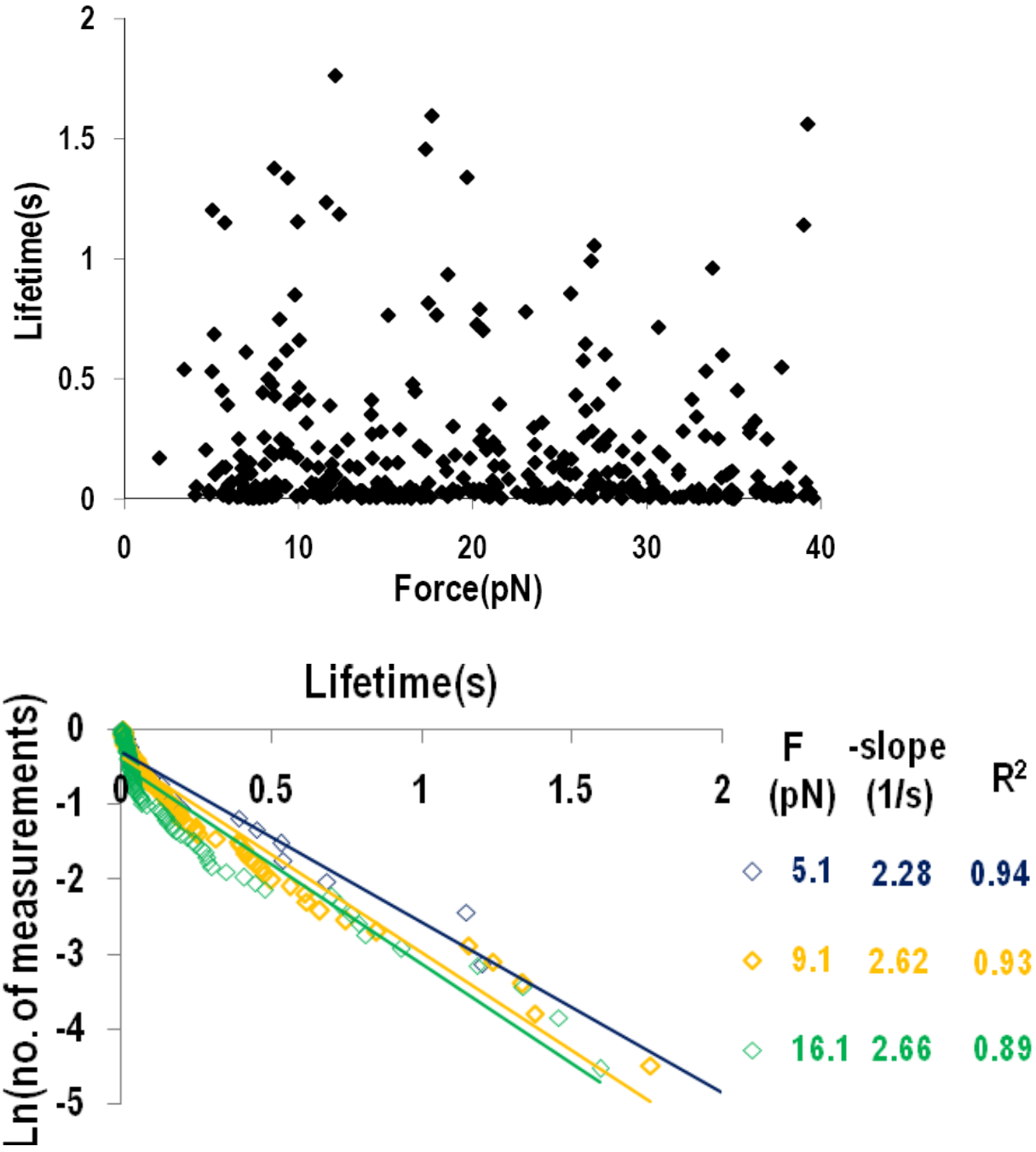

Figure 5.23: Scattergram of low force lifetime measurements used to obtain the three average lifetime vs. average force data shown in Figure 5.8, and lifetime distributions, i.e., ln[(# of measurements with a lifetime > t)/(total number of measurements)] in each force bin measured by AFM.

An interesting observation for the analysis of ln[(# of measurements with a lifetime > t)/(total number of measurements)] in each force bin is that the data points were not aligned very well with the fitted line, suggesting there could be other factors contributing to these effects. Binding pocket difference for GPIbα/A1 could be one possibility. It has been reported that A1 could adopt different conformational states. For our physical adsorption protocol, A1 could have already been activated. But chances are that part of the molecule population remained inactive. Furthermore, A1 could also be partially/wholly unfolded, based on previous studies (60). The repeated stretching of A1 by GPIbα could be the cause of partial/complete unfolding, thus affecting the conformation upon bond breaking. It has also been reported that the type 2B mutation could result in a different conformation of the A1 molecule (67, 68). This way, the binding interface of GPIbα/A1 could be different for WT-A1 and R543Q mutants, leading to the observed difference in bond kinetics behavior.

If the R543Q A1 mutant showed elimination of the WT-A1 catch bond, another GOF mutant R687E could also eliminate the catch bond. To test this hypothesis, we measured the bond lifetime of GPIbα/R687E, as shown in Figure 5.12. Similar to the R543Q mutant, the R687E mutant also showed a monotonous decrease in mean bond lifetime with increasing force, or slip bond behavior. We harvested more large value lifetimes under the low force regime, prolonging the mean bond lifetime even longer than was the case for the R543Q mutant. Except for the difference at the catch bond regime, R687E collapsed with WT-A1 data at the slip bond regime. The observation of sharp decrease in lifetime at low force regime was repeated for the scattergram, and slopes of ln[(# of measurements with a lifetime > t)/(total number of measurements)] were established at each force bin, as shown in Figure 5.13.

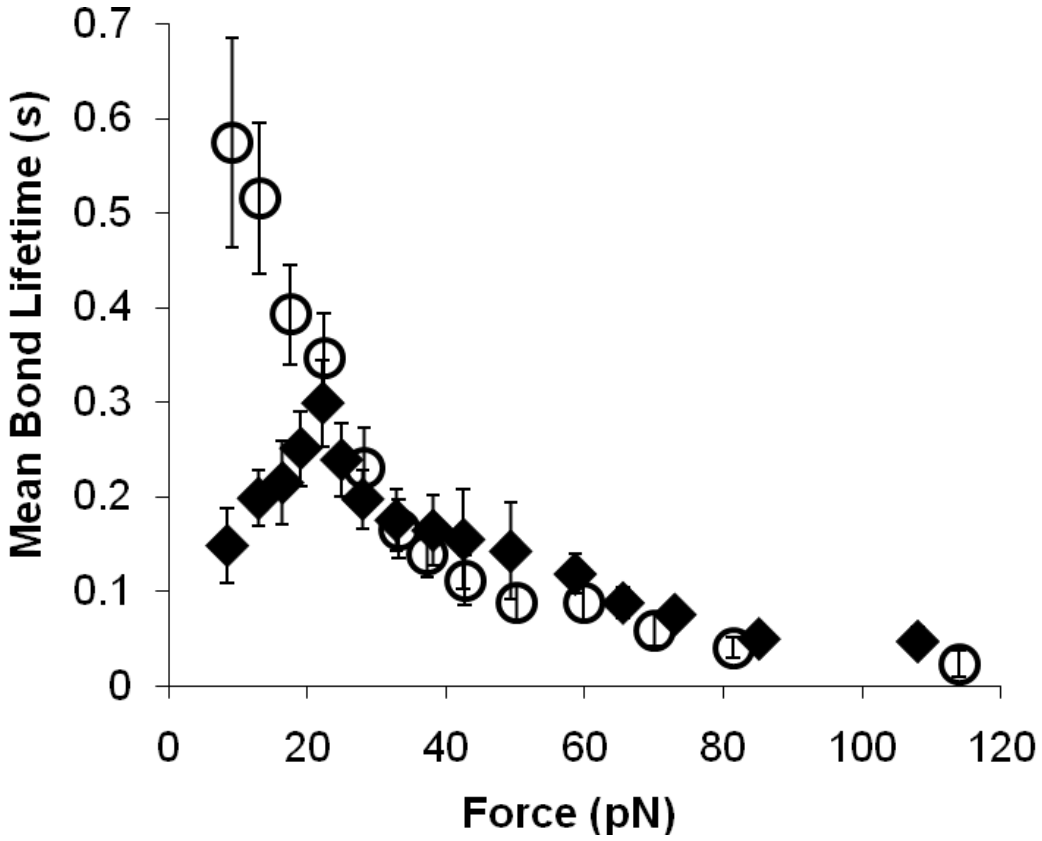

Figure 5.24: Mean bond lifetime vs. force for R687E A1 mutant (circle) interacting with GPIb*α*, in comparison with WT-A1 data (solid diamond). Error bars are standard error of the mean.

Compared with the R543Q data analysis in Figure 5.11, R687E gave a clearer trend in the off-rate (-slope) increase in the four force bins. There were still slope transitions in the ln[(# of measurements with a lifetime > t)/(total number of measurements)] analysis, but these were not as obvious as those in R543Q. The observation of longer lifetime for the R687E mutant than for R543Q at low force is consistent with the previous studies showing that R687E had more evident "gain of function" in the "shear induced platelet aggregation" (SIPA) and "ristocetin induced platelets aggregation" (RIPA) assays. This change in binding kinetics may come from different binding interface or conformation for this mutant A1 protein.

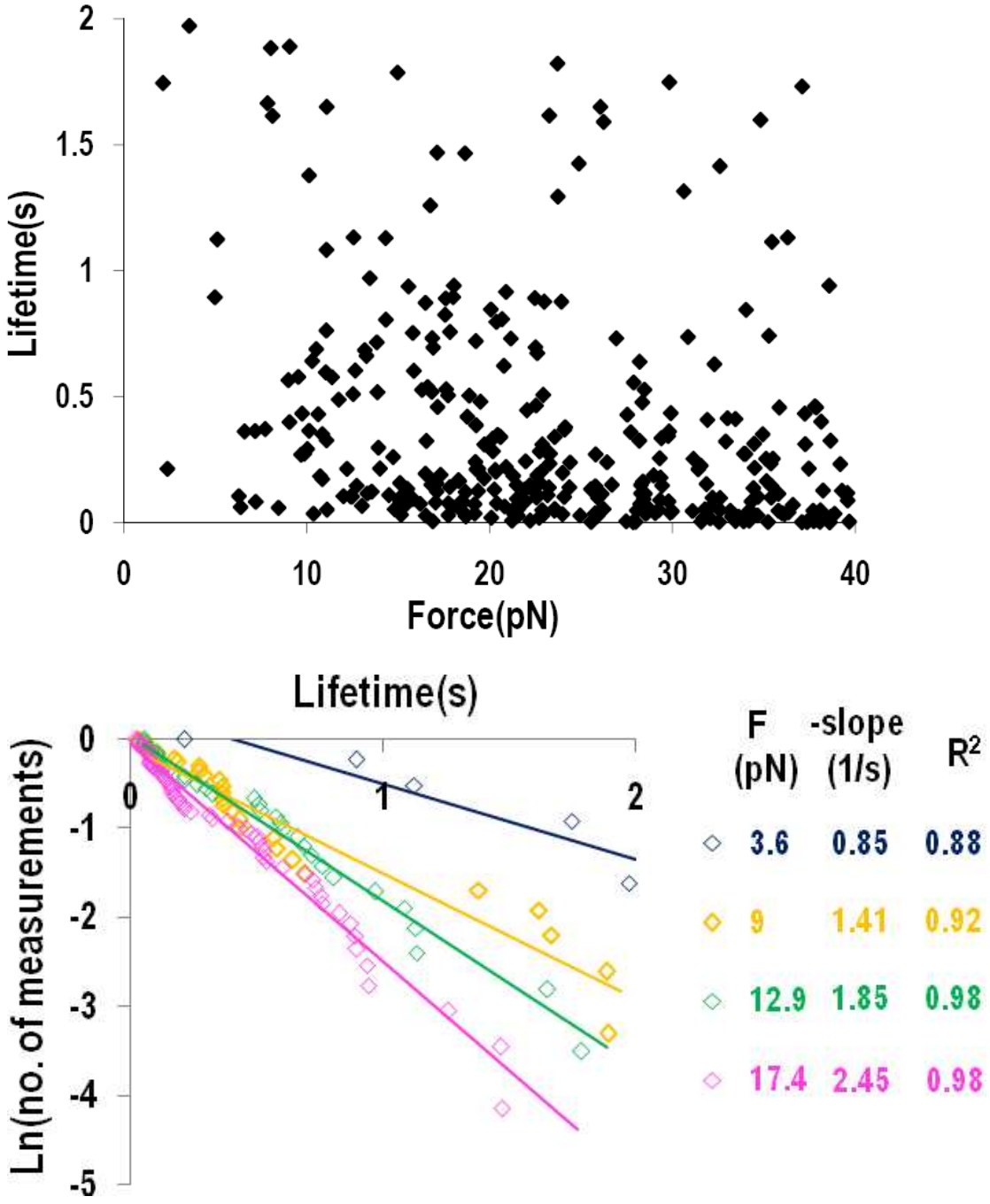

Figure 5.25: Scattergram of low force lifetime measurements used to obtain the four average lifetime vs. average force data shown in Figure 5.12, and lifetime distributions, i.e., ln[(# of measurements with a lifetime > t)/(total number of measurements)] in each force bin measured by AFM.

Discussion (adapted and modified from (29))

"The above findings of force regulated binding kinetics for WT and two GOF mutants A1 interacting with GPIbα were complemented by flow chamber studies and SMD simulation. In summary, flow chamber data showed that catch bonds caused platelets and GPIbα-coated microspheres to roll slower on VWF or WT A1 as flow increased below suboptimal shear; this explains flow-enhanced rolling. Longer bond lifetimes at low forces eliminated the flow requirement for rolling on R543Q and R687E A1(29). Flowing platelets agglutinated with microspheres bearing R543Q or R687E A1 or A1A2A3-triplets but not with WT A1 or A1A2A3. Therefore, catch bonds may prevent VWF multimers from agglutinating platelets. Steered molecular dynamics simulations of GPIbα dissociating from A1 suggested mechanisms for catch bonds that A1 mutations lack(29).

These findings demonstrate how force regulates platelet rolling on VWF, illustrate its similarity to force regulation of leukocyte rolling through selectins, suggest a structural basis for this regulation, and offer insights into the molecular basis for type 2B VWD.

The counterintuitive "arterial flows enhanced platelet adhesion to VWF" was noted over a decade ago but was not explained (7, 38, 84). The flow chamber study demonstrates how flow strengthens rolling adhesion through slower and more regular rolling steps (Figures 1, 3, and 4 of (29)), which are governed by the off-rate of dissociation of GPIbα/VWF bonds. By measuring the force-dependent lifetimes of single bonds or tethers between purified or platelet-expressed GPIbα and the VWF A1 domain at forces lower than those previously studied, we directly demonstrated transitions from catch bonds to slip bonds by using the AFM data and flow chamber tether lifetime data. Previous studies only observed slip bonds at higher forces. Second, by scaling the analysis of platelets and GPIbα-bearing microsphere rolling on intact VWF or VWF A1

domain ((29) Figures 1, 3, and 4), we showed that force-dependent dissociation kinetics of GPIbα/VWF interactions governed rolling velocity and that catch bonds specifically governed flow-enhanced rolling, i.e., the ability to roll more slowly and more regularly as flow increases from a suboptimal rate. As flow increased above the optimal rate, catch bonds transitioned to slip bonds and rolling velocities increased. The interactions of P-selectin and L-selectin with their glycosylated ligands also transition from catch to slip bonds as force increases, and catch bonds govern flow-enhanced leukocyte rolling through L-selectin. Thus, two structurally distinct receptor/ligand systems use catch bonds to enable flow-enhanced rolling of blood cells on vascular surfaces.

Besides, two single-residue substitutions in the VWF A1 domain, R543Q and R687E, were used to further explore the force regulation of GPIbα/VWF interactions. Both VWF mutants exhibit features of type 2B VWD and both have increased affinity for GPIbα in the absence of force. Extending this result, we observed that bond lifetimes of both A1 mutants with GPIbα were longer at low forces, eliminating catch bonds and resulting in a monotonic shortening of bond lifetimes (slip bonds) as force increased. These mutations eliminated the shear threshold requirement for platelet or GPIbα-bearing microsphere rolling on VWF and strengthened the causal relationship between rolling velocity and the dissociation kinetics of GPIbα/VWF bonds. Single-residue substitutions in the hinge between the lectin and EGF domains of L-selectin (30) or in the ligand-binding surface of L-selectin (90) similarly prolong bond lifetimes at low forces and reduce (30) or eliminate (90) the shear threshold for leukocyte rolling. Catch bonds provide a mechanism to support platelet rolling on VWF immobilized on surfaces but to prevent inappropriate agglutination of circulating platelets by binding to VWF multimers in plasma. Consistent with this notion, flowing platelets agglutinated with microspheres bearing R543Q or R687E A1 or R687 A1A2A3 but not with WT A1 or WT A1A2A3. Similarly, flowing leukocytes, which express the L-selectin ligand PSGL-1, do not

agglutinate with microspheres bearing WT L-selectin but do agglutinate with microspheres bearing L-selectin mutants that prolong lifetimes at low forces (30). Thus, catch bonds may provide a general mechanism for blood cells to adhere to vascular surfaces but not to agglutinate as they circulate.

Crystal structures of GPIbα/VWF A1 complexes have provided important information on the molecular details of the interactions, but they do not indicate how the complexes respond to applied force and they have not readily explained how type 2B VWD mutations in the A1 domain clustered outside the binding site can alter function. The SMD simulations of dissociation of the WT GPIbαN:A1 complex enabled us to visualize dynamic conformations not seen in the equilibrium conformations of the crystal structures, to determine how force regulates these conformational changes, and to assess how such changes might elicit catch bonds. These simulations suggest that force breaks interactions of D1269 with R543 or R687 in the A1 domain, causing A1 to rotate and slide along the interface with GPIbα. The sliding allows R1334 in A1 to form a strong salt bridge with E14 in GPIbα that delays dissociation of the molecular complex after all atomic-level interactions seen in the crystal structure have disrupted. This provides a structural mechanism for the experimentally observed catch bonds. Remarkably, the sliding-rebinding mechanism resembles that observed in SMD simulations of P-selectin dissociating from its ligand PSGL-1, where force breaks interactions at the lectin-EGF domain interface, causing the lectin domain to rotate and to form new interactions as it slides along the interface with PSGL-1(91). A mutation that disrupts an interaction between the lectin and EGF domains of L-selectin reduces the force required to rotate the lectin domain and to slide along the interface with its ligands (30).

Free dynamics and SMD simulations of dissociation of the mutant GPIbαN:A1 complex have provided explanations for the gain-of-function phenotype and the elimination of catch bonds by the R543Q mutation; this may also explain the effects of

the R687E mutation. In the model, the mutation results in formation of the E14:R1334 salt bridge at zero force and no new contacts after force is applied. An alternative model similar to one previously proposed (30) suggests that the R687E mutation removes the interaction with D1269, which allows the sliding-rebinding mechanism to allosterically prolong lifetimes at nearly zero forces. The same mechanism can explain the gain-of-function phenotype of the H1268A/D1269A A1 mutant (92), because the D1269A substitution also eliminates the salt bridge(s) with R543 and R687.

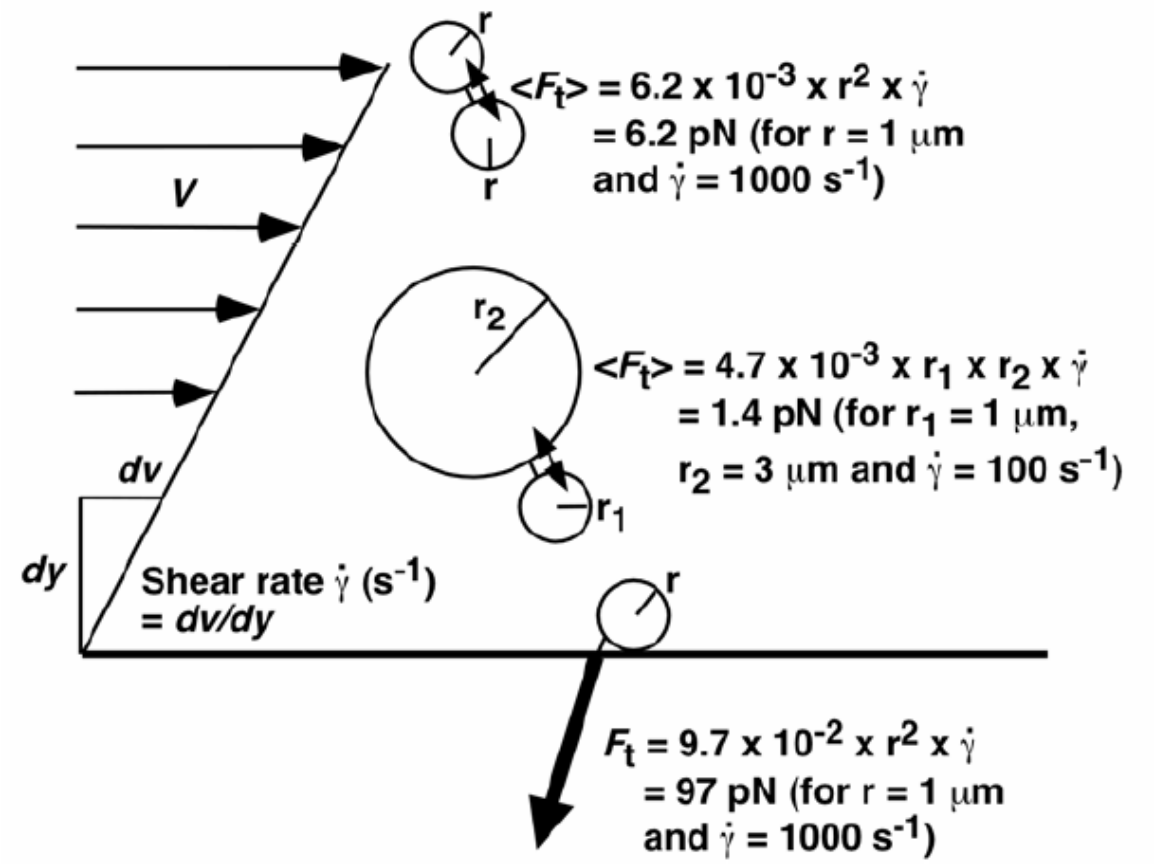

Figure 5.26: At the same shear rate, tensile force applied to bonds that link flowing platelets or microspheres is much lower than that applied to bonds that tether rolling platelets or microspheres. The schematics show tensile forces between two spheres of equal or unequal sizes in a doublet or between a sphere and the wall under a simple shear field.

Our data provide a biophysical mechanism for the phenotypes of patients with type 2B VWD. The platelet-binding activity of VWF increases with the size of the multimers, which may assume different conformations to expose binding sites for GPIbα on A1 domains (93, 94). In thrombotic thrombocytopenic purpura, ultralarge multimers may be particularly capable of exposing very large numbers of binding sites on A1 domains that spontaneously agglutinate circulating platelets (95). However, the number of exposed binding sites in plasma VWF multimers of normal size cannot stably agglutinate platelets because the lifetimes of A1 bonds with GPIbα are too short at arterial shear rates (500 to 5,000 s^{-1}). Shear-induced platelet aggregation only occurs at

the very high shear rates, e.g. 20,000 s^{-1}, found in stenotic arteries (96, 97). At these shear rates, the forces applied to platelet doublets linked by VWF multimers are sufficiently large to elicit catch bonds (see Figure 5.14), which prolong bond lifetimes enough to agglutinate circulating platelets. Extremely high shear rates may also expose more binding sites for GPIbα on A1 domains of normal-sized multimers (96, 97). In type 2B VWD, the longer lifetimes of VWF with GPIbα at low forces enable plasma VWF multimers to bind stably to circulating platelets. This explains the ability of these VWF mutants to spontaneously agglutinate platelets in vitro at shear rates as low as 200 s^{-1} or in response to low concentrations of a modulator such as ristocetin (60). Our data demonstrate that the mutations directly affect the mechanical properties of isolated A1-domain bonds with GPIbα, but they do not exclude an additional effect of the mutations to expose more A1 domains on VWF multimers. In vivo, the enhanced binding also agglutinates platelets, which depletes larger VWF multimers from plasma and may cause thrombocytopenia. Furthermore, flow exerts force on the VWF that agglutinates platelets, exposing the cleavage site for the protease ADAMTS-13, thus further reducing the larger VWF multimers (98, 99). Bleeding results from depletion of larger VWF multimers from plasma, limiting their availability for binding to collagen on disrupted vascular surfaces, and from occupancy of GPIbα by plasma VWF, preventing interactions with collagen-bound VWF."

Binding kinetics of type 2M VWF-A1 with GPIbα

As opposed to the type 2B GOF mutants, type 2M mutants of VWF-A1 exhibited a loss of function in the SIPA and RIPA assay compared with WT A1. The type 2M VWD phenotype is characterized by a decreased platelet-dependent function of plasma VWF, associated with a normal multimeric pattern (100). It is of particular interest for us to use the single molecular technique to study the biophysical properties of these LOF mutants interacting with GPIbα, as compared with the GOF kinetics data described above. We hypothesized that the LOF mutants will exhibit different kinetics during binding with GPIbα.

The AFM experimental setup and protocol was similar to that used in the previous GOF studies. The only difference was that we replaced the protein coated on the Petri dish surface by type 2M mutants. We have tried three type 2M mutants, which were V516I, G561S and P704S. Figure 5.15 shows the mean bond lifetime vs. force curve for GPIbα/V516I bond. It has several characteristics. First, the V516I LOF mutant also formed catch-slip bonds with GPIbα. Second, this catch-slip bond had an obvious shift towards larger force: WT-A1's catch bond peaked at around 23pN, while V516I's catch bond peaked at around 39pN. The peak lifetime values were about the same, giving ~0.25 seconds and ~0.3 seconds for V516I and WT-A1, respectively. Third, the catch bond shifted towards larger forces, resulting in much lower lifetime at low force regime. The lowest point for the V516I curve at low force was at around 15pN, giving mean bond lifetime a value of around 0.04 seconds. In sharp contrast, WT-A1 gave a mean lifetime value of around 0.2 seconds at 15pN. Figure 5.16 shows the lifetime vs. force curve for another LOF mutant, G561S. It exhibited behavior similar to that of V516I, except that the shift showed more obviously that the slip bond regime had a larger value than the WT-A1 data.

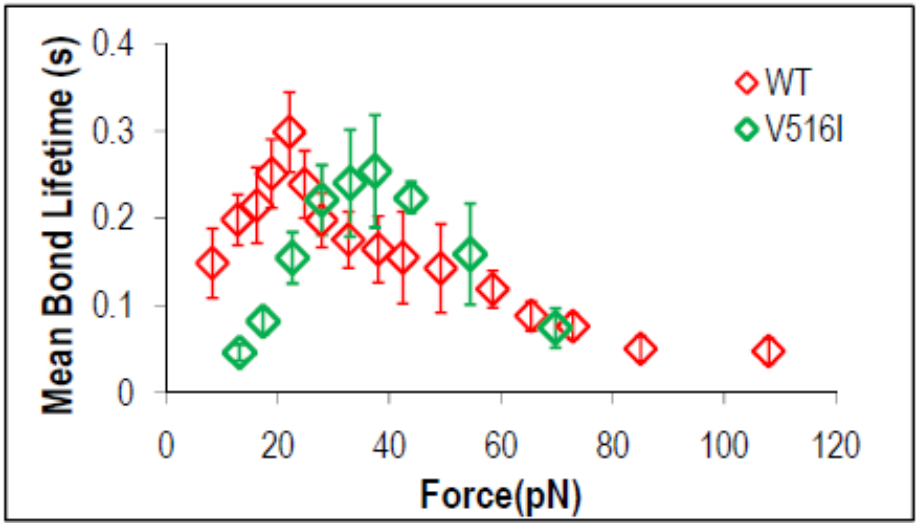

Figure 5.27: Mean bond lifetime vs. force of V516I LOF mutant (green) interacting with GPIbα, in comparison with GPIbα/WT-A1 (red) bond.

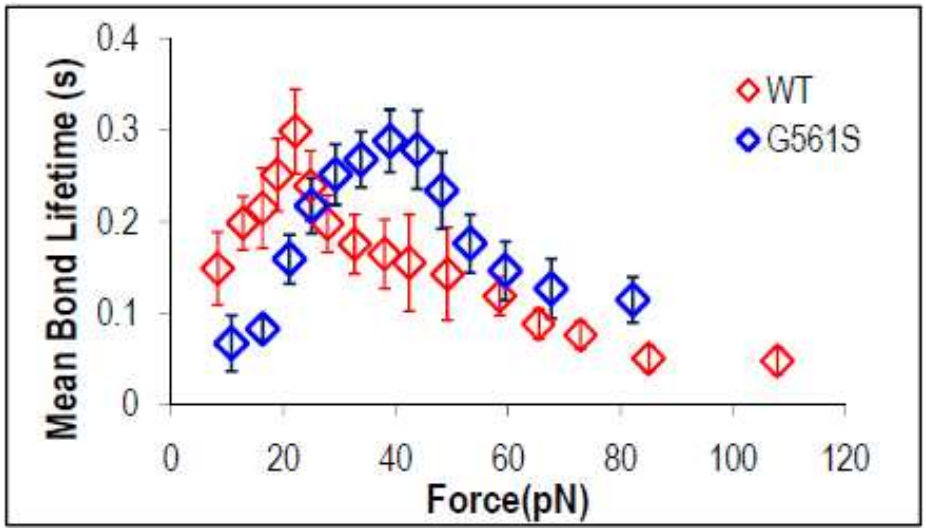

Figure 5.28: Mean bond lifetime of G561S LOF mutant (blue) interacting with GPIbα, in comparison with GPIbα/WT-A1 (red) bond.

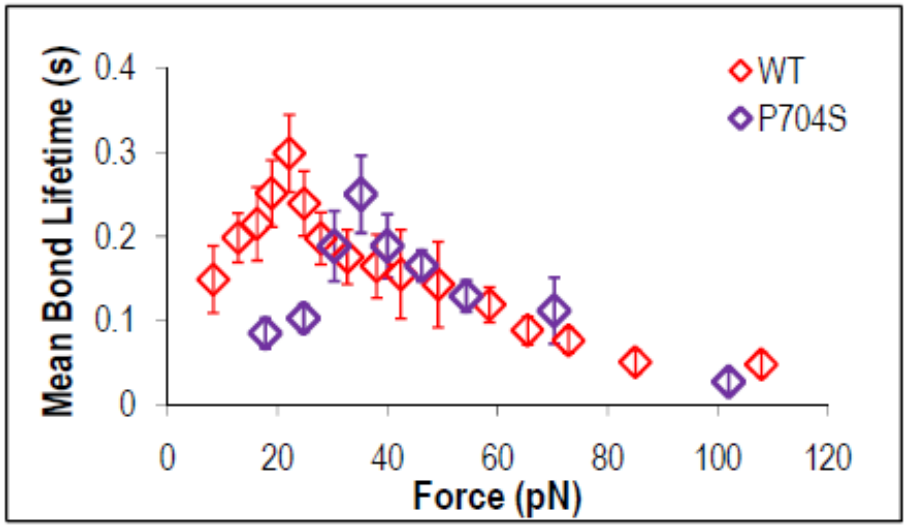

Figure 5.29: Mean bond lifetime of P704S LOF mutant interacting with GPIbα, in comparison with GPIbα/WT-A1 bond.

Figure 5.17 shows the bond lifetime vs. force data for the third LOF mutant P704S. Again, it exhibited a shift in the catch-slip bond as V516I and G561S did. The slip bond regime collapsed well with the WT-A1 data.

Discussion

Because all three LOF mutants showed the same shift of catch-slip bond, we believe this behavior for LOF might be a typical kinetics for other LOF mutants. It has been shown previously that at high shear rates of ~4000 seconds^{-1} none of the type 2M VWFs was able to induce any measurable aggregation compared with WT-VWF. And this loss of binding function was also similar for ristocetin- but not botrocetin-dependent platelet binding (100). This study suggested that type 2M VWFs resulted in VWF conformation change that made it insensitive to high shear rates and ristocetin. Botrocetin could induce a VWF conformation which is totally different from the conformation of VWF caused by ristocetin binding or high shear stress. Furthermore, botrocetin induced platelet aggregration in the presence of VWF is insensitive to WT VWF and type 2M VWF. In other words, type 2M mutants could cause a similar VWF conformation as WT-

A1 in the presence of botrocetin, but not the same as the VWF conformation in the presence of ristocetin or high shear. And this conformational similarity could come directly from the A1 domain. Our AFM experiments were all done without any A1 agonist, either botrocetin or ristocetin, or high shear condition. So the possibilities are that the three type 2M mutations had only slightly changed the conformation of the A1 domain, induced minor change at the binding interface for GPIbα-A1 bonds, and thus shifted the catch-slip bond quantitatively. This hypothesis was partly supported by the observation that none of the three LOF mutants is located in or directly next to the GPIbα-binding site. Therefore, the mutant induced conformational change could only be allosteric. Further experiments could be done in the presence of agonist ristocetin, to resemble the A1 confirmation in high shear condition. The hypothesis would be that type 2M mutant A1 would have a much decreased bond lifetime, or a much increased off-rate, over the WT-A1, when A1 adopts the conformation as under high shear rates. And the control experiments could be testing GPIbα-A1 binding kinetics in the presence of botrocetin.

Our findings provide new insights for type 2B and type 2M VWD, illustrate the different binding kinetics of GOF and LOF mutants, suggest possible structural basis for these functional differences, and propose a working hypothesis for future experiments.

Binding kinetics of VWF A1A2A3 domain triplet with GPIbα and collagen effects

Previously, we studied the binding kinetics of the WT A1 domain, two of its GOF, and three of its LOF mutants with GPIbα. The A1 domain is the core for VWF binding with GPIbα. At the same time, the other domains of VWF could also potentially affect the binding kinetics of A1. To dissect the effects from the A2A3 domain, we studied the binding kinetics of the A1A2A3 domain triplet with GPIbα, which could also provide a comparison to our previous A1 data. Figure 5.18 shows the AFM

measurements for the GPIbα/A1A2A3 bond lifetime, in comparison with the WT A1 data.

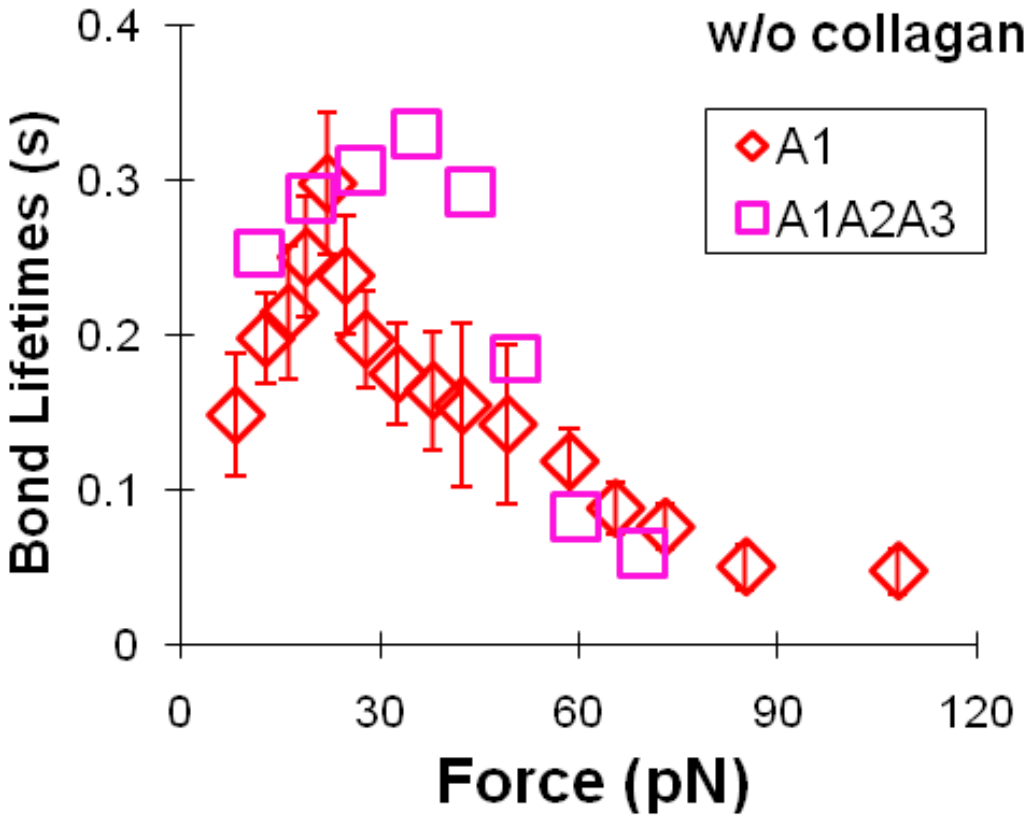

Figure 5.30: AFM measurements for GPIbα/A1A2A3 bond (pink square) lifetime, in comparison with WT A1 data (red diamond).

Compared with the WT-A1 data, the GPIbα/A1A2A3 bond shows a similar catch-slip transitional bond but with a different peak force and lifetime values. The peak force happened at ~35pN, larger than the WT-A1's 23pN peak force. The peak lifetime value for this experiment was slightly higher than that found for WT-A1, giving 0.32 seconds. In the catch bond regime (<35pN), lifetimes were generally higher than those found for WT-A1, and this difference started to decrease in the slip bond regime, collapsing with WT-A1 data after ~60pN. Therefore, A1A2A3 gave higher lifetimes than A1 when interacting with GPIbα in the whole force range.

During the process of hemostasis, circulating plasma VWF gets immobilized on the surface of the sub-endothelium by binding with collagen fiber. The immobilization of VWF on collagen would serve as an anchoring point for platelet-expressed GPIb to bind, and trigger the succeeding thrombus formation to stop the bleeding. Therefore, collagen binding with VWF is a very important step for recruiting plasma VWF to the site of vascular injury and would be of special interest to study. The immobilization of VWF on the collagen surface would also possibly affect the conformation, thus the binding kinetics, of A1 or A1A2A3. It is also not clear whether immobilization on collagen would change the difference between A1 and A1A2A3 when binding with GPIbα.

For AFM experiments, we used type III collagen (purified from human placenta) to coat the Petri dish surface. Collagen (10ug/ml) was physically adsorbed on the Petri dish surface overnight at 4^{o}C. At the start of the experiments, excess collagen protein was removed by washing three times by PBS buffer. A1 or A1A2A3 protein (1ug/ml) was applied on the collagen-coated surface for 1 hour secondary incubation under room temperature. During this incubation for collagen to capture A1/A1A2A3, a dampened paper towel was used to keep the incubation spot from drying out. Similar to our previous protocol, a BSA coated AFM tip was used first to characterize the non-specific binding level at a certain distance from the Petri dish surface. After confirming low enough non-specific binding frequency, the GPIbα coated AFM tip was loaded to run a force clamp program to harvest lifetimes at that distance. We have frequently observed long (>50nm) ascending phases, or dead zones, which might come from the length of collagen fiber. The collagen/A1 binding affinity has been reported to be in the scale of 10^{-7}-10^{-9} M, which is comparable to common antigen-antibody interaction. Therefore, this capturing would strongly support the lifetime measurement of GPIbα-A1/A1A2A3 bonds.

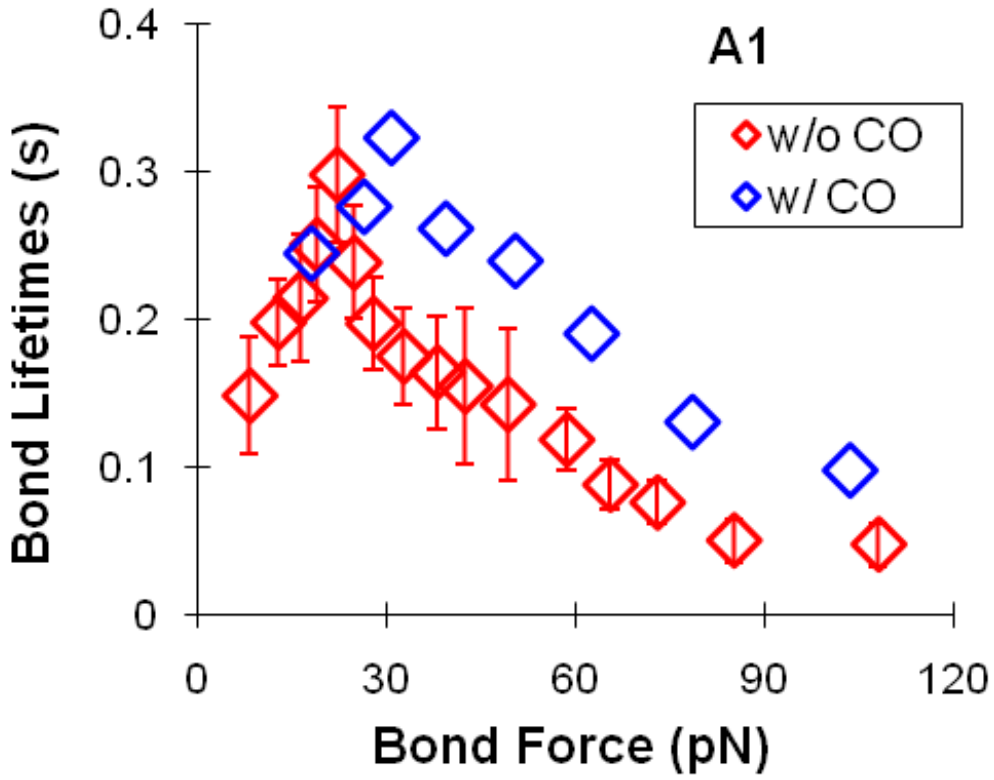

Figure 5.31: Mean bond lifetime vs. force curve for GPIbα binding with A1 captured by type III collagen (blue diamond), in comparison with WT-A1 data without collagen capturing (red diamond).

Figure 5.19 above shows the lifetime vs. force curve for GPIbα binding with A1 captured by type III collagen. Compared with WT-A1 lifetime data, collagen capturing has not changed the catch-slip transitional bond, but has resulted in a considerable shift of the curve. There was a further increase at the catch bond regime, reaching higher peak force (30pN) and lifetime (0.32 seconds) value. The slip bond regime was almost parallel to the WT-A1's slip bond, but with higher lifetime value at each force level.

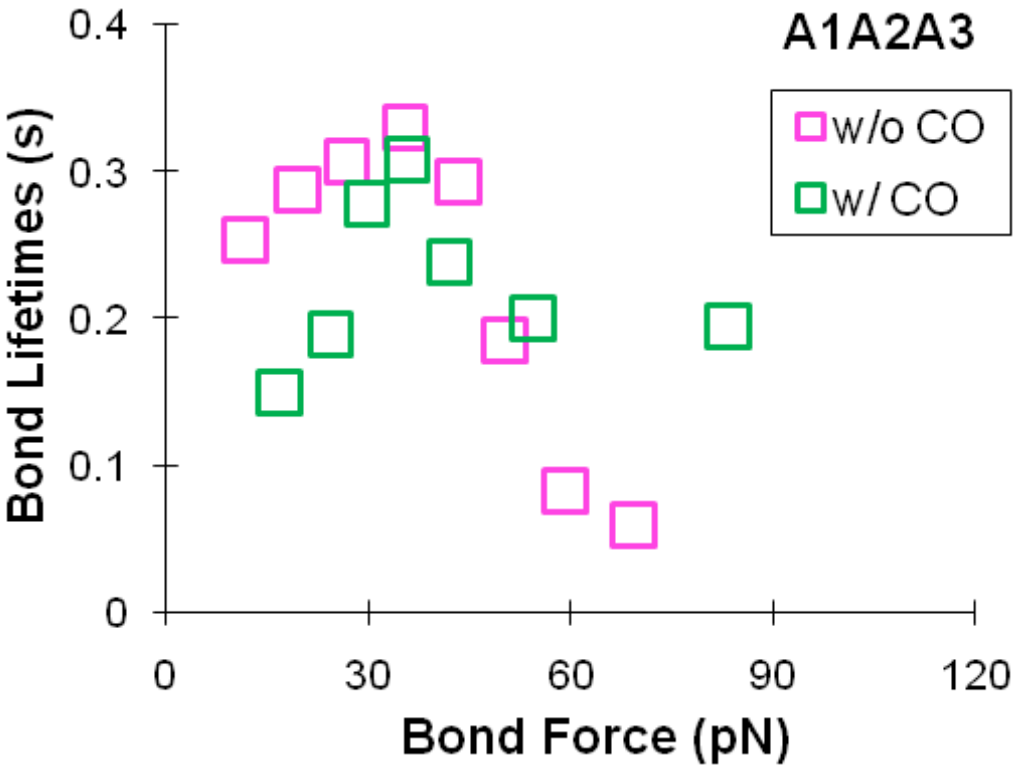

Figure 5.32: GPIbα-A1A2A3 bond lifetime vs. force curve with A1A2A3 captured by type III collagen (green square), in comparison with the data of A1A2A3 physically adsorbed on Petri dish surface (pink square).

Figure 5.20 shows the GPIbα-A1A2A3 bond lifetime vs. force curve with A1A2A3 captured by type III collagen, in comparison with the data of A1A2A3 physically adsorbed on Petri dish surface. The green squares show similarity to the A1 data at the catch bond regime, and with shorter lifetime vs. the physically adsorbed A1A2A3. When the force was larger than 60pN, collagen-captured A1A2A3 exhibited much longer lifetime (~0.2 seconds at ~90pN) than both physically adsorbed A1 and A1A2A3 (<0.05 seconds at ~90pN) when binding with GPIbα. It is also interesting to notice that bond lifetime was insensitive to even high force level when using the collagen capturing protocol, suggesting strong bond strength.

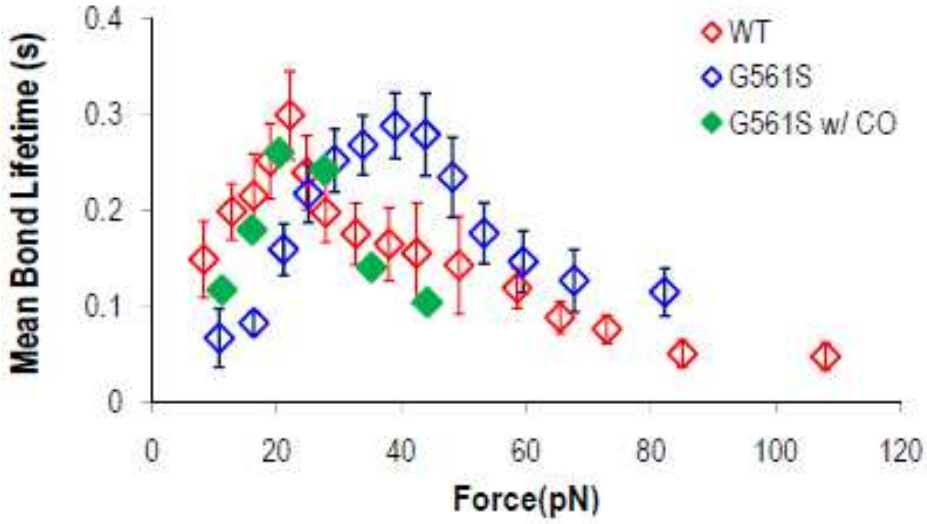

Figure 5.33: Collagen capturing effects on LOF A1 mutants G561S lifetime when interacting with GPIbα (green diamond), in comparison with physically adsorbed WT-A1 (red diamond) and G561S data (blue diamond).

To study whether collagen capturing would have effects in type 2M LOF A1 mutants, we also measured its lifetime with GPIbα (Figure 5.21). Interestingly, the shift observed for the G561S mutants was not observed for the collagen captured LOF mutants, that is, collagen capturing shifted the curve back to the WT-A1 curve.

Discussion

The above data shows a clear trend that, with the exception of the catch bond regime, collagen capturing prolonged the GPIbα-A1 lifetime. This bond lifetime enhancement was similar to A2A3's effect on A1 (Figure 5.18), but had an impact on a broader range of force. Because GPIbα can only bind to the A1 domain, the lifetime difference could only come from the conformational difference of the A1 domain. The A2 domain has been revealed to be able to form coupling with the A1 domain, in other words, A2 could bind with A1 to shield the GPIbα binding sites. From our experimental observation, the binding frequency for GPIbα-A1A2A3 was comparable to GPIbα-A1 binding. Therefore, it is highly possible that the coupling between A1A2, if there was any, has already been disrupted if this was the necessary step to expose A1's binding sites

for GPIbα. If A1 and A2 were still coupled together, the GPIbα binding sites must have already been exposed during the experiments, which might be caused by the physical adsorption. The extra linkage of two A-domain could stabilize the GPIbα-A1 binding sites thus giving longer lifetime before ~60pN. On the other hand, type III collagen capturing enhanced the GPIbα-A1 bond lifetime at larger force range, but showed minimal effects at low force range. This difference in function would come from the different structural strengthen effects at the binding sites. Therefore, A1 could assume different conformations, each of which would also cause different binding pocket structure and therefore binding strength. From the sliding-rebinding model for explaining catch bond, another possibility would be the sliding-rebinding pathway difference for the various conformation of A1 domain. The difference in the number of hydrogen bonds along the sliding-rebinding pathway would obviously be a strong factor to affect the bond strength. The combination of data for A2A3 effects and collagen effects revealed that both could affect the conformation of the A1 domain and result in the prolonged lifetime at different force range. A2A3 caused longer lifetime at lower force range, i.e. at the catch bond regime. Collagen capturing induced more evident lifetime increase at larger force range, i.e. at the slip bond regime. The A2A3 and collagen effects could be additive. One observation is that there is no difference for lifetime at catch bond regime using the collagen capturing protocol, for either A1 or A1A2A3.

It is also interesting for us to notice that collagen shifted the G561S lifetime curve back to the WT-A1 curve. This observation implies that collagen might cause the LOF A1 mutant to adopt a conformation similar to that of WT-A1. That is, the G561S A1 mutant's conformational change induced by binding to collagen might switch the molecule back to the original A1 conformation. Furthermore, it is a more dominant effect than the previous conformational change induced allosterically by point mutation. Considering the pathophysiological condition for VWF A1 binding GPIbα, LOF mutants need to bind to collagen to become immobilized on the subendothelial surface. Thus, our

current data has not observed any “loss of function” of the molecule, if collagen capturing is a prerequisite. This observation confirmed previous studies that type 2M mutant effects were only observable when the A1 molecule adopted a special conformation as in ristocetin induced platelet aggregation experiments (76).

CHAPTER 6

BINDING KINETICS OF ADAMTS13 WITH VWF

Introduction

During the process of hemostasis, the size of ULVWF affects the affinity of VWF to platelets bearing GPIbα on the membrane. ADAMTS13 (A Disintegrin and Metalloprotease with ThromboSpondin motif) is a multi-domain metalloprotease that can cleave at the Tyr1605-Met1606 bond of VWF, thus regulating the size of ULVWF. Based on the available data from previous studies, a model of proteolysis was built as in Figure 6.1 to show the regulation of ULVWF size by ADAMTS13 cleavage under blood shear flow (8).

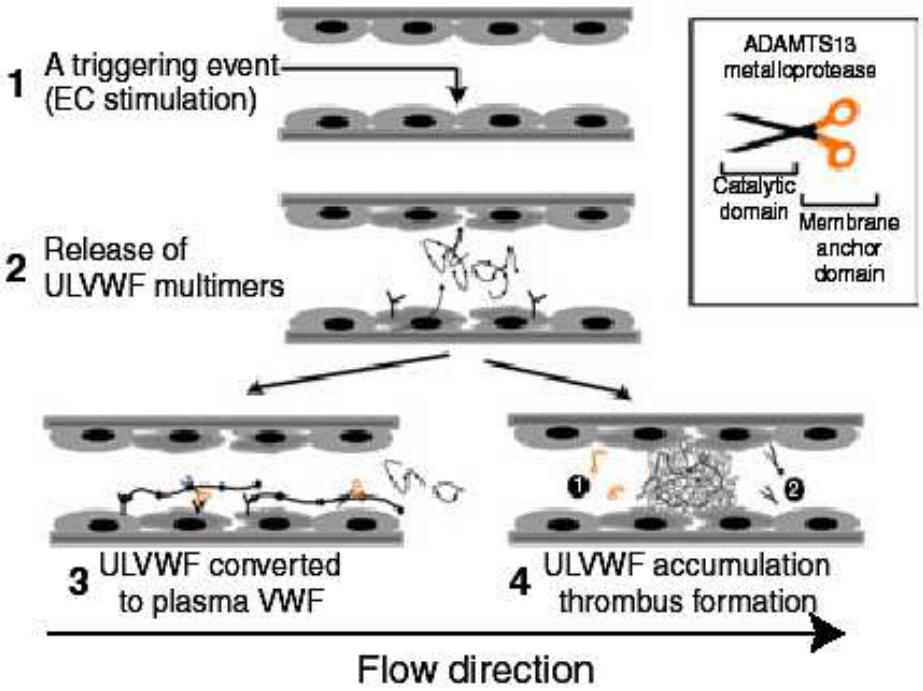

Figure 6.1: A potential model for ULVWF proteolysis by ADAMTS13 *in vivo*. (Adapted from (8))

In this model, ULVWF secreted by the endothelial cell upon stimulation would anchor at the surface of the endothelium. The subsequent binding of platelets on these hyper-adhesive VWF multimers would transduce the shear stress into stretching force on VWF molecules. The stretching force would result in the exposure of the ADAMTS13 cleavage site buried inside the A2 domain, thus facilitating the cleavage events. Smaller fragments of VWF would be released into the blood stream and would adopt a different conformation because of the concurrent release of stretching force after cleavage. This change in molecule conformation would make the released fragments resistant to cleavage because of the inaccessibility of ADAMTS13 to both/either the binding sites and/or cleavage sites in VWF. Deficiency of plasma ADAMTS13, either from inherited mutations or from an acquired autoimmune response that produces antibodies against ADAMTS13, could result in the malfunction of ADAMTS13's function of reducing the size of ULVWF molecules and could cause systematic thrombotic microangiopathies such as thrombotic thrombocytopenic purpura (TTP) (93). TTP is a serious disease with high mortality which would observe formation of platelet thrombi within the microvasculature of patients.

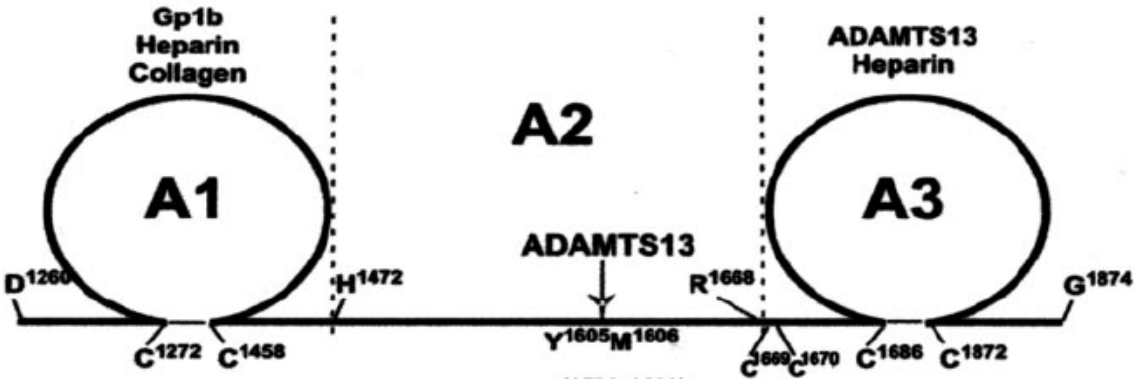

Figure 6.2: Diagram of the VWF A1A2A3 domains. ADAMTS13 cleaves at Y1605-M1606 peptide bond in A2 domain. (Adapted from (101))

VWF has a multi-domain structure which we have shown in the last chapter. The key binding sites for GPIbα are located inside the A1 domain and the ADAMTS13

cleavage site is located inside the A2 domain (Figure 6.2). The A3 domain may bind to ADAMTS13 to provide an anchoring point for the enzyme to target at the A2 domain. Since the discovery of ADAMTS13 seven years ago (102), extensive studies have been done to investigate the binding between ADAMTS13 and its substrate VWF. Most studies focused on the A1A2A3 domain because these domains are highly interdependent in regulating the exposure of the A2 domain's cleavage site and ADAMTS13's cleavage efficiency. Figure 6.3 below shows the domain structure of ADAMTS13 (103). It consists of the metalloprotease domain which is the enzymatic functional domain, disintegrin domain, TSP1-8 domains, Cys-rich domain, spacer domain, CUB 1-2 domain. Previous truncation studies of ADAMTS13 show that TSP1-8 repeats, the Cys-rich domain, the spacer domain and the CUB domains are all possible candidates to bind with the A1A2A3 domains (Figure 6.4). Therefore, the interaction of ADAMTS13 with VWF A1A2A3 is a convoluted problem, containing possible binding between different domains of both molecules.

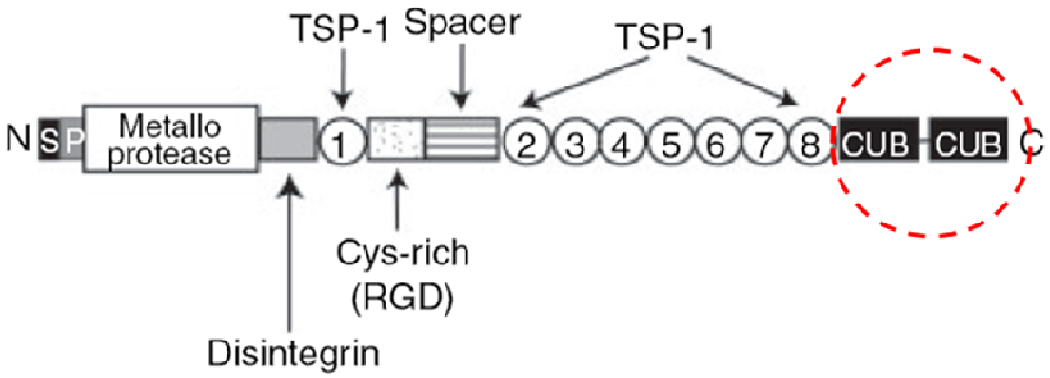

Figure 6.3: Schematic depiction of ADAMTS13 domain structure. (Adapted from (8))

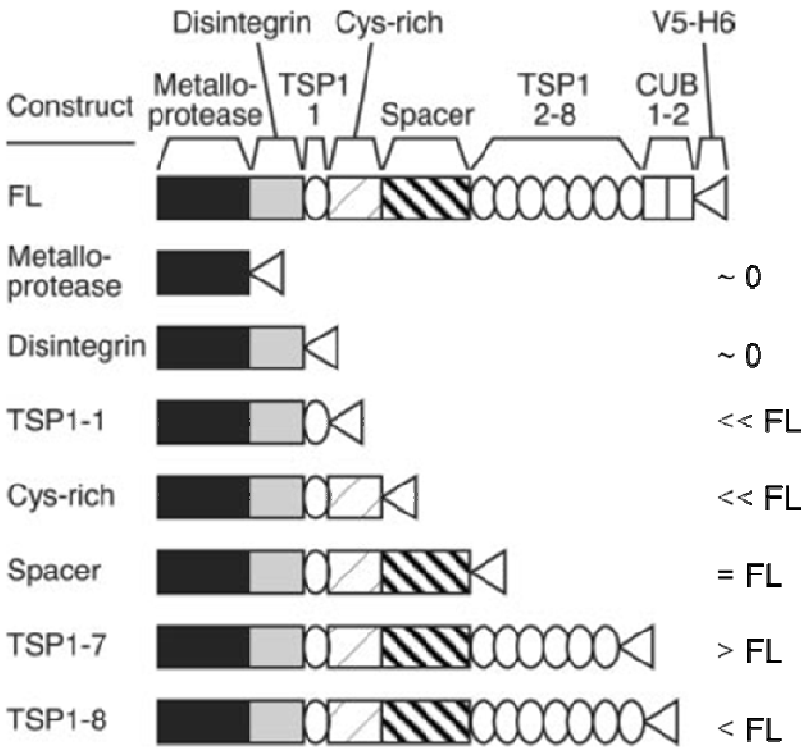

Figure 6.4: Truncation study of ADAMTS13 constructs affinity with plasma VWF. Label at right shows the comparison of each specific construct's binding affinity vs. full length (FL) ADAMTS13 molecule. (Adapted from (103))

ADAMTS13 belongs to the family of ADAMTS metalloproteinases which are frequently involved in the proteolysis of extracellular matrix proteins (103). The CUB domains are unique for ADAMTS13, which has been shown to interact with VWF (9, 104). Although the *in vitro* data revealed that the ADAMTS13 truncation construct without CUB domains retained the same binding capability with human plasma VWF (103), the *in vivo* data showed the interaction between the CUB2 domain and VWF still played a major role in regulating ADAMTS13-VWF binding after partial unfolding of VWF (adding 1M urea). The difference between these studies implied the importance of physiological shear stress in affecting the ADAMTS13-VWF interaction.

In this chapter, we study the binding kinetics of two ADAMTS13 constructs with the VWF A1A2A3 domain triplet, testing the binding force regulation of kinetics for both

interactions. These data would help elucidate the binding properties of ADAMTS13 with VWF. Our hypothesis is that full CUB domains (CUB1-2) can bind to VWF; and full-length ADAMTS13 has different force regulated binding kinetics with A1A2A3 as compared with CUB1-2 domains.

Results

CUB Domain Forms Slip Bonds with A1A2A3 Tridomain

To test our hypotheses, we started by looking at CUB1-2 binding with A1A2A3. The spots labeled on the Petri dish surface were coated with 10ug/ml A1A2A3 in PBS buffer and kept overnight at 4^{o}C. On the day of experiments, excess A1A2A3 was removed from the spot by PBS washing three times. Then the Petri dish was filled with 5ml 1% BSA in PBS solution to block the non-specific interaction. At least two AFM probes were prepared by the same protocol to physically adsorb proteins on the AFM tips. One probe would be coated by 1% BSA and the other one by 10ug/ml CUB1-2. At the beginning of the experiments, the A1A2A3 coated spots were tested by the BSA coated AFM tip at a certain distance from the surface. Once it was confirmed that the non-specific binding was low enough (<5% for three consecutive points of the same spot), we loaded the CUB tip to test the specific binding. Usually, the specific binding frequency could reach around 15%, three times the value obtained for non-specific binding.

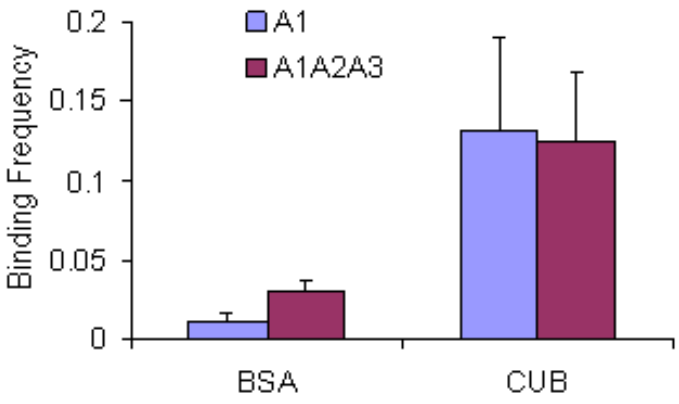

Figure 6.5: Binding frequency comparison of specific (CUB-A1A2A3) vs. non-specific (BSA-A1A2A3) interaction. Blue bars are binding with A1 domain and red bars are with A1A2A3 tridomain.

Figure 6.5 shows the typical binding frequency comparison of specific vs. non-specific. Besides testing the specific binding between CUB and A1A2A3, we also tested the possible binding between CUB and the A1 domain. The data suggested that CUB could also bind with A1. Previous studies have shown that the VWF-A1 domain could inhibit the cleavage of A2 by ADAMTS13 and that this inhibition could be relieved by interaction of the A1 domain with GPIbα(105). Binding between CUB and A1 implied that ADAMTS13 might be also able to use CUB binding to A1 to relieve the possible steric hindrance of A1 on A2, possibly through uncoupling of A1 from A2. It thus might favor the exposure of a cleavage site in the A2 domain. As revealed by other studies, the A3 domain may serve as the anchoring point for ADAMTS13 to bind A1A2A3. Although we have not done the study to test possible binding of CUB with A3 or even A2, the CUB-A1 binding may also provide an additional anchoring point for ADAMTS13. The contribution of CUB domains to the ADAMTS13-VWF binding differs for the *in vitro* and *in vivo* studies, indicating the importance of A2 unfolding. The *in vitro* binding assay without A2 unfolding might favor more interactions between ADAMTS13 and VWF, minimizing the contribution from CUB domains. With A2 unfolded and changing conformation, there might be fewer binding sites at the interface, thus maximizing the impact from CUB domains. The other possibility is that the conformational change of A1A2A3 and/or A2 from folded to unfolded condition would change the synergies for domains inside ADAMTS13, leading to the increased significance of the CUB domains' contributions to the overall binding affinity. Recent studies also showed the spacer domain binds to the exosite near the C-terminal of the A2 domain, leading to an even more complicated discussion (106).

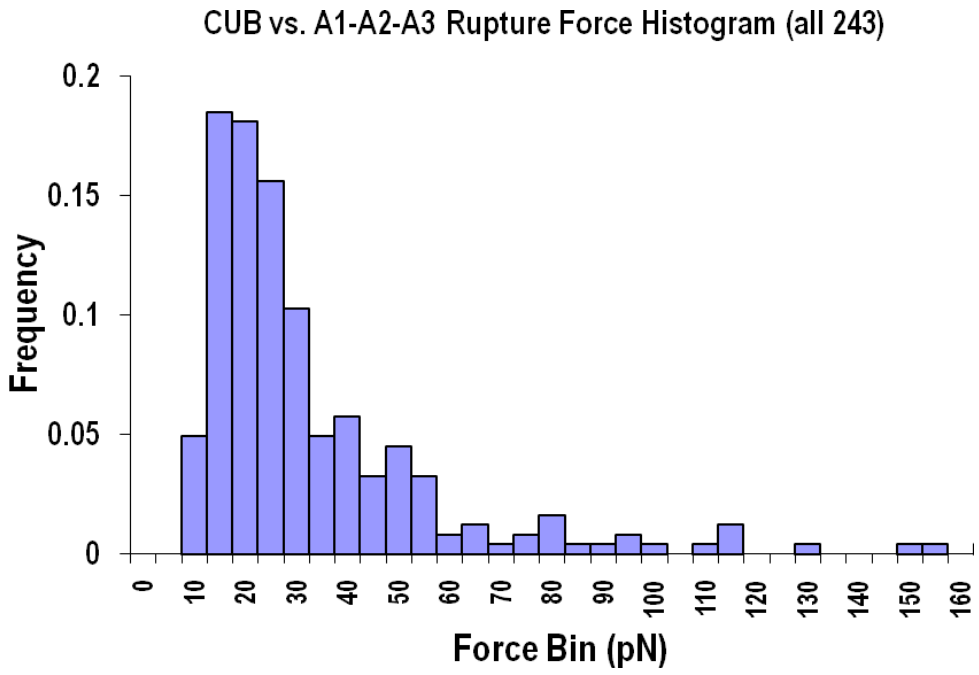

Figure 6.6: Rupture force histogram of CUB-A1A2A3 bonds at 200nm/s loading rate.

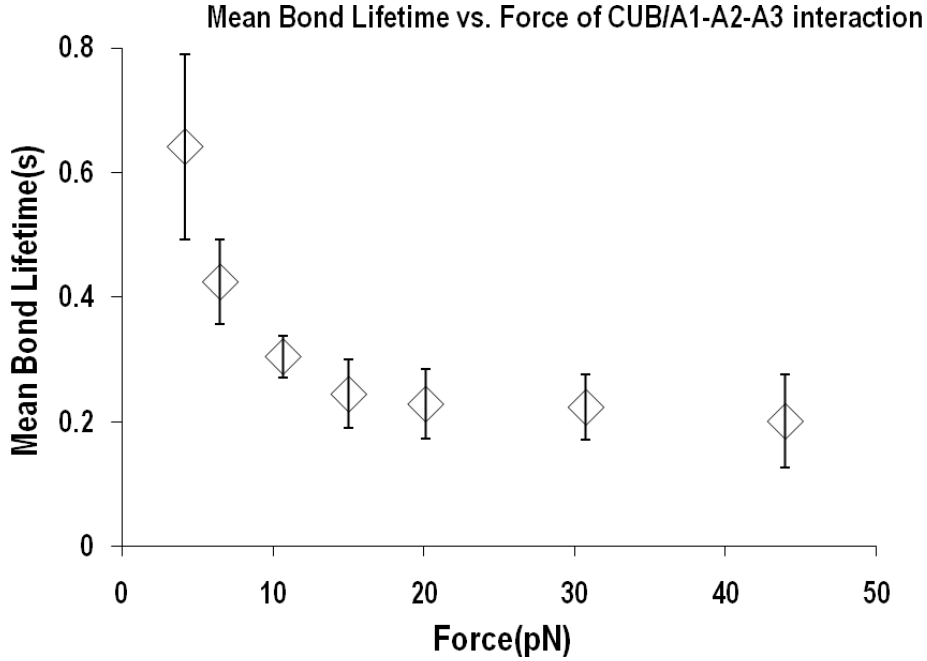

Figure 6.7: Average lifetime dependence on force data shows CUB forms slip bonds with A1A2A3.

From the binding events of CUB with A1A2A3, we first quantified the rupture forces and made the histogram to evaluate the bond strength from rupture force distribution (Figure 6.6). All the experiments were done at 200nm/s loading rates. The histogram data peaks at ~15pN, and most data had rupture force values between 10pN and 55pN. Figure 6.7 shows the average lifetime measurements for CUB/A1A2A3 interaction. It has a typical Bell model shape, indicating that a slip bond existed, i.e. increasing force shortened the lifetime.

Full Length ADAMTS13 Forms Catch Bonds with A1A2A3 Tridomain

After measuring the bond lifetime dependence on force for CUB/A1A2A3 binding, we continued to measure the full-length ADAMTS13 binding with A1A2A3. The goal was to test our hypothesis regarding whether the other domains of ADAMTS13 would affect the binding kinetics of the CUB domain. For the A1A2A3 coated petri dish, we characterized the non-specific and specific binding frequency dependence on distance. The distance here is calculated by subtracting the piezo position at the waiting/fishing stage (any point during this 500ms) from the start-to-contact point, which is the same as discussed in the last chapter. In Figure 6.8, the upper panel shows three binding frequency vs. distance curves that were used for averaging to calculate the specific binding frequency vs. distance curve shown in the lower panel. In contrast to the sharp decrease of non-specific binding (BSA-A1A2A3) frequency with increasing distance from the surface, the ADAMTS13 coated AFM tip had much slower decrease in the binding frequency when being brought away from the A1A2A3 coated surface. Based on these data, our experiments were started by testing non-specific binding frequency at >12nm distance from the surface. We would increase from 12nm until the averaged non-specific binding frequency at three consecutive testing points for the BSA coated AFM tip fell below 5%. At 2nm and 4nm, the average specific binding frequencies were even a little lower than the non-specific binding frequencies. This came from the heterogeneity

of surface physical adsorption, which could also be observed in the upper panel of Figure 6.8.

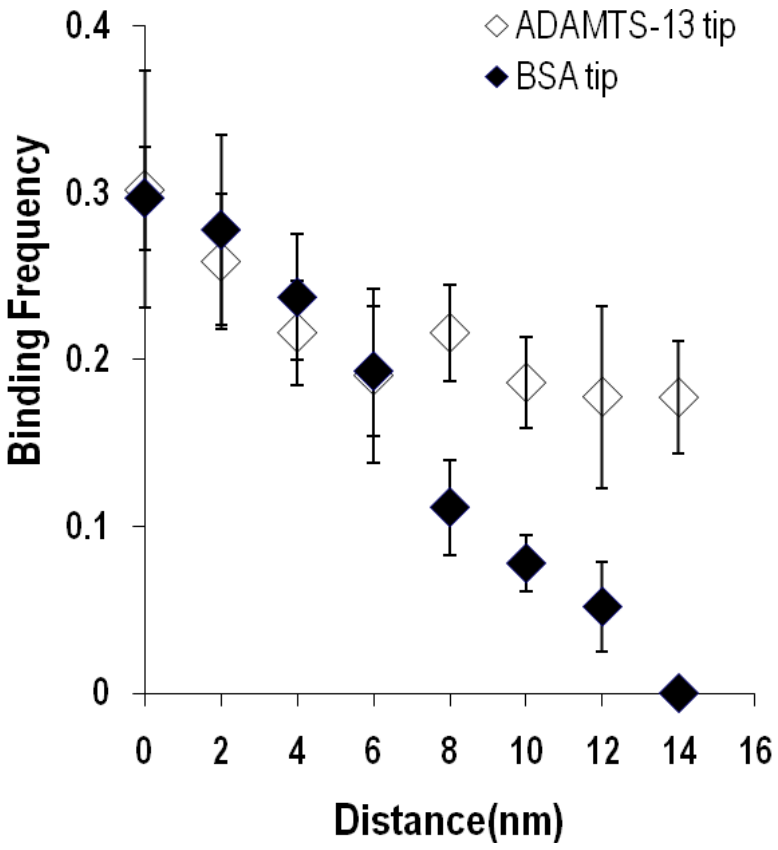

Figure 6.8: Binding frequency vs. distance curves for non-specific (BSA/A1A2A3, solid diamond) and specific (ADAMTS13/A1A2A3, diamond) interactions. Data suggest 14nm will be enough to suppress the non-specific binding, while there are still ~20% specific binding.

From observation of experiments, we found that ADAMTS13-A1A2A3 binding had certain obvious features. The most evident one was that there were many multi-force-drop events. Figure 6.9 shows an observation of typical occurrence frequency of one, two and three-force-drop events when ramping ADAMTS13-A1A2A3 bonds. The experiment was done at ~20pN clamping force, and different force drop events were counted based on the ~20% total binding frequency. This observation was consistent for all seven points tested. Compared with the frequency predicted by Poisson distribution (assuming random

occurrence of one, two, three-force-drop events), our experiments observed many multi-force-drop events, indicating the possibility of protein structural change or sequential breakage from multi-binding-sites interaction. It is highly possible that these findings represent A1A2A3 structural change, because the A2 domain could unfold even under low force levels (60). We will study the structural change of A1A2A3 in much more detail in the next chapter because we hypothesize that it is the prerequisite for ADAMTS13 cleavage.

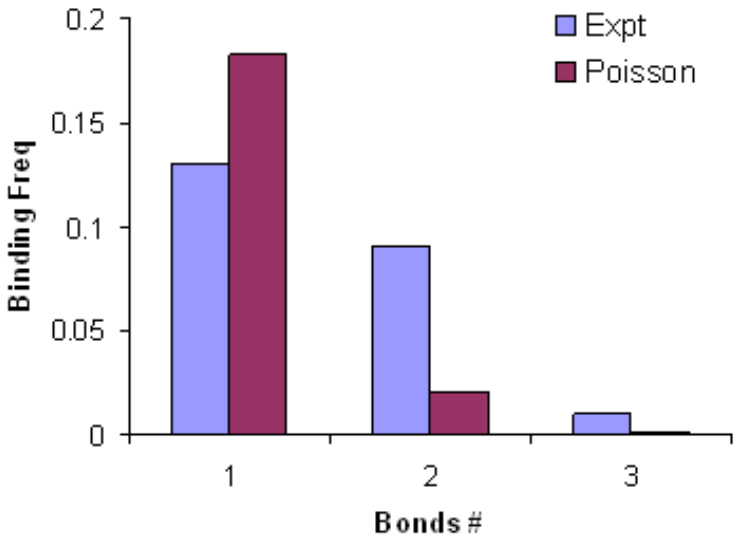

Figure 6.9: A typical distribution of one, two and three-force-drop events when stretching ADAMTS13-A1A2A3 bonds (blue bars). For the same total binding frequency ~20%, Poisson distribution predicts much lower frequency/probability for multiple bonds events (red bars), indicating there were other reasons causing multi-force-drop events.

From 401 lifetime measurements, we obtained the mean bond lifetime vs. force curve as shown in Figure 6.10. It shows a clear trend of catch-slip transition, which forms a sharp contrast to the CUB-A1A2A3 bond lifetime data. It is interesting for us to notice that, if we divide the full-length ADAMTS13 molecule into CUB and delCUB (without CUB), the delCUB part would exert a negative effect in bond strength at low force, changing the slip bond into a catch bond. At larger force level, the effect from the delCUB part would be minimal, and thus we observed the collapse of two curves.

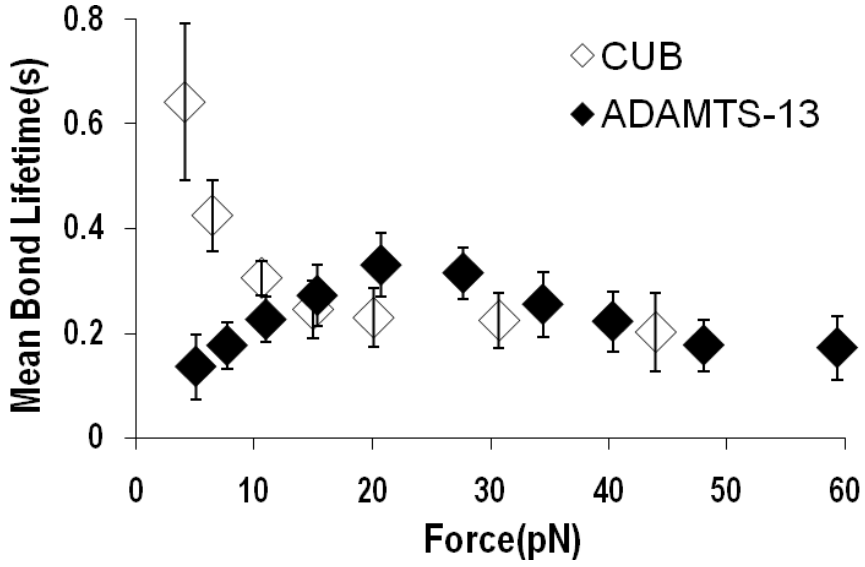

Figure 6.10: Mean bond lifetime vs. force curve for ADAMTS13-A1A2A3 interaction (solid diamond), in comparison with CUB-A1A2A3 lifetime data (diamond).

Discussion

One possible explanation for the sharp contrast at low force range could be as follows: at minimal force, delCUB would have much faster association rate (high on-rate) with A1A2A3. DelCUB thus competed and took advantage of binding to A1A2A3. However, delCUB could also have much faster dissociation tendency (high off-rate) at low force. On the other hand, the CUB domains had much less chance to bind A1A2A3 at low force because of low on-rate and/or possible hindrance by delCUB/A1A2A3 binding. Once bound, CUB would not be easily dissociated from A1A2A3 because of low off-rate at low force (slip bond). With the increasing force, delCUB's on-rate would decrease, as would its off-rate (slip bond). The decrease of the delCUB on-rate made it easier for more CUB molecules to bind A1A2A3. Although the off-rate of CUB-A1A2A3 would also decrease with increasing force, the off-rate's absolute value would still be lower than delCUB-A1A2A3 off-rate. Consequently, for the ADAMTS13-

A1A2A3 bond, we will observe a higher off-rate value (lower lifetime) than for CUB-A1A2A3, but the difference quickly diminishes with increasing bond lifetime (i.e., decreasing off-rate) as force increases. After reaching a peak value of lifetime (lowest off-rate) because of this combinational effect, the on-rate for delCUB-A1A2A3 would be negligible and most binding and dissociation events would come from CUB-A1A2A3. That may be the reason why we observed similar behavior for ADAMTS13-A1A2A3 interaction and for CUB-A1A2A3 at high force level. The above hypothesis could be tested using the delCUB construct, possibly by measuring off-rate (lifetime). If there were both delCUB and CUB in contact with A1A2A3 in the experiments, we would also use the molecular pattern from CUB-A1A2A3 data (contour length, spring constant, etc.) to map out the percentage of CUB-A1A2A3 interaction from the ADAMTS13-A1A2A3 data.

The other possible explanation for the above catch-slip transition would be to exclude the CUB-A1A2A3 interaction. The CUB's role in contributing to ADAMTS13 binding with A1A2A3 is still unclear; one possibility is that CUB was not involved in the ADAMTS13-A1A2A3 binding. This way, the catch-slip transition would be governed by the behavior of delCUB. This hypothesis is supported by the in vitro truncation constructs study in that TSP1-8 (delCUB) had negligible difference as full-length ADAMTS13 in the binding affinity with plasma VWF (103). To test this hypothesis, we can measure the lifetime of delCUB-A1A2A3 bond and see whether it behaves as the same catch-slip transition.

ADAMTS13-A1A2A3 interaction is another example of a catch bond we observed besides selectin-PSGL-1 and GPIbα-VWF interactions. Besides this, the significance of observing this catch bond may be elsewhere. This is the first catch bond to be observed for the enzyme-substrate interaction. Enzymes are responsible for virtually all of the metabolic chemistry in the biological world. And nearly all enzymes are proteins (except ribozymes – catalytic RNA). The enzyme-substrate interaction can be

divided into two steps: enzyme binding to the substrate and chemical reaction. The substrate binding is a highly specific interaction largely determined by a special binding pocket that recognizes the amino acid side chains on the substrate. In the ADAMTS13-A1A2A3 case, the binding interface may contain multiple binding sites between different domains of both ADAMTS13 and A1A2A3. Like ADAMTS13, there are many other enzymes circulating in the blood, like COX-2 and ACE, to name a few. COX-2 is involved in brain inflammation (107). The brain is dependent on highly regulated blood flow. Therefore, blood flow change during inflammation may also be important in regulating COX-2 function in the brain blood vessels. Angiotensin-converting enzyme, or ACE, plays a critical role in controlling blood pressure and is the target of common medications (108). Angiotensin is an oligopeptide in the blood that causes vasoconstriction, increased blood pressure, and release of aldosterone from the adrenal cortex. It is also under the blood shear condition that ACE converts an inactive form of angiotensin into an active form by clipping off two amino acids. Therefore, our finding of an ADAMTS13-A1A2A3 catch bond shed light on this enzyme-substrate interaction topic and implied that there could be various molecular mechanisms that these proteins can utilize to regulate the binding kinetics under different blood shear conditions.

Second, the ADAMTS13-A1A2A3 catch bond may serve as a recruiting mechanism for the ADAMTS13 to be captured to endothelial cell-anchored ULVWF from the rapidly circulating plasma. Our previous studies have shown that the L-selectin-PSGL-1 catch bond could help recruit leukocytes to the sites of inflammation. GPIbα-A1 catch bond could help recruiting platelets to the sites of blood vessel injury. Therefore, prolonging lifetime by increasing force could also help recruiting more ADAMTS13 to the sites of cleavage for ULVWF. It is still unclear how this shear force would be applied between ADAMTS13 and VWF.

Third, this catch bond could inhibit the inappropriate adhesion of ADAMTS13 with plasma VWF. For the L-selectin-PSGL-1 and GPIbα-A1 catch bonds, we found both

of them could prevent the unwanted aggregate formation of neutrophils (30) and platelets (29) in the blood stream because of the short bond lifetime under small bond force (small relative velocity in the blood). Current the ADAMTS13-A1A2A3 catch bond observations could also explain why the VWF and ADAMTS13 coexist in plasma with minimal cleavage of the former. Fast dissociation at low force may prevent substrate binding and thus may inhibit further chemical cleaving reactions. This line of reasoning might not be the only reason for preventing unintended cleavage, because VWF would also remain at folded states if the force level is low.

In conclusion, we studied the force regulated binding kinetics of VWF A1A2A3 triplet with two structural constructs of ADAMTS13, CUB and full-length ADAMTS13. They showed totally different bond behavior with varying force level, indicating the interaction between ADAMTS13 and A1A2A3 might have multiple binding sites and different binding sites may also contribute differently to the final binding kinetics. The finding of ADAMTS13-A1A2A3 catch bond shed light on the enzyme-substrate interaction although this is another example of a catch bond that exists for protein-protein interaction.

CHAPTER 7

CLEAVAGE EFFECTS OF ADAMTS13 ON VWF

Introduction

As previously demonstrated, endothelial cells constitutively release small multimer VWF molecules and secrete ULVWF upon stimulation. If ULVWF is the substrate for ADAMTS13 cleavage, the enzyme should function only during endothelial cell activation. This reasoning suggests that the thrombotic episodes of TTP are not only caused by ADAMTS13 deficiency, but also require a triggering event that induces systemic release of ULVWF.

Regarding the physiological condition for cleavage to happen, one question is begged: does ULVWF proteolysis require fluid shear stress? Shear stress has long been known as critical for platelets tethering to the subendothelial surface as the first step of the recruiting process at the site of vessel injury and of thrombus formation upon rupture of atherosclerotic plaques. The effects of shear stress on ULVWF may be positive or negative in that it can enhance the binding of ULVWF to platelets or it can facilitate the proteolysis of ULVWF by stretching the molecule to an open conformation. Supporting evidence for this hypothesis includes the following: First, denaturing agents such as urea are required for VWF cleavage by ADAMTS13 under static condition (109, 110), while the cleavage under shear stress occurs without such requirement (9, 111). Second, ULVWF strings could be cleaved a thousand fold faster under shear stress than under static condition (9). Third, electronic microscopy observation revealed that an arterial shear stress of 35 dyn/cm^2 converts loosely coiled VWF multimer with ~0.3 μm diameter to an extended filament about 1-3 μm long (65, 92). This conformational change of the molecule may expose the cleavage site of a single peptide bond buried inside the A2

domain and shielded by A1 and A3 domains. This possibility is supported by previous studies showing that the recombinant A2 domain polypeptide could be cleaved faster and does not require urea, while cleavage of the recombinant A1A2A3 polypeptide is significantly slower (112, 113). Removal of the A1 domain also increases cleavage rate of VWF more than 10 fold (105). Further, the more opened-up conformation by shear stress may also facilitate the binding of ADAMTS13 to initiate the cleavage. Enhanced cleavage with similar efficiency has been observed for both plasma VWF under arterial shear stress of 34-48 dyn/cm^2 (114) and ULVWF string at arterial (40 dyn/cm^2) and venous shear stresses (2.5 dyn/cm^2) (9). Therefore, using the single molecule method to study ADAMTS13 cleavage efficiency will provide important insights and direct experimental evidence to reveal how mechanical force plays an important role in regulating VWF cleavage by ADAMTS13.

In this chapter, all the experiments are designed and finished by the author. I would like to thank Jiangguo Lin for his help with the data analysis. Without his help, it would take much longer time to finish the project.

Results

Experiment Setup and Specificity Control

Using the Atomic Force Microsope (AFM), we measured the interaction of GPIbα or CR1 (mAb targeted at A1 domain) with VWF A1A2A3. The experimental setup is shown in Figure 7.1.

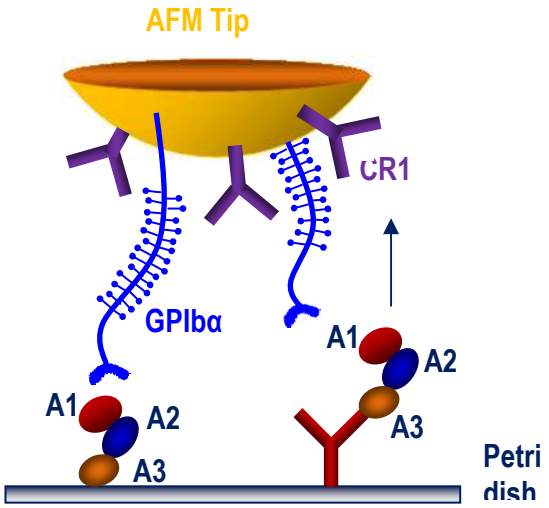

Figure 7.1: Experimental set-up for mechanically stretching VWF A1A2A3 by GPIbα (labeled blue) or CR1 (labeled purple). GPIbα or CR1 was physically adsorbed on AFM tip; A1A2A3 was either physically adsorbed on Petri dish, or captured by anti-6-HIS mAb pre-adsorbed on Petri dish.

We used two experimental protocols to immobilize and stretch A1A2A3. In the first protocol, 10ug/ml A1A2A3 in PBS solution was physically adsorbed on a Petri dish surface and kept at 4^{o}C overnight. On the day of experiment, excess A1A2A3 solution was washed three times by PBS buffer, and the Petri dish was filled by 5ml 1% BSA to block the non-specific binding. When running cleavage experiments with ADAMTS13 in the buffer, 200ul PBS buffer with 1% BSA and 5ug/ml ADAMTS13 was added to the spots with A1A2A3. A meniscus would form between the tip mount and Petri dish and the liquid inside the meniscus usually could last at least 3 hours for experiments before the liquid evaporated to an insufficient level. EDTA could totally inhibit the function of

ADAMTS-13 and was also added in the buffer to serve as a control to see whether it could kill the cleavage effects. On the other side, GPIbα was also physically adsorbed on the AFM tip surface. The AFM cantilever (Veeco Instruments, Santa Barbara) was soaked in 10ug/ml GPIbα in PBS solution, incubated at 4^{o}C overnight. The AFM tip was rinsed and soaked in 1% BSA for at least 30 min before the experiments. The A1A2A3 coated spots on the Petri dish were tested using a 1% BSA coated AFM tip first to confirm that the non-specific binding was low enough before continuing with specific binding experiments.

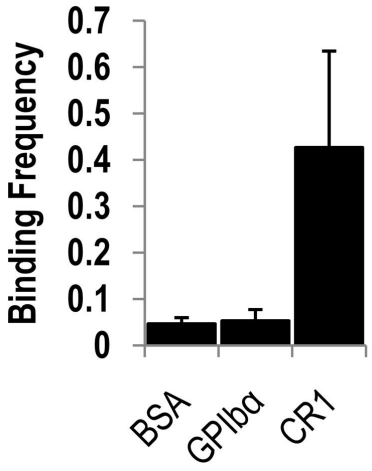

Figure 7.2: Anti-6-HIS mAb capturing A1A2A3 binds with CR1 but not with GPIbα.

In the second protocol, we physically adsorbed anti-6-His mAb on a Petri dish surface by coating the labeled spots with 10-15ug/ml anti-6-HIS mAb in PBS solution under 4^{o}C overnight. Excess solution was washed off the spots the next day and 20ul 5-10ug/ml A1A2A3 was dropped on the spots for capturing. This secondary incubation was 1 hour under room temperature, and wet tissue was covered on the Petri dish to keep the A1A2A3 solution from evaporating. Then excess A1A2A3 would be washed away and 5ml of 1% BSA filled in the Petri dish to block the non-specific binding. 10ug/ml CR1 in PBS solution was used to soak the AFM cantilever as described above. A 1% BSA in PBS coated AFM tip was used to test the non-specificity of the A1A2A3 spots, and the

CR1-coated cantilever was used to stretch the A1A2A3. Different immobilization methods lead to different conformations of A1A2A3, and consequently affected their binding properties. GPIbα could bind with physically adsorbed A1A2A3 but not with antibody-captured A1A2A3. In sharp contrast, conformational sensitive antibody CR1 could bind with anti-6-HIS captured A1A2A3, indicating the conformational differences for differently immobilized A1A2A3 (Figure 7.2). Mostly likely, physical adsorption "activated" A1 and exposed its GPIb binding sites, making it ready to bind GPIbα. Antibody capturing kept the A1 domain in the "inactive" state and it could only bind with CR1. The other possibility is that the physical adsorption disrupted the coupling between the A1 domain and the A2 domain, thus exposing the GPIb binding sites.

Force Clamp Experiments Detect Molecular Conformational Change

With the above experimental set-up, we used a single molecular experiment to study the cleavage effects of ADAMTS13. **We hypothesize that the mechanical stretch of VWF induces molecule conformational change and thus facilitates its proteolysis by ADAMTS13**. Although this hypothesis has received some support (9) (92) (60, 114), these studies are thermodynamic measurements of protein unfolding by chemical denaturing reagents under equilibrium conditions. More direct and definitive evidence is required to validate or falsify the hypothesis.

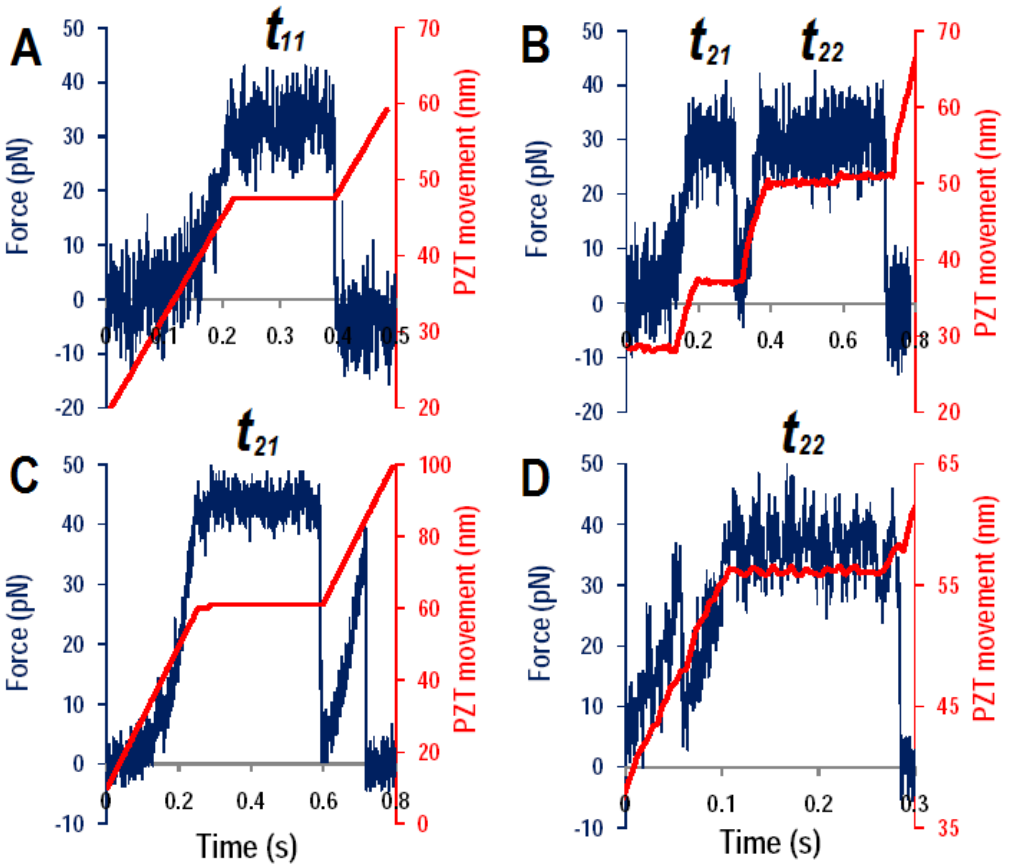

Figure 7.3: Force (navy) and piezo movement (red) vs. time data recorded by AFM. Panel A **shows 1-force-drop lifetime t_{11} (time-to-rupture);** B **shows 2-force-drop having lifetimes t_{21} (time-to-unfold) and t_{22} (time-to-rupture);** C **shows 2-force-drop having only lifetime t_{21} (time-to-unfold);** D **shows 2-force-drop having only lifetime t_{22} (time-to-rupture).**

Figure 7.3 shows the force clamp experiments we used to detect molecular conformational change and enzymatic cleavage effects. Panel A represents the single-force-drop (rupture) event which has been used extensively in our previous measurements of bond lifetimes. The curve in navy color is a force trace of cantilever deflection over time, converted from the A-B voltage signal. The force clamp routine will be triggered once the pre-set force has been reached. The piezo voltage signal over time is also recorded as a red curve. The trigger point of the force clamp routine is the same point for starting lifetime recording and also the same point for the piezo to stop retracting. Once there is structural change or bond rupture, the force on the cantilever will decrease and the piezo will continue to retract until the final bond ruptures.

Panel B recorded two lifetimes; we defined the first one as time-to-unfold and the second one as time-to-rupture. The second force drop could only be a bond rupture event; otherwise there would be a third ascending phase until final rupture. The first force drop could be unfolding or uncoupling, either of which is a catastrophic structural change of A1A2A3. And the time-to-unfold is the time recorded showing how long the structure can hold there before catastrophic structure change happens. In other words, it is the waiting time before unfolding/uncoupling. Panel C has time-to-unfold but no time-to-rupture because the second ascending phase could not reach the preset force (~45pN) before the bond finally ruptured. Panel D does not have time-to-unfold and only has time-to-rupture. Unlike panel A, panel B, C, and D all have two ascending phases, undergoing structural change before the final bond rupture.

We first questioned whether these two-ascending phase observations were the results of two-bond rupture events. The following analysis has been done to rule out the multi-bond break possibility.

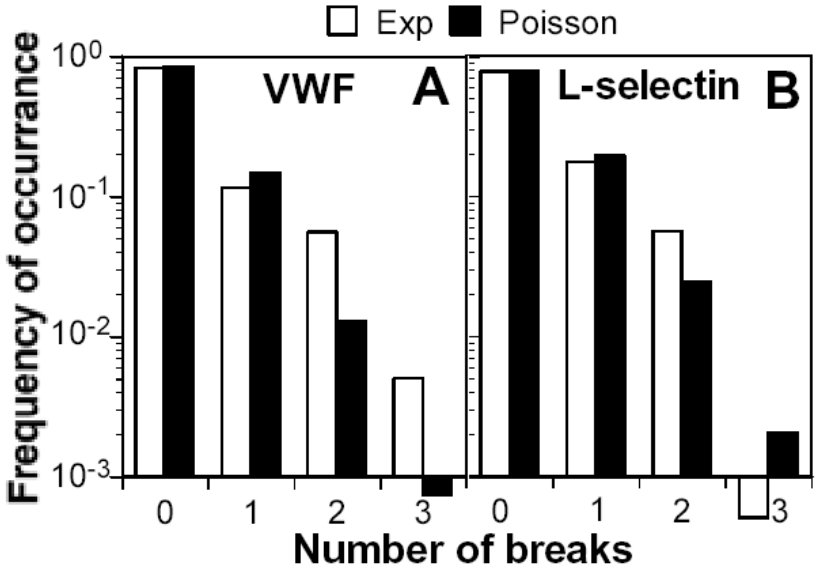

Figure 7.4: Frequencies of occurrence of multiple force drops (number of breaks) in the raw force scan of stretching GPIbα-A1A2A3 bonds (Figure 7.3 only shows events with up to two force drops) compared with Poisson distribution prediction (Panel A). Panel B shows the comparison from experiments of L-selectin/PSGL-1 interaction.

First, we counted the number of multiple force drop events and compared the ratio of these events to the multi-bond break observations of other molecule systems and to that predicted by Poisson distribution. We analyzed the frequencies of occurrence of 0 (no adhesion), 1 (Figure 7.3 panel A), 2 (Figure 7.3 panel B, C and D), and 3 (not shown) force drops in an ensemble of force-scan traces collected under identical conditions, and we compared the results to the Poisson distribution (Figure 7.4A). Poisson distribution is expected if multiple force drops represent multiple bonds (115, 116). When the total binding frequency (thus probability of no adhesion, or zero break) is matched, the numbers of 1, 2 and 3 breaks measured from the selectin experiment agree with the Poisson distribution (Figure 7.4B), suggesting that the sequential force drops represent sequential dissociation of multiple bonds in parallel (13). In contrast, we observed more 2 and 3 force drop events in the VWF data (at the expenses of fewer single break events) than were predicted by Poisson distribution (Figure 7.4B, note the log scale used in the

ordinate). This is consistent with the interpretation that the sequential force drops represented sequential unfolding of multiple globular protein domains in series. Or, A1 domain uncoupling from A2 domain could also contribute to these sequential force drops.

Force-Extension Curves Exhibit Clear Patterns for A1A2A3 Conformational Change

From the force-clamp data shown in Figure 7.3, we can convert the force trace over time into force vs. molecular extension curves based on force and piezo voltage signals, which are more straightforward tools for examining molecular signature or structural change patterns. The molecular extension value is calculated by subtracting cantilever deflection from the piezo movement. Force-extension curves are fitted by Worm-Like-Chain model (WLC):

$$f(z) = (k_B T / L_p)\{z / L_c + 0.25[(1 - z / L_c)^{-2} - 1]\}$$

From the WLC model fitting, we can get fitting parameters including the Contour Length Increment. Figure 7.5 shows the alignments of 32 force-extension curves with the contour length increment ranging from <5nm to 80nm. In the upper panel, all the curves are aligned by the first ascending phase (black dots), leaving the second ascending phase spanning all around the space (color dots). In the lower panel, we separated the curves into three color schemes (blue, navy and green) based on the contour length increment histogram shown in Figure 7.8, which represented different contour length increment groups: 15-20nm, 45-50nm and 0-80nm. All the curves are still aligned by the first ascending phase. The purpose is to visualize the patterns from all these two force drop events.

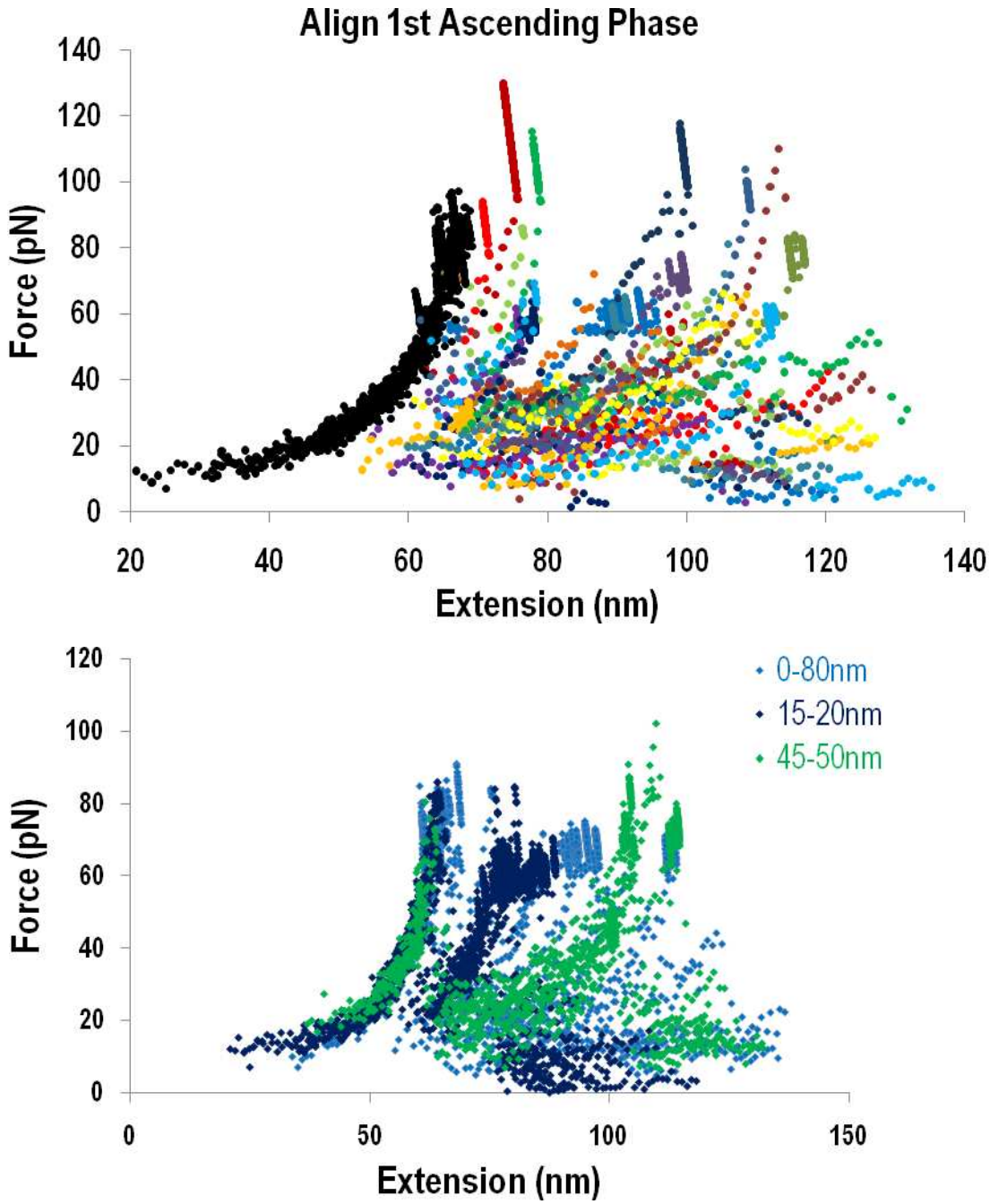

Figure 7.5: Upper panel shows alignment of 32 force-extension curves for GPIb stretching A1A2A3. Two sample curves were taken to represent each 5nm contour length increment bin, and totally there are 16 bins in the range of 0-80nm. The first ascending phase (shown in black) was aligned and other parts of the curve not aligned (shown in color). Lower panel aligns 47 force-extension curves. Curves were separated into three color schemes: blue, navy and green, which represented different contour length increment groups: 15-20nm (navy), 45-50nm (green) and 0-80nm (blue). This separation was based on the contour length increment histogram shown in Figure 7.8.

In Figure 7.5, the good alignment of the first ascending phase rules out the possibility of considerable conformational difference in A1A2A3 molecules because of the physical adsorption protocol. Because the AFM has spatial resolution of 1nm, A1A2A3 may still have small conformational variations in the sub-nanometer scale, beyond the resolution of our current experimental system. This similarity provided a uniform pool of A1A2A3 molecules for the pulling experiments. The aligned dots in the Y-axis direction result from thermal fluctuation of the A-B signal during lifetime recording. The piezo had stopped retraction but the cantilever was still vibrating, causing the A-B signal's fluctuation. The calculated stretching force would also vibrate because of this.

In the lower panel of Figure 7.5, although the WLC model gives similar contour length increments in each specific group, chances are that they still could be misaligned if obvious patterns did not exist. The curve shape was not solely determined by contour length increments. The second ascending phase of these curves formed two clusters, one at 15-20nm and the other one at 45-50nm; this is consistent with the following contour length increment histogram analysis. This clustering suggested there are molecular signatures underlying all these two force drop events. The first cluster was packed denser than the second cluster, which could be due to the properties of structural change.

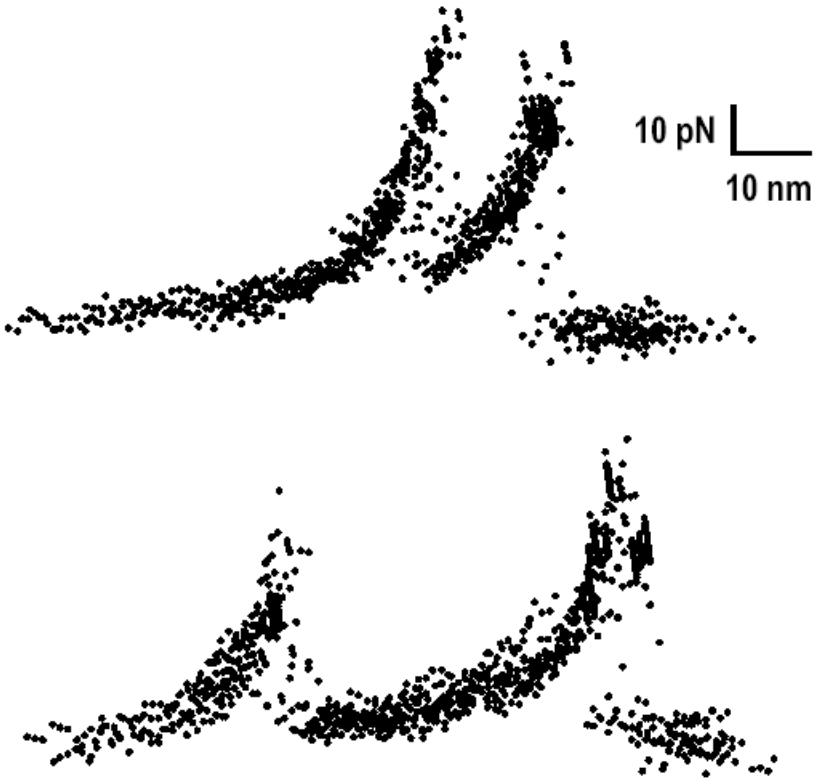

Figure 7.6: Two ascending phase alignment of force-extension curves with contour length increments falls in between 15-20nm and 45-50nm. This method aligns both first and second ascending phases, which shows more clearly two patterns.

We tried another aligning method. Aligning first ascending phase and second ascending phase, 15-20nm and 45-50nm contour length increment force-extension curves gave even clearer pattern as shown in Figure 7.6. This aligning method is implemented by the naked eyes and is more like a least-square-fitting method, trying to minimize the differences between different curves. Although the alignment of these force-extension curves was still qualitative, it provided us some insight into the different molecular behaviors observed from these two force drop events. Most importantly, from these insights based on experimental observation, we could form the proper molecular model and further test our hypothesis from the analysis of current data.

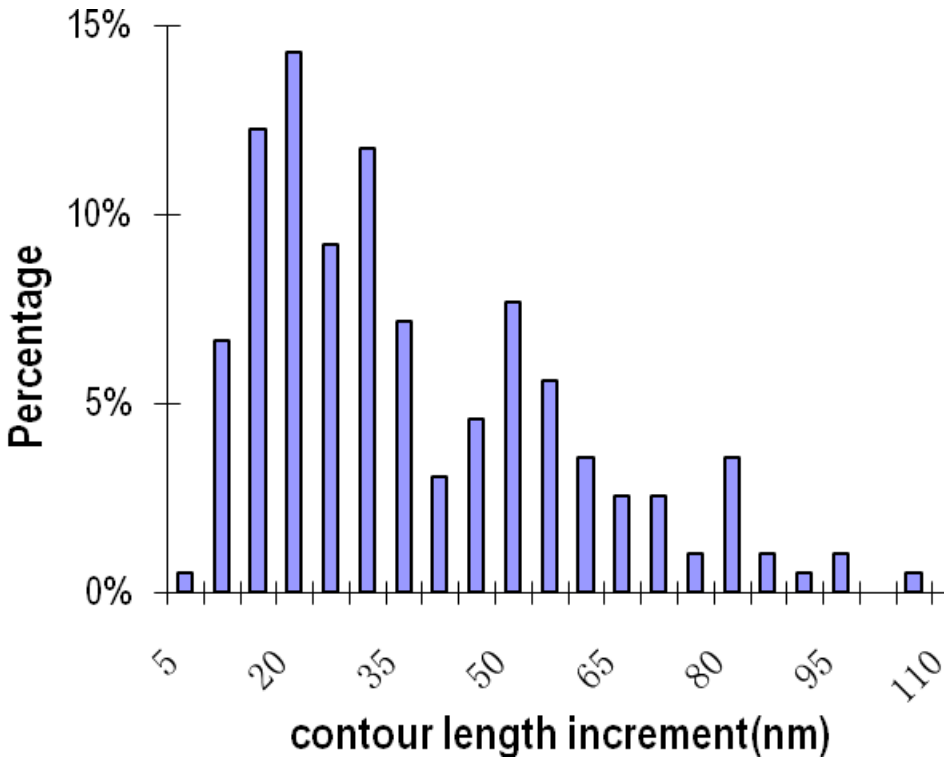

Figure 7.7: Contour length increment histogram of GPIbα-stretching force-extension curves. Contour length increment value is from Worm-Like-Chain (WLC) model fitting of force-extension curves. Histogram peaks at 15-20nm and 45-50nm.

The above description has also been observed and confirmed from the contour length increment histogram analysis for GPIbα force-extension data. Figure 7.7 shows there are two major populations in the histogram. The highest peaks of these two populations are 15-20 nm and 45-50 nm, suggesting that most occurrences happen at that contour length increment.

Furthermore, when steered molecular dynamics (SMD) simulations are used to unfold a model VWF-A2 structure, the results are consistent with thermodynamic and structural analyses, showing that among the three homologous A-type domains, A2 is the easiest to unfold because the N- can C-termini of both A1 and A3 are linked by a disulfide bond whereas A2 is not. The β-strands were observed to unfold sequentially, giving rise to multi-peak force vs. N-to-C terminal length plot (Figure 7.7).

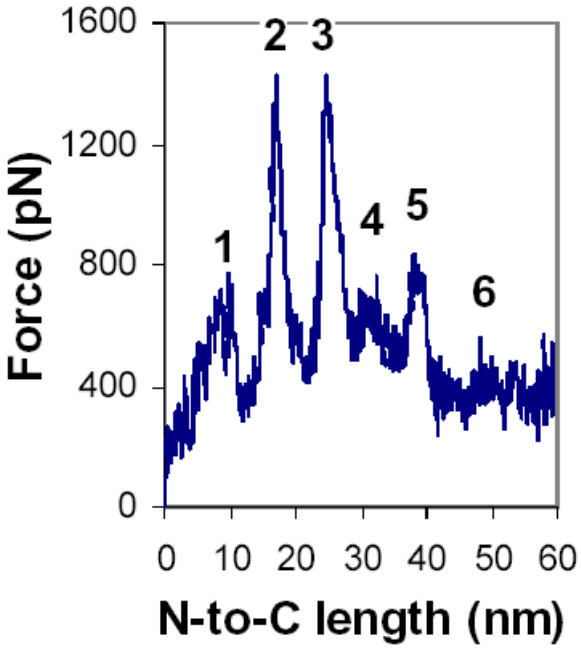

Figure 7.8: Force vs. N-to-C length plot of unfolding VWF-A2 domain by SMD simulation (by Wei Chen)

The force level is much higher in the simulation than in the lab experiments because SMD must use much larger forces to accelerate the sub-second processes to nanosecond processes that are observable in computer simulations. Nevertheless, the simulated molecular length changes should provide some insights. The length of 20nm after the second force drop agrees well with the first peak value of the contour length increments value. This provides strong evidence for us to build a molecular model of the catastrophic structural change.

Next, we measured the spring constant of the two ascending phases to further verify that these two force drop events are different from two bond rupture events that were observed before for L-selectin/PSGL-1 double bonds sequential rupture events (Figure 7.9).

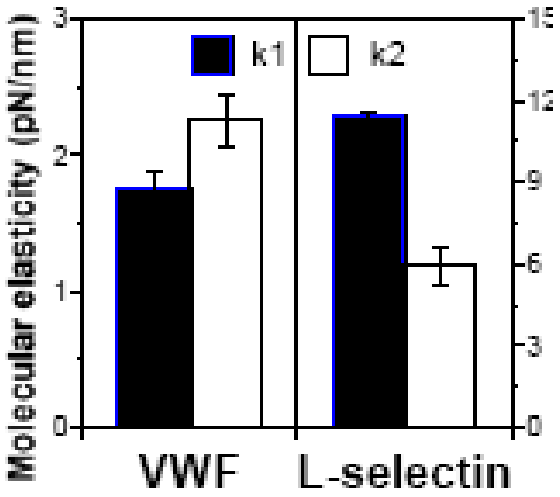

Figure 7.9: VWF A1A2A3 structural change in two-force-drop events exhibit comparable spring constants for the two ascending phases which is different from typical double bonds sequential break as in L-selectin/PSGL-1 case. The second ascending phase has only half the elasticity of the first ascending phase for the double bonds.

The sequential breakage of L-selectin/PSGL-1 double bonds resulted in half the value of spring constant for the second ascending phase as for the first ascending phase (Figure 7.9 right panel). In sharp contrast, for the roughly 200 measurements of these GPIbα-stretch force-extension curves with different contour length increments from 5nm to over 100nm, the second ascending phase has a similar or even larger spring constant value than the first ascending phase (Figure 7.9 left panel). Thus, it is more likely that structural change took place than that two bonds ruptured in sequence.

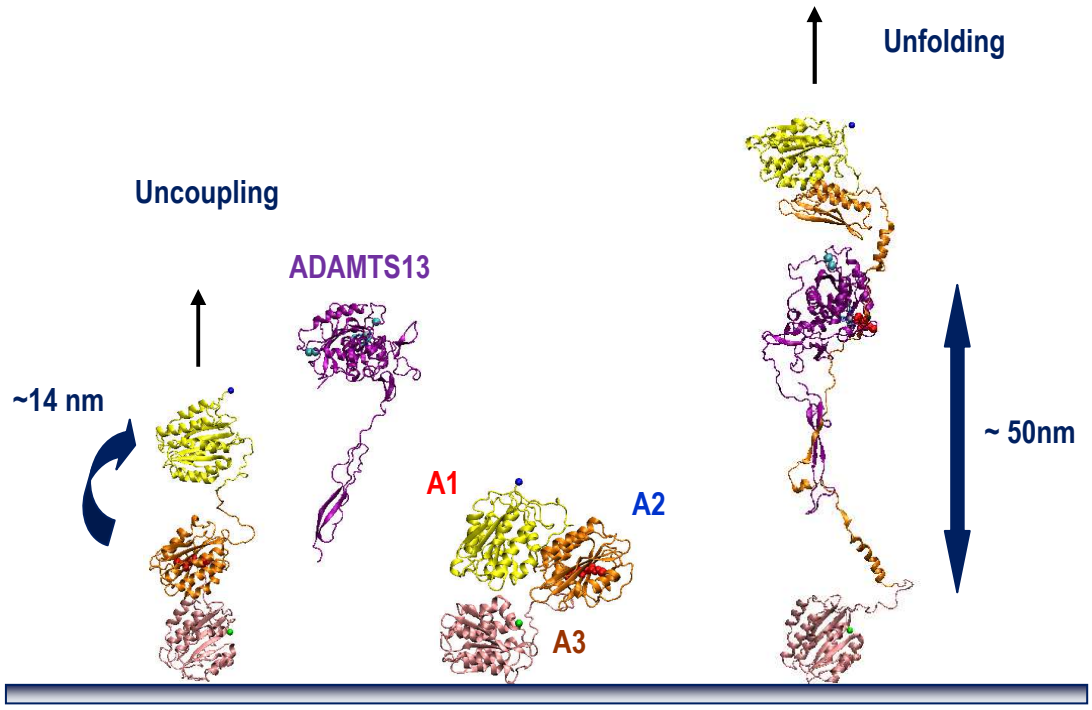

Figure 7.10: Model for A1A2A3 catastrophic structural change from un-stretched state (middle): one pathway as uncoupling of A1 from A2 domain (left); another pathway as unfolding of A2 domain with A1A2 coupled (right). (by Wei Chen)

Figure 7.10 shows a model illustrating how tensile force on A1A2A3 (applied by GPIbα or CR1 binding to A1) could induce uncoupling of the A1A2 or unfolding of the A2 domains before the final breakage of the receptor (GPIbα or CR1) ligand (A1A2A3) pair. The final breakage could be rupture of the bond or cleavage in the A2 domain when ADAMTS13 was present in the buffer. The above-mentioned catastrophic structural change and final rupture is a series of events that have been observed in the AFM force clamp experiments as shown in Figure 7.3. To study these catastrophic structural change events, we started by analyzing two force drop events because this is the basic building block for three-, four- or even more ascending phase events. Most importantly, analysis of two-force-drop events excludes those multiple force drop events that combine different kinds of structural change. The complexity of discerning specific structural change has been minimized, because the first force drop could only reflect uncoupling or unfolding

events. It is most unlikely that uncoupling and unfolding would happen simultaneously. If both of these structural changes happen, there would be at least three force drops before final bond rupture.

Discussion

Naturally, A1A2A3 are packed with each other in the globular state, with the ADAMTS13 cleavage site shielded inside the A2 domain (Figure 7.10 center). Only until sheared by flood flow or surrounded by denaturing reagents like urea, will this cleavage site be exposed to ADAMTS13 (8, 9). The detailed molecular mechanism by which the A2 domain unfolds, binds to ADAMTS13 and is cleaved remains unclear. The A1 domain would couple with the A2 domain (117), and the uncoupling of A1 from A2 could result in a molecular extension around 15-20nm (Figure 7.10 left). The other possibility is that A1 still couples with A2 and that pulling A1 will induce A2 to unfold because of the force propagated from the coupling interface. From the SMD simulation we know that the A2 domain unfolding could undergo several steps, depending upon the pulling force and the loading speed. Different unfolding steps will generate different molecular extensions. Therefore, the contour length increment histogram would be the overlap of two extension histograms representing two possible structural changes, namely, uncoupling and unfolding extension. The first peak of the contour length increment histogram would also be the summation of these two kinds of conformational change, rather than solely the uncoupling pathway's signature.

Analyzing ADAMTS13 Effects on GPIbα Binding to A1A2A3 Tridomain

I: ADAMTS13 Effects on Binding Frequency

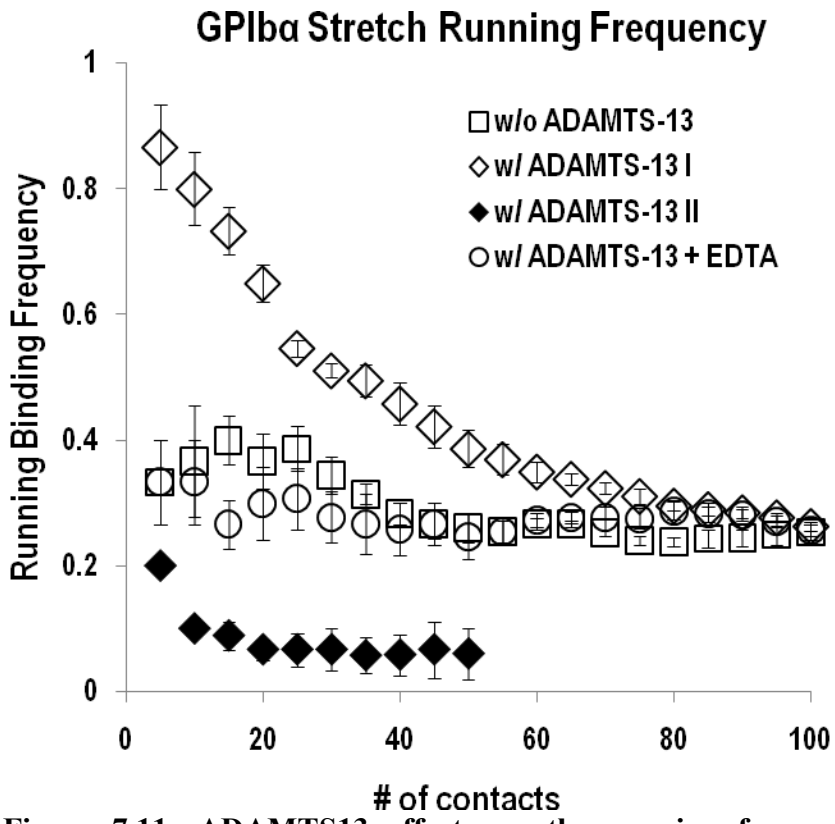

Figure 7.11: ADAMTS13 effects on the running frequency of GPIbα binding A1A2A3 in the absence (square), presence (diamond) of ADAMTS13 and EDTA (circle). The above three curves all have 26% total binding frequency in 100 contacts. The bottom curve (solid diamond) has an initial binding frequency of 20%. Each curve is based on average of three individual curves. Error bars are standard error of the mean.

To dissect the ADAMTS13 cleavage effect, we started by analyzing the binding frequency because this is one of the first read-outs from the experiments. Experiments with similar final binding frequencies (out of 100 contacts) of around 26% were taken in the comparison. For each curve in Figure 7.11, we averaged three running frequency curves. From the data we can see that, before adding ADAMTS13, the binding frequency gradually decreases from 40% to 26% (square). This decrease could be due to the gradual

depletion of molecules adsorbed on either surface of the AFM tip or the Petri dish. This observation of gradual decrease in binding frequency was consistent with our previous observations in using AFM to study L-selectin binding with 2-GSP-6 and 6-sulfo-sLex, and GPIbα binding with VWF A1. Although the strength of physical adsorption is very strong compared with receptor-ligand interaction, chances are that some molecules will be detached from the surface or gradually lose functionality. This depletion of function is not obvious when the coating density is high. Compared with the condition in the absence of ADAMTS13, the running frequency of binding decreased sharply from ~80% to ~40% in less than 50 touches for the condition in the presence of ADAMTS13 (diamond). After 70 touches, the running frequency was similar to the control level. Adding EDTA in the buffer inhibits the function of ADAMTS13. The initial binding frequency of 35% can last 100 contacts, gradually decreasing to the final binding frequency of 26% (circle). Because we are comparing three curves with similar final binding frequency (~25%), the initial binding frequency could be very different, which is shown in Figure 7.11. In other words, only those experiments with initial binding frequency as high as 80% could survive the sharp drop and reach the final 26% binding frequency. This sharp drop in binding frequency indicates that the cleavage effects were very obvious in our experimental observations. If the initial binding frequency is ~80%, the condition with the absence of ADAMTS13 will have much higher final binding frequency compared with the condition in the presence of ADAMTS13 (data not shown). Furthermore, for the case in the presence of ADAMTS13, if the initial binding frequency is ~20% (solid diamond), it would also decrease sharply to the background level binding of 5% in just 20 contacts.

There could be several reasons for the sharp drop in binding frequency. The direct explanation is that the physically adsorbed A1A2A3 lost functionality to bind GPIbα on the AFM tip. When the GPIbα coated AFM tip picked up A1A2A3 by binding to the A1 domain, the A2 domain was also stretched, regardless of whether A1 was coupled to A2

at that time. If the A2 domain unfolded and was cut by ADAMTS13, the A1 domain would also detach from the rest of the A2 domain. Part of the A2 domain with the whole A1 domain (labeled as A1A2*) would detach from the petri dish surface. With the ongoing experiment, more and more A1A2* would be chopped off their anchoring points. Most likely, the anchoring point would be the A3 domain. It could also be the A2 domain itself, if the A2 domain is adsorbed to the Petri dish by certain chance. If the anchoring points lay on the A1 domain surface, the ADAMTS13 would not have any chance to cut the A2 domain before the A1 domain was peeled off the surface. This is most unlikely because we observed many multiple force drop events and binding frequency dropped obviously after these multiple force drop events. The above speculation is based on the assumption that the A2 domain has to unfold upon stretching before it can be accessed and cut by ADAMTS13.

After cleavage, the A1A2* could still bind to GPIbα if the final force drop was a result of cleavage. This type of binding could last much longer than the binding obtained under the forced condition. Or it could also be short, if low force shortened the lifetime of the bond between GPIbα and A1A2* when there is a catch bond behavior. The GPIbα binding site for A1 could be blocked by A1A2* if this cleavage product still remained on dock. The analogy is that the bait is still being occupied by a half fish, so other fish cannot bite. Thus, the binding frequency will drop when more and more A1 binding sites on GPIbα are occupied by A1A2* with the progression of cleavage. Compared with the first reason for A1A2A3 depletion, this effect is not as obvious, although it could also contribute to the binding frequency drop when doing experiments at a specific point. If we changed the point on the Petri dish for the experiment, the initial binding frequencies were comparable. This provides strong evidence that it is the A1A2A3 coated points that were losing functionality. Only after several hours of experimentation (after changing ten points) would we find that the AFM tip also lost functionality.

II. ADAMTS13 Effects on Contour Length Increment

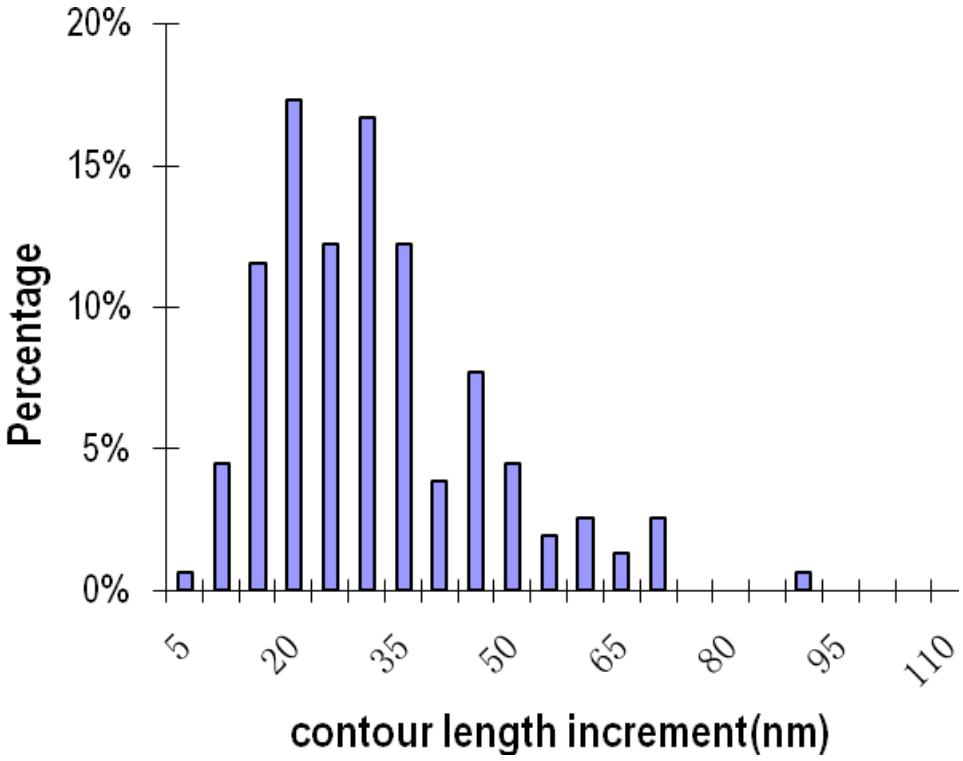

Figure 7.12: Contour length increment histogram of GPIbα-stretch A1A2A3 force-extension curves (in the presence of ADAMTS13). Contour length increment value is from Worm-Like-Chain (WLC) model fitting of force-extension curves. Histogram peaks at 15-20nm and 40-45nm.

Then we compared the extension histogram for those two force drop events after adding ADAMTS13 in the buffer. Figure 7.12 shows that the extension histogram is similar to the extension histogram in the absence of ADAMTS13. There are still two major populations of extension. The highest peak is still 15-20nm. However, there are also obvious shifts from large extension values to small extension values. There are almost no events with extensions over 70nm (only 1% at 90-95nm).

In Figure 7.7, there are a considerable number of events with extension over 70nm. Most bars in the low extension (<35nm) regime have higher percentage. Because we are analyzing the extension values from Worm-Like-Chain model fitting, if the AFM tip picked the same type of A1A2A3 molecules from the Petri dish, the comparative

extension values for cases in the presence of ADAMTS13 would not differ much from those measured in the absence of ADAMTS13, because the cleavage would only happen during the second ascending phase in our analysis method. The current data suggested that the AFM tip was picking up a different batch of molecules which had smaller extension values. Where were the molecules with longer molecular extensions? Most likely those with longer extension values had already been cleaved and only those with shorter extension values were left uncleaved. This could be because different kinds of conformational changes would create different accessibilities for ADAMTS13. And the molecule population with shorter contour length increment would be less vulnerable for ADAMTS13 and thus could better survive the cleavage. When those molecules with longer contour length increments had been cleaved and the percentage of those with shorter contour length increased, we could observe the shift of this extension to smaller values. The histogram still exhibits two similar populations, with percentage peaks at similar locations. This indicates that the molecules keep similar behavior when undergoing conformational change.

Then we continued to analyze the survival rate of the second ascending phase before and after adding ADAMTS13 and EDTA. The survival rate is calculated by counting how many percentages of two-force-drop events have the second lifetime recording as shown in panels B and D of Figure 7.3, that is, the survival rate represents the percentage of second ascending phases that reach the clamping force. The data is shown below in Figure 7.13. In this analysis, we separate the data into two categories by contour length increment <35nm and >35nm. This separation is based on two populations in the extension histogram shown in Figure 7.7 and Figure 7.12. From our model, we hypothesize that most two-force-drop events with extension below 35nm are uncoupling events, and those with extension above 35nm are mostly unfolding events. Based on this hypothesis, the cleavage effect would be minimal for the first extension group because uncoupling of A1 from A2 would not expose the cleavage site in the A2 domain.

However, A2 domain unfolding would expose the cleavage site; thus the cleavage effect will be most evident for the second group with extension value larger than 35nm. The data in Figure 7.13 support our hypothesis.

III. ADAMTS13 Effects on t_{22} Survival Rates

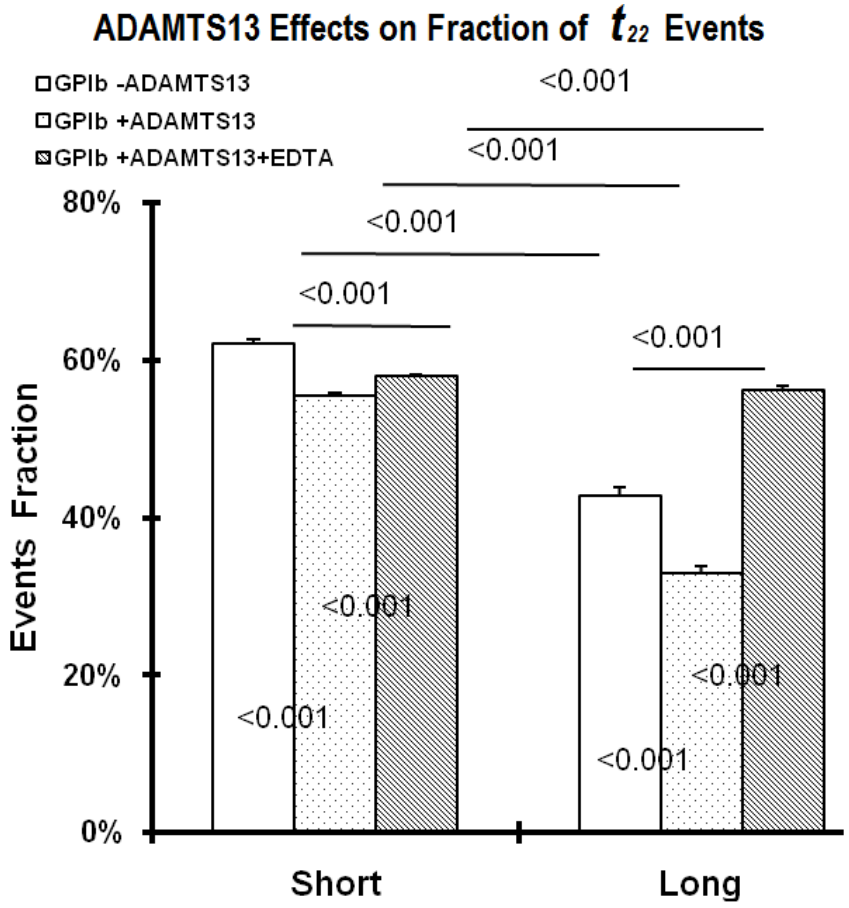

Figure 7.13: Fraction of t_{22} events in the absence (open bars) and presence (dotted bars) of ADAMTS13, and EDTA (hatched bars). Analysis is separated into "short" (putative uncoupling) and "long" (putative unfolding) groups which have contour length increment <35nm and >35nm, respectively. Numbers labeled are p-value for paired t-test.

Figure 7.13 shows the fraction of t_{22} events for GPIbα-stretch VWF A1A2A3 in the absence and presence of ADAMTS13, and EDTA. From all the two force drop events, we counted the percentage of those events that reached the preset force value and

the given lifetime recording. This is another bond strength measurement which is different from a lifetime measurement. It could also provide information on cleavage because cleavage that happens either during the ramping or after the ramping (during lifetime recording) would both affect the survival rate of t_{22}. First, adding ADAMTS13 in the buffer decreased the ability of molecules to reach the preset force value from about 62% to 55% for short extension (<35nm). This percentage decrease was larger (from 43% to 33%) for long extension (>35nm). It strongly supports our hypothesis that unfolding facilitates cleavage because long extension events had higher possibility of unfolding. For the unfolding events, the cleavage could happen either during the second ramping, or after the bond survived the ramping and gave a lifetime recording. Both cases would decrease the t_{22} survival rates: the first one lowered the survival rate directly and the second one would decrease the number of those molecules which have the potential to survive the ramping.

There were still unfolding events having short extension, but the possibility is much lower. Instead, more uncoupling events would fall into this category. Adding EDTA rescued the survival rate of T_{22}, leaving an even higher percentage for the long extension category. This over-compensation may result from the effects of EDTA on A1A2A3 structural change. Comparing the two categories, all the three situations (without ADAMTS13/with ADAMTS13/with ADAMTS13+EDTA) for long extension had lower survival rates than those of short extension. This trend indicates that more events after uncoupling could survive the succeeding ramping. Longer extension does not provide any benefits over surviving the ramp because the longer time for longer extension would subject the molecules to either rupture or cleavage. The putative unfolding would also increase the molecule's contour length and thus lengthen the pathway for force propagation.

IV. ADAMTS13 Effects on Average t_{22}

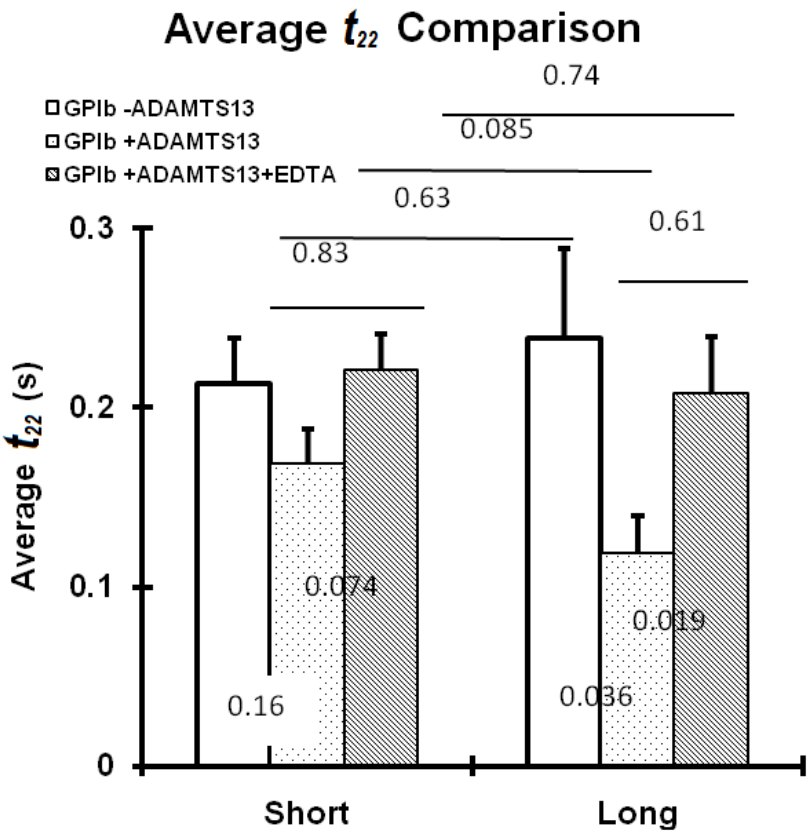

Figure 7.14: Average t_{22} comparison for the condition in the absence (open bars) and presence (dotted bars) of ADAMTS13, and EDTA (hatched bars). As Figure 7.13, analysis is separated into "short" (putative uncoupling) and "long" (putative unfolding) groups which have contour length increment <35nm and >35nm, respectively. Numbers labeled are p-value for paired t-test.

Similar to the analysis above, we averaged the lifetime t_{22} of those events that survived the ramping. Both short and long extension events exhibited obvious effects. For the short extension case, adding ADAMTS13 shortened average t_{22} from 0.21 second to 0.17 second. EDTA brought the t_{22} back to the initial level. For long extension events, adding ADAMTS13 shortened the average t_{22} from 0.24 second to 0.12 second, only half the initial level. Similarly, adding EDTA brought the average t_{22} back to the comparable level. The small decrease of t_{22} indicates that there could still be cleavage effects with

short extension but that small extension did not favor cleavage effects. However, long extension favors cleavage and cleavage effects were most evident with conformational change at a larger scale. The average t_{22} of short and long extension events were at comparable levels, before adding ADAMTS13. However, Figure 7.14 shows that considerably less two-force-drop events could survive the second ramping and give a lifetime recording. The implication is that, although it is hard for longer extension events to reach the preset force, the bond would still maintain the same strength once it climbed up the 'hill'. In other words, the force history does not have much effect on the bond lifetime before adding ADAMTS13 in the system. The effect on GPIbα/A1A2A3 bond lifetime was also minimal for the kind of conformational change that happened before the t_{22} recording.

The sharp contrast between the average t_{22} of short and long extensions after adding ADAMTS13 are strong evidence for observing the cleavage effect. From the structural point of view, longer extensions would expose the cleavage site more and make it more accessible for ADAMTS13 cleavage. It is still not clear whether the cleavage happened during second pulling phase or during lifetime recording after the molecule was pulled to the preset force. One thing definitive is that cleavage took place during lifetime recording and caused an evident decrease in average t_{22}. As discussed previously, this cleavage could also result in a lower survival rate of t_{22} events because cleavage affected the pool of molecules available during the experiments. It is still not clear to what extent the A2 domain should unfold before the cleavage site can be exposed for ADAMTS13. It is also highly possible that cleavage would occur during the second ascending phase, especially for the long extension events. This second type of cleavage would not affect the average t_{22} but would affect the survival rate of t_{22}. Potential A1A2A3 candidates for t_{22} could suffer from being cleaved before reaching the triggering points of the clamping force, thus decreasing the t_{22} survival rates. The longer the extension, the more possibility

for this type of cleavage to happen. Most likely, these two types of cleavage would both take place during the experiments, in a randomized manner.

Because we use the Worm-Like-Chain model to fit the force-extension curve, chances are that those events with long fitted extension values have not been stretched to the same extension. The fitting gave only the patterns of conformational change, and we manually separated the groups in two patterns. Most likely, these two patterns represent uncoupling and unfolding pathways. In this regard, the uncoupling pathway did not favor the cleavage because the A2 domain structure would not be affected by A1 detachment from A2. If an uncoupling pathway has the short contour length increments, the real molecular extension increase would not benefit cleavage because the cleavage site on A2 was always inaccessible no matter how far the A1 domain swung away from the A2 domain. On the other hand, if the unfolding pathway adopts long contour length increments, the molecular extension in those two-force-drop events would help the ADAMTS13 to access the cleavage site. At this stage, we still cannot correlate the extent of the cleavage site exposure to the average t_{22} decrease because t_{22} is related to force level. If the force is high for t_{22}, the molecular extension value would also be high and thus could induce longer unfolding of A2 and more exposure of the cleavage site. A low force t_{22} would give shorter molecular extension even under the long contour length increment category. Therefore, only after analyzing the force-dependent behavior of t_{22} can we make a clearer comparison and offer a more detailed explanation of what happened during the cleavage process.

V. ADAMTS13 Effects on Transition Time and Rupture Time

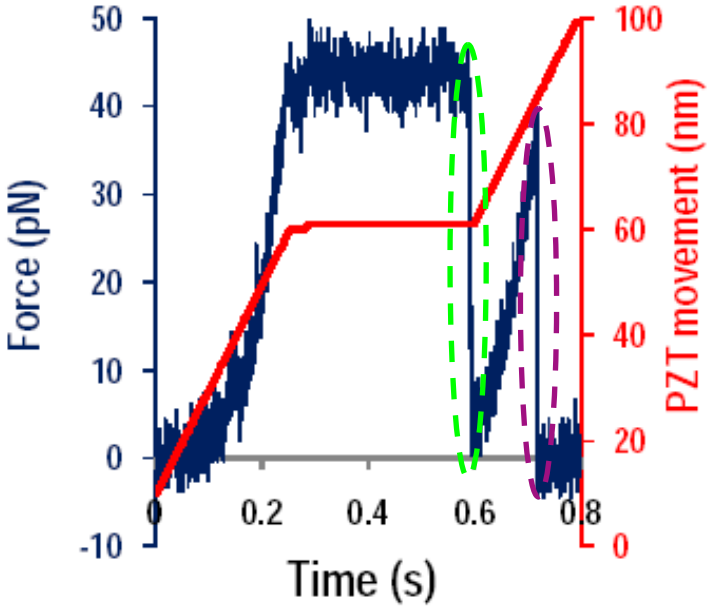

Figure 7.15: Panel C of Figure 7.3 illustrates the measurement of transition time (in dashed green oval) and rupture time (in dashed purple oval).

To further study the conformational change that happened at short and long contour length increments, we analyzed the transition time of the first force drop and the rupture time of the second force drop of two-force-drop events, as illustrated in Figure 7.15. Transition time represents how long the structure needs to adjust to the catastrophic structural change and to transit to the new conformation in response to the applied force after this structural change. Rupture time represents the time for the molecule to fully dissociate from the binding pocket or the time for the A2 cleavage site to fully break in the presence of ADAMTS13. This transition and rupture happened so fast that it only took a couple of milliseconds.

The transition time and rupture time measurements are summarized in Figure 7.16. Before adding ADAMTS13, the transition time is different for the "short" and "long" group of contour length increments. But there were no differences between rupture times for the two groups. This strongly implies that the catastrophic structural

changes for the "short" and "long" groups were totally different; even if the final rupture resulted from the same kind of structural change. As we explained previously, the final rupture could only be bond dissociation of GPIbα from the A1 domain of A1A2A3. So the rupture events would behave the same regardless what kind of structural change happened before that.

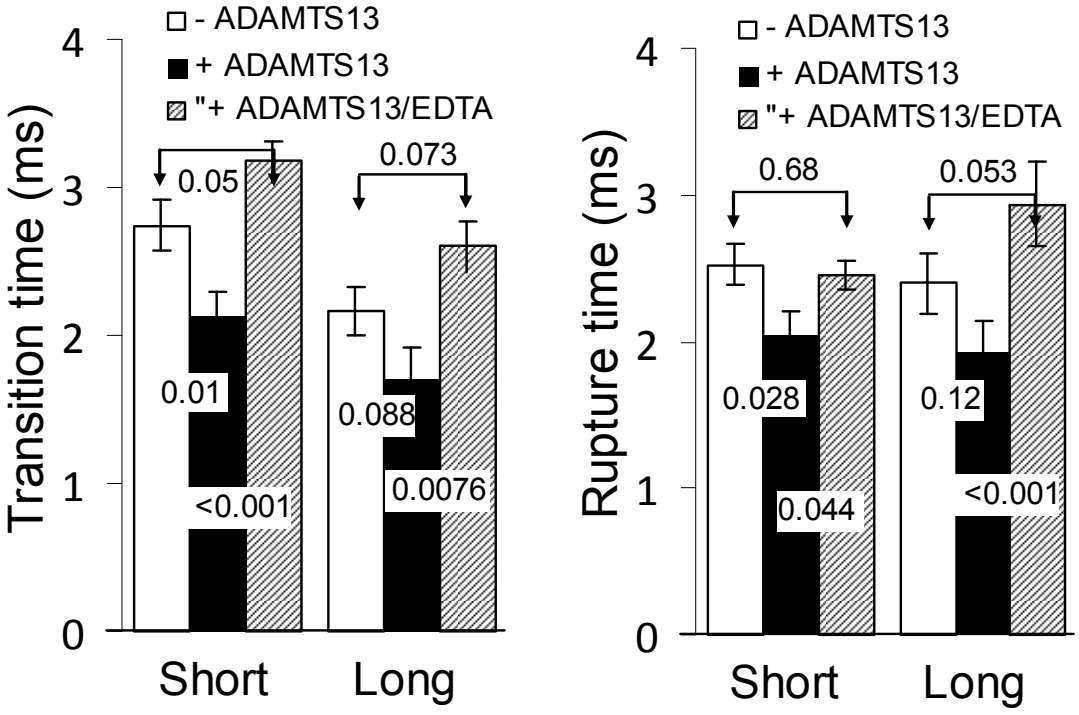

Figure 7.16: Average transition time (left panel) and rupture time (right panel) analysis for GPIbα-stretch A1A2A3 in the absence (open bars) and presence (solid bars) of ADAMTS13, and EDTA (hatched bars). Comparison is separated in two groups with short (<35nm) and long (>35nm) contour length increments. Numbers labeled between bars are p-value for paired t-test.

It is interesting that structure transitions with shorter extension increments took more time than those with longer extensions. These two structure changes could be the same kind. After adding ADAMTS13, both short and long extension groups had shortened transition time, which indicates that ADAMTS13 facilitated the structural change and speeded them up. In the previous chapter, we discussed the binding between ADAMTS13 and A1A2A3. This binding of ADAMTS13 clearly has changed the conformation of A1A2A3 and thus has affected the structural change inside the A1A2A3.

The relative comparison of transition time between the short and long groups after adding ADAMTS13 retained the same features as were found in the case without ADAMTS13, and it confirms this unique observation. Rupture time has also been shortened after adding the enzyme. This shortening could have a couple of explanations: one explanation is that the enzyme cleavage caused faster breakage of this linear linkage of molecules. Compared with the A1 dissociation from GPIbα, the breakage of the backbone covalent bond may need less time because the cleavage only happened between two specific amino acids (102). There are fewer atoms involved than in the receptor-ligand binding pocket. For the GPIbα-A1 interaction, there are more than ten hydrogen bonds involved in the binding pocket (68). And the dissociation may undergo a sliding-rebinding pathway which could be a potential explanation for the GPIbα-A1 catch bond mechanism (29). The other explanation would be the effect of ADAMTS13 binding to A1A2A3. ADAMTS13 could bind to the A3 or the A2 domain of VWF (103). And ADAMTS13 itself is a large multi-domain protein whose binding site with A1A2A3 could also be multiple domains. This binding could easily affect the conformation of A1A2A3 and could induce binding pocket structural change, leading to accelerated dissociation of GPIbα/A1. As before, when adding ADAMTS13, there was still no difference between short and long extension groups in rupture time.

Adding EDTA to the buffer inhibits the function of ADAMTS13. Killing the enzyme prolonged the transition time to the level even longer than the initial condition in the absence of ADAMTS13. This over-compensation brought by EDTA has also been seen for the T_{22} survival rate for the long extension group (Figure 7.13). The short extension group still has longer transition time than the long group, which is consistent with the transition time comparison in the absence and presence of ADAMTS13. The rupture time difference between the short and long extension groups is not significant, and the values are comparable to those obtained for cases before adding ADAMTS13. These data suggest that EDTA not only inhibits the cleavage function of ADAMTS13,

but most likely, it could also inhibit the binding of ADAMTS13 to A1A2A3. ADAMTS13 has to bind to A1A2A3 to cleave, and this could be the reason for transition time shortening. If ADAMTS13 still binds to A1A2A3 after adding EDTA to inhibit its function, the conformational change induced by ADAMTS13 binding would still remain, regardless whether ADAMTS13 could cleave or not. ADAMTS13 is a circulating zinc metalloprotease and its function is highly dependent on the metal ion. EDTA is a metal ion chelator. Therefore, EDTA could possibly affect the binding of the enzyme to its target, making ADAMTS13 totally lose its function. This could be tested by adding EDTA to the system of ADAMTS13 binding with VWF A1A2A3.

Analyzing ADAMTS13 Effects on Force Regulated Binding Kinetics of GPIbα-A1A2A3 Bonds

I. ADAMTS13 Effects on One-force-drop Events t_{11} and Two-force-drop Events t_{22}

Previous analysis provides strong support for our hypothesis and our catastrophic conformational change model. However, as discussed above, to make more detailed comparison of cleavage effects, we need to examine the force regulated binding kinetics of GPIbα/A1A2A3 interaction in the absence and presence of ADAMTS13, and EDTA. We started from measuring the single bond lifetime as shown in Figure 7.17 (scatter plot). By averaging the lifetimes at each specific force bin, we got the results presented in Figure 7.18.

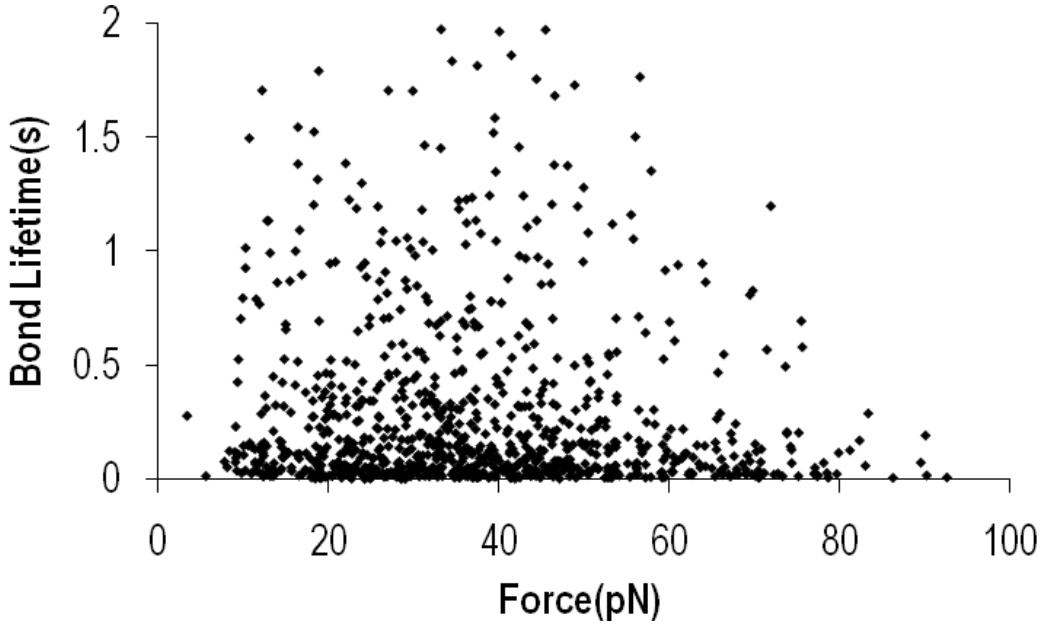

Figure 7.17: Scatter plot of 931 lifetime measurement for GPIbα-A1A2A3 single bond t_{11}.

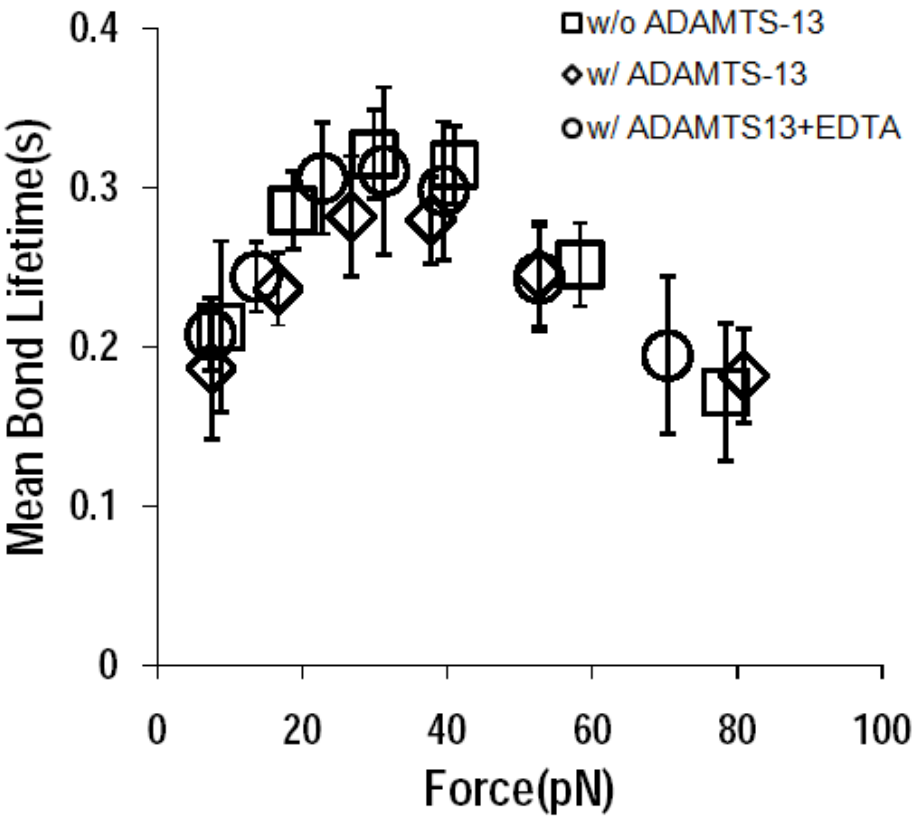

Figure 7.18: Single bond (one-force-drop) lifetime (time-to-rupture) t_{11} in the absence (square), presence (diamond) of ADAMTS13, and EDTA (circle); Error bars are stand error of the mean.

In the absence of ADAMTS13, GPIbα formed catch-slip bonds with A1A2A3 (square). In Chapter 4, we have already shown that GPIbα forms catch-slip bonds with WT A1 and A1A2A3. These data confirmed this observation. In the low force regime, the average lifetime t_{11} increased with increasing force. The average t_{11} peaked at around 35pN with 0.3 second lifetime value. The peak lifetime force is larger than the GPIbα-A1 catch-slip bond, which is around 25pN, but the peak lifetime value is comparable. One possible explanation for this increase in peak force is that A1A2A3 molecules are longer than the A1 domain only. This lengthening of the molecule could affect the binding pocket structure and make it withstand larger force. Furthermore, the A2 domain could couple with the A1 domain, and this coupling could be a strong interaction (117). The A1A2 coupling could also affect the ability of A1 to bind with GPIbα. It is still not clear how this molecular lengthening and domain coupling affects the sliding-rebinding in the binding pocket, if explaining the catch bond in this diagram.

Surprisingly, we found that adding ADAMTS13 did not affect GPIbα-A1A2A3 catch-slip transition or the value of t_{11} in a statistically significant manner (diamond). This indicates that the ADAMTS13 cleavage effect could not be observed through comparing t_{11}. Since t_{11} measures the lifetime before the bond start to rupture, it has no relation with catastrophic structural change inside the molecule. In other words, a single bond lifetime only deals with the strength of the binding pocket without any structural rearrangement. In the analysis and discussion of rupture time, we suggest that ADAMTS13 could bind to A1A2A3 during the process of stretching by GPIbα. And this binding could be one cause of the observed difference in rupture time. It is still possible that ADAMTS13 bound to A1A2A3 during the measurement of bond lifetime before rupture. It is more unlikely that the enzyme would bind to and detach from A1A2A3 during the t_{11} measurement, because the force level remained unchanged during the t_{11} measurement. With high possibility, instantaneous binding and detaching of ADAMTS13 from A1A2A3 would cause conformational change of the A1A2A3 molecule, thus

causing fluctuation of force level of the GPIbα-A1A2A3. Therefore, chances are that GPIbα bound to A1A2A3 with or without ADAMTS13 bound. Even if ADAMTS13 had already bound to A1A2A3 before it was picked up by GPIbα, it also had no effect on GPIbα-A1A2A3 t_{11}, which was shown by data in Figure 7.16. It is still not clear whether ADAMTS13 would affect the rupture time of GPIbα-A1A2A3. The previous difference of rupture time before and after adding ADAMTS13 could result from the effect of ADAMTS13 binding to A1A2A3. It could also result from the catastrophic conformational change of A1A2A3, or both.

Adding EDTA did not affect t_{11} and this is expected (circle), because there is no effect of ADAMTS13 cleavage. The GPIbα-A1A2A3 bond is also metal ion independent. One complication in this discussion is what if ADAMTS13 was bound to A1A2A3 during the t_{11} measurement. In this regard, adding EDTA would inhibit this binding. But because we had not tracked the instantaneous binding of ADAMTS13 on A1A2A3 using the current t_{11} analysis method, we would not be able to quantify this effect. But it will be helpful to analyze the rupture time in the absence and presence of ADAMTS13, and EDTA. If ADAMTS13 binding to A1A2A3 will affect the rupture time, and if that is the cause of the difference between Figures 7.14 and 7.15, then adding EDTA would affect the rupture time from inhibiting ADAMTS13 binding to A1A2A3 of these t_{11} events.

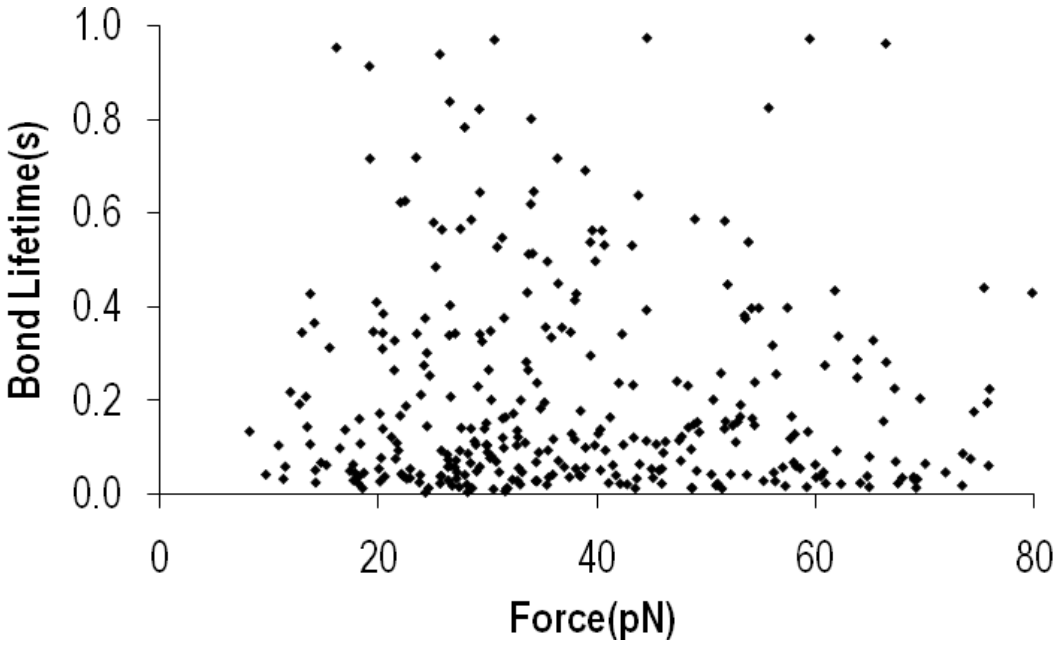

Figure 7.19: Scatter plot of 333 lifetime measurements for GPIbα-A1A2A3 two-force-drop time-to-rupture t_{22} in the absence of ADAMTS13. As shown in the lifetime population, there is very few data over one second. Therefore, we set one second as cutoff line for outliers.

Because we did not observe any difference in the one-force-drop bond rupture lifetime, we started to analyze the two-force-drop events. According to our hypothesis, it is expected that no difference will be observed for single bond t_{11} though, because the A2 domain hadn't unfolded yet to expose the Tyr1605-Met1606 cleavage site. As defined in Figure 7.3, the time-to-rupture t_{22} is the waiting time before the GPIbα-A1A2A3 bond started to rupture. t_{22} happened after the catastrophic structural change. The data in Figure 7.19 shows the scatter plot for all the measurements. The two-force-drop events are very specific bond features, and they are only part of the observation. Not all the two-force-drop events had time-to-rupture t_{22} (Figure 7.3 panel C). Therefore, the productivity for harvesting t_{22} was much lower than for harvesting t_{11}. The scatter plot also shows that the value for t_{22} distribution was in a much lower range than that for t_{11}, suggesting the effect of catastrophic structural change.

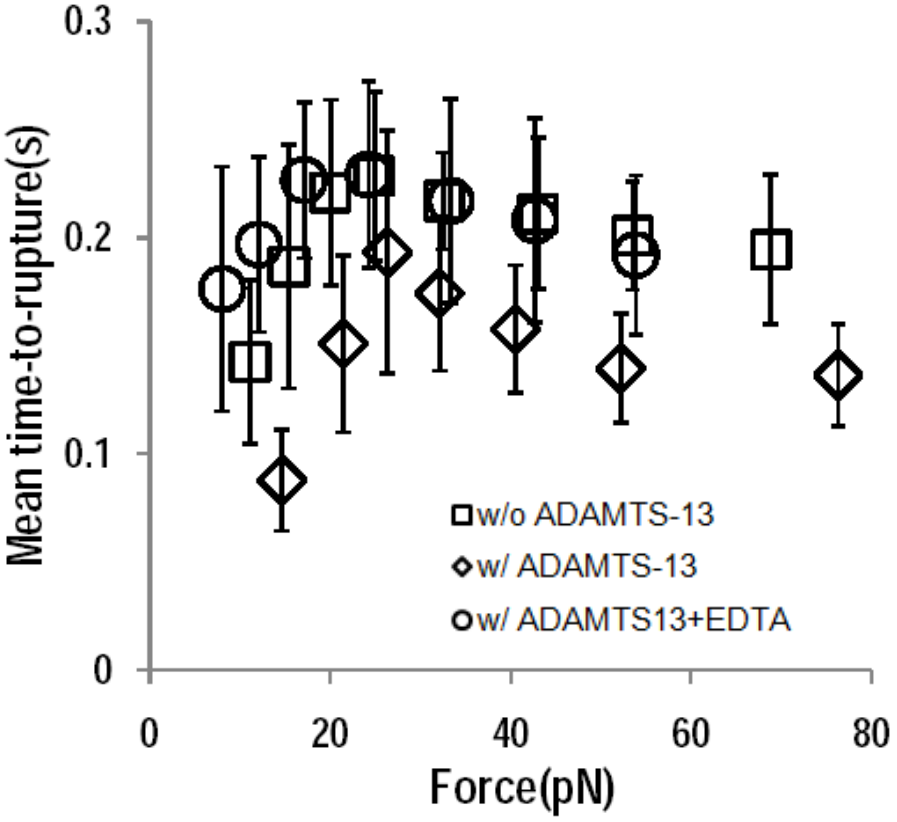

Figure 7.20: Average time-to-rupture t_{22} in the absence (square) and presence (diamond) of ADAMTS13, and EDTA (circle). Error bars are stand error of the mean.

The scatter plot and average lifetime (square) shows the t_{22} curve also had a catch-slip transition shape. The peak force for maximum lifetime is around 25pN, which is lower than the t_{11} peak force (~35pN). The peak average lifetime value is around 0.22 seconds, lower than the 0.31 seconds of average t_{11}. The slip bond regime looks flatter, and thus had a slower decrease than t_{11}'s slip bond. All these differences in time-to-rupture between one-force-drop and two-force-drop events indicated the strong effect of catastrophic structural change on force-regulated binding kinetics of GPIbα-A1A2A3 bond.

Discussions for The Above Data

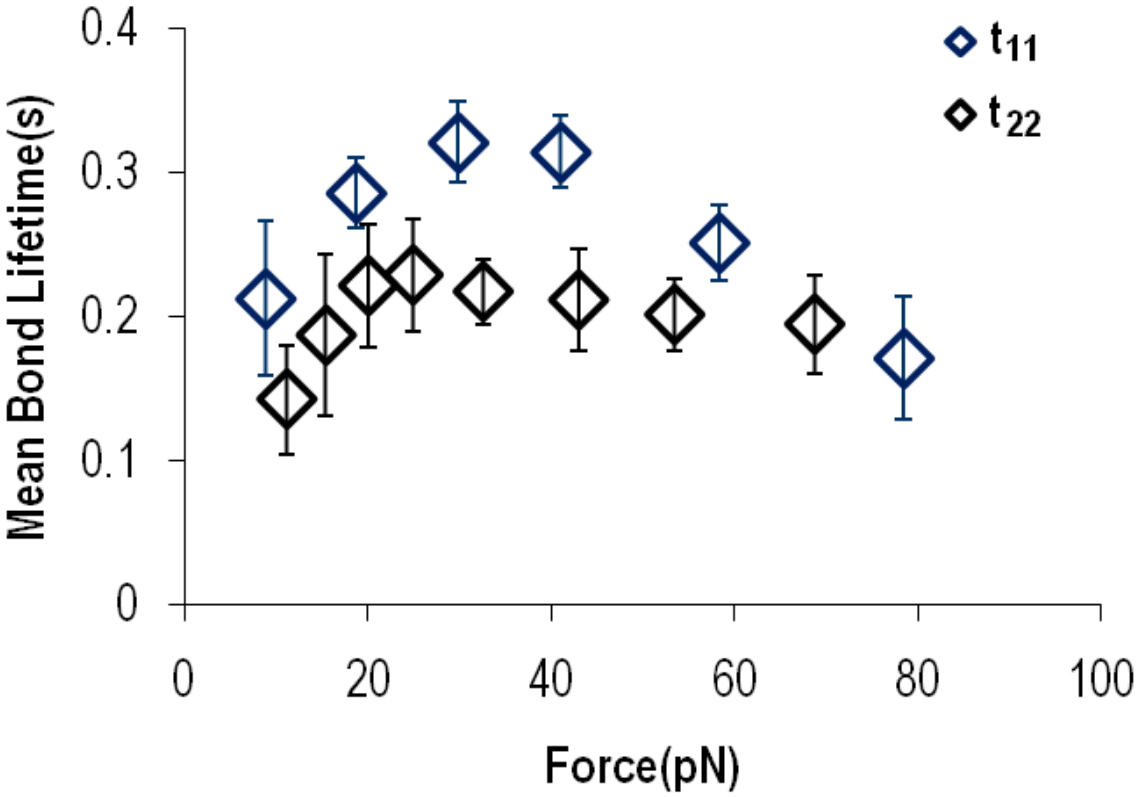

Figure 7.21: Re-plot of average t_{11} and t_{22} for comparison. Both curves are from experiments done in the absence of ADAMTS13.

For comparison, we plotted one-force-drop t_{11} and two-force-drop t_{22} together in Figure 7.21, because both of them measure lifetime before rupture. There are several observations from these data. First, structural change (A2 unfolding or A1A2 uncoupling) weakened the bond and thus shortened the bond lifetime (there is still no cleavage yet) in the whole force range (Figure 7.21). In this scenario, the first ascending phase of stretching and the catastrophic structural change had already applied force history on the binding pocket of GPIbα-A1A2A3. This force history had a negative effect on the bonding strength. Second, the catch-slip biphasic pattern has been retained and this implies that the effect of preloading force history was still quantitative but not qualitative. There could also be conformational changes in the binding pocket during the preloading

history, but this disruption has not been deterministic. If the sliding-rebinding model could still be applied to explain this t_{22} catch-slip transition, then the structural change would have only affected the hydrogen bonds' number in the sliding pathway because some sliding-rebinding might have already happened before the final rupture started. Third, the shortening of t_{22} was not equal under each force level. In the comparison of average t_{11} and t_{22} values in Figure 7.21, the bond lifetime shortening was about the same at the low force (<25pN) regime. But this shortening effect decreased with force, starting from around 35pN, and was minimal at large force around 70pN. One possible explanation is that, after the preloading history resulting from the first ascending phase and the catastrophic structural change, the bond would not be as sensitive to force as before. This caused the slip bond regime to flatten towards more ideal bond behavior. From the structural point, the preloading history might have created some conformational change in the binding pocket and thus might have decreased the capacity for further conformational change in adjustment to the external forces. In other words, preloading would 'prepare' the structure to a force-favored conformation for future force loading, but at the expense of possibly breaking the hydrogen bonds which could be used by the structure to respond to the force imposed at the very beginning of loading; this would decrease the overall ability of the binding pocket structure to respond to a certain force level. This decrease in force resistance was obvious at the lower force level, but may not be of the same importance in the higher force level.

Adding ADAMTS13 did not change the catch-slip transitional bond behavior for t_{22} but shortened the t_{22} in the whole force range, with maximal decrease occurring at low force levels. The first point of t_{22} in the presence of ADAMTS13 had only half the value of that in the absence of ADAMTS13. This t_{22} shortening in the presence of ADAMTS13 decreased with increasing force until it reached a constant level after both t_{22} curves peaked at around 25pN (Figure 7.20 and Figure 7.21). Adding EDTA totally abrogated this t_{22} shortening. The t_{22} curve for addition of EDTA in the presence of ADAMTS13

collapsed very well with that representing no addition of ADAMTS13. Compared with single bond rupture lifetime t_{11} in Figure 7.18, these data revealed that ADAMTS13 had an obvious effect on two-force-drop events time-to-rupture t_{22}, but had no obvious or no effect on one-force-drop events time-to-rupture t_{11}. These data strongly support our hypothesis that catastrophic structural change in A1A2A3 is required for the ADAMTS13 function to cleavage at A2. This cleavage could be totally inhibited by adding the metal ion chelator EDTA in the buffer, indicating that the function of this metalloprotease was also strongly dependent on metal ion.

The other possible explanation for these data is that the accelerated dissociation of GPIbα from A1A2A3 was due to the binding of ADAMTS13 to A1A2A3, but not to the cleavage from A1A2A3 of ADAMTS13. However, the single bond lifetime data in Figure 7.18 strongly disputes this argument. If the accelerated dissociation was from ADAMTS13 binding, then we should also observe it in the single bond lifetime comparison. In the previous chapter we showed that ADAMTS13 could bind to A1A2A3 and actually form a catch-slip transitional bond in the whole force range. Therefore, it is unlikely that accelerated dissociation but not cleavage, facilitated by ADAMTS13, required A1A2A3 structural change. On the contrary, this quantitative shortening of time-to-rupture was most likely from the cleavage effect of ADAMTS13 on A1A2A3, validating the necessity for structural change of A1A2A3 to expose the cleavage site Tyr1605-Met1606 on A2 domain. The other potential method to prove this cleavage is to collect the buffer after AFM experiments and to run the western blot to visualize the cleavage products.

II. Tensile Force on GPIb-A1A2A3 Weakens ADAMTS13 Cleavage Effects

To further quantify the ADAMTS13 cleavage effect on t_{22} shortening, we re-analyzed the raw t_{22} data according to different bin sizes. The whole force range for the data was divided by the same force increment (5pN). On each force level, we tried

different force bin sizes for optimization as shown in Figure 7.22. Because the amount of data is limited, we could not use too small of a force bin size. Otherwise there would be too much fluctuation noise in the curve. With the increase of force bin size from 15pN to 25pN, the average t_{22} curve (in the presence of ADAMTS13) became flatter because the averaging eliminated the large fluctuation. We do not want too much fluctuation as shown in 15pN bin size (green solid diamond). On the other hand, we don't want too many details being flattened out as 25pN bin size (red) either. Therefore, a 20pN bin size was chosen to compare the t_{22} difference by cleavage effect.

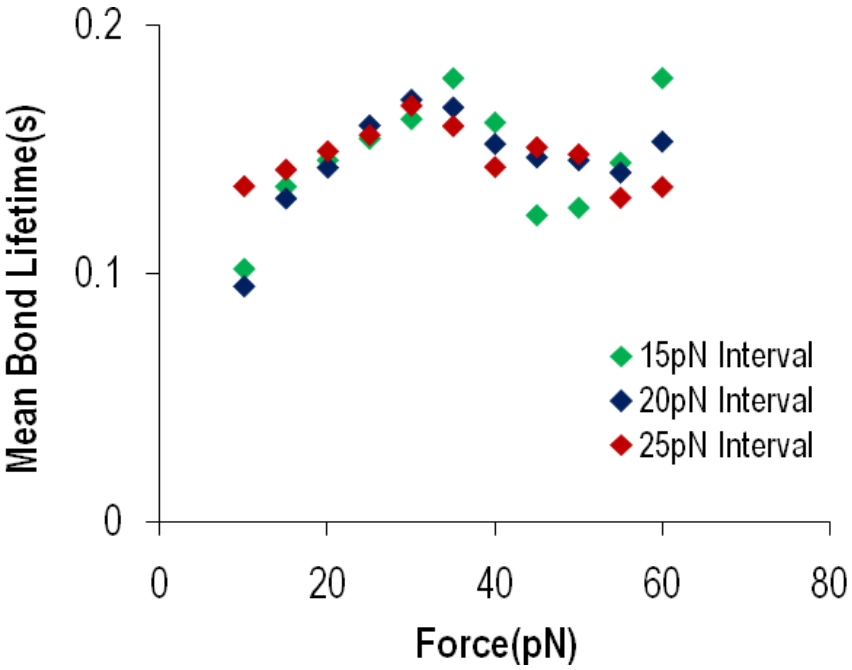

Figure 7.22: Comparison of different force bin size effect on averaged time-to-rupture t_{22} in the absence of ADAMTS13. When bin size increases from 15pN (green) to 20pN (navy) and 25pN (red), detailed variations become smoothed out. For each curve, force increment is set to 5pN.

Figure 7.23 panel A illustrates the comparison of averaged t_{22} based on same bin size (20pN) analysis. Panel B shows the off-rate difference calculated from averaged t_{22} difference. Off-rate is the reciprocal of average lifetime. Adding ADAMTS13 shortened the averaged t_{22} and thus increased the bond off-rate. The dependence of this off-rate

increase on force implies how the force regulated the cleavage effect of ADAMTS13. Figure 7.23 is another presentation of the data in Figure 7.20. ΔK_{off} decreased sharply at the low force level until it reached a plateau after 25pN. These data implied that the stretching force on GPIbα-A1A2A3 bonds had a negative effect in regulating the cleavage by ADAMTS13. This observation was out of our expectation but interesting.

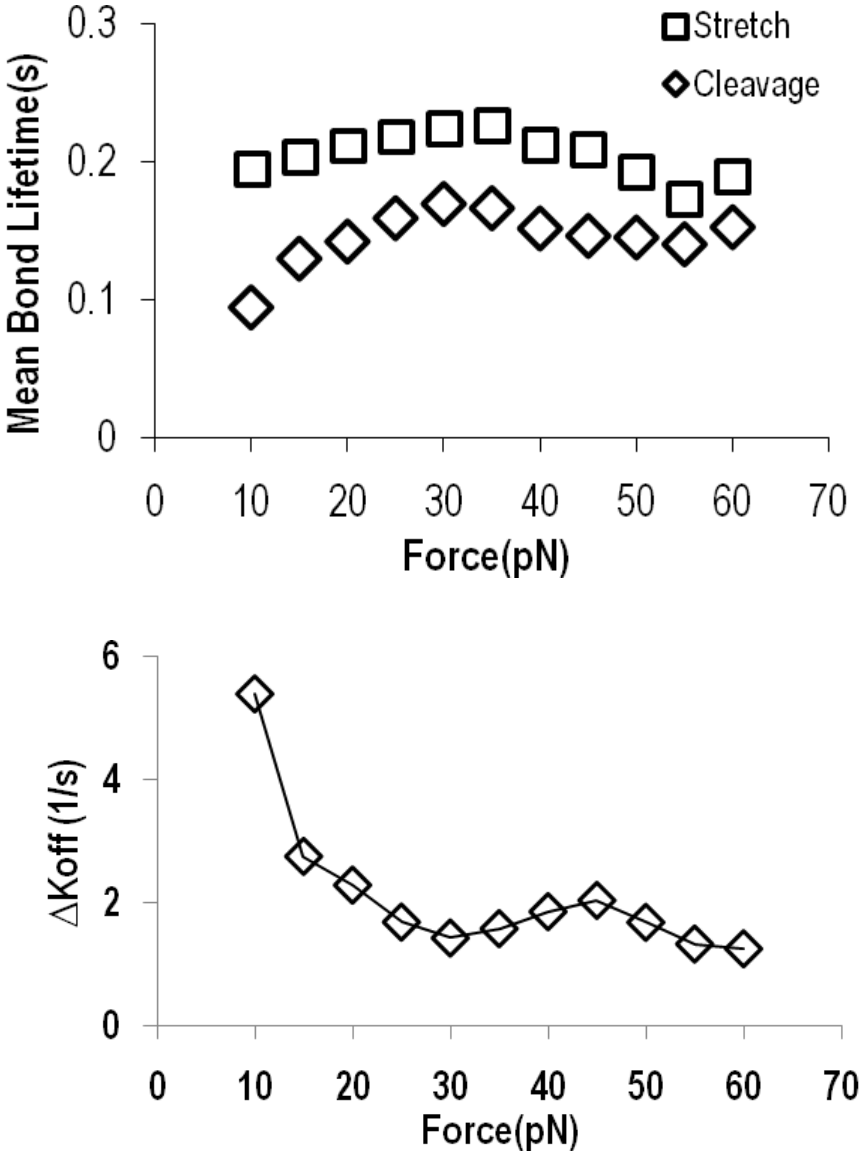

Figure 7.23: Comparison of averaged t_{22} based on same bin size (20pN) analysis (upper panel) and off-rate difference calculated from averaged t_{22} difference (lower panel).

Discussions for The Above Data

The force corresponding to t_{22} is not the force causing A1A2A3 catastrophic structural change, which corresponds to t_{21}. Instead, it is the peak force before the bond rupture (refer to Figure 7.3). Therefore, the A2 domain cleavage site might have already been exposed and subjected to ADAMTS13 cleavage. Here the force contributed to the stretching of the A1A2A3 molecular peptide backbone which includes the Tyr1605-Met1606 cleavage site. It is still unclear how this stretching force affected the orientation of the Tyr1605-Met1606 covalent bond and prepared it for cleavage.

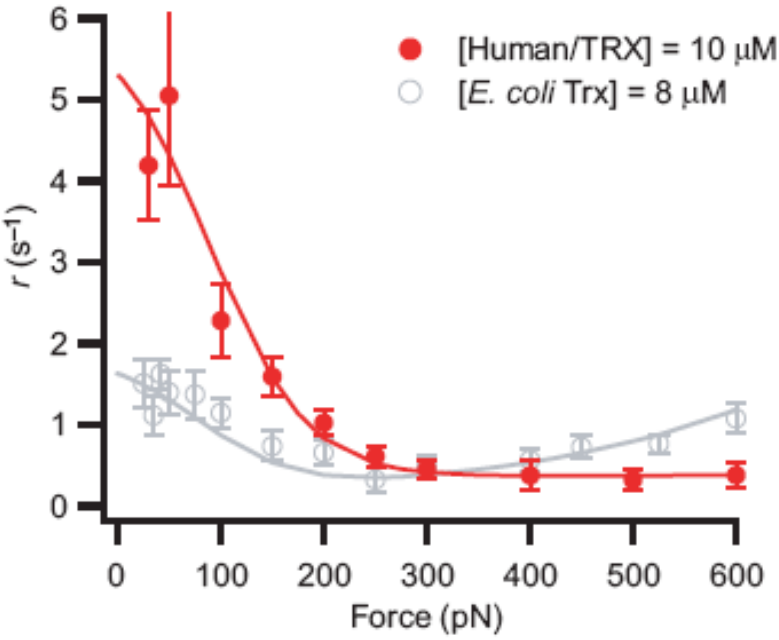

Figure 7.24: Trx reduction rate on disulfide bonds depends on stretching force on eight tandem repeat of I27 polyprotein. (Adapted from (118))

According to a paper published by Dr. Fernandez' group (118), force decreased the reduction rate of Thioredoxin (Trx) on the eight disulfide bonds buried in eight tandem I27 (Ig) domains (Figure 7.24). In their model, they argued that if the thioredoxin had to bind I27 to reduce the disulfide bond, the reduction rate curve would flatten out in large force level. If thioredoxin could reduce the disulfide bond without binding to the substrate I27, the reduction rate curve would decrease first and would then increase again

like *E. coli* Trx, as shown in the figure. Our off-rate deduction result simulates the result of Wiita et al., also giving a negative correlation on force. Putting in the schematic of their model, the flattening of ΔK_{off} at large force of our result implied the ADAMTS13 had to bind to A1A2A3 to cleave. In other words, ADAMTS13 could not function by attacking Tyr1605-Met1606 with the enzyme still isolated from its substrate. In the paper, Wiita et al. proposed a model to explain the negative regulation of reduction rate by force. The two sulfide atoms of the disulfide bond had to adopt a certain orientation (a kink from the backbone) with Trx for the reduction to happen. Stretching force straightened the backbone with the disulfide bond and hindered the formation of optimal orientation for reduction. A larger stretching force provided a higher energy barrier for adopting the optimal geometric conformation, thus decreasing the reduction rate. For the ADAMTS13 cleavage site Tyr1605-Met1606 in A2, there is still no crystal structure resolved, nor does the ADAMTS13 and the ADAMTS13-A1A2A3 co-crystal. Nevertheless, ADAMTS13 cleavage on A1A2A3 is also an enzyme-substrate interaction, which is similar to the Trx-I27 polyprotein interaction. Therefore, it is highly possible that Tyr1605-Met1606 would also assume a certain orientation with ADAMTS13 for the cleavage to happen. If the orientation does not favor stretching force, then we would observe negative regulation of cleavage by force. One major difference in the force regulated reduction rates vs. off-rate deduction is the force scale: we used much smaller force (ten fold smaller) than the Trx reduction of disulfide bonds. This difference could result from the different strength of molecules in resisting external force. The VWF molecule is subject to venous and arterial blood shear force. I27 is from the cardiac muscle protein titin, which has to possess much higher strength in the high frequency cyclic strain environment than the blood vessel molecule VWF. Previous studies also revealed the unfolding force for titin is much higher (several hundred pN) than what we observed for A1A2A3 (several ten pN) in the comparable loading rates (119).

III. ADAMTS13 Effects on Two-Force-Drop Events t_{21}

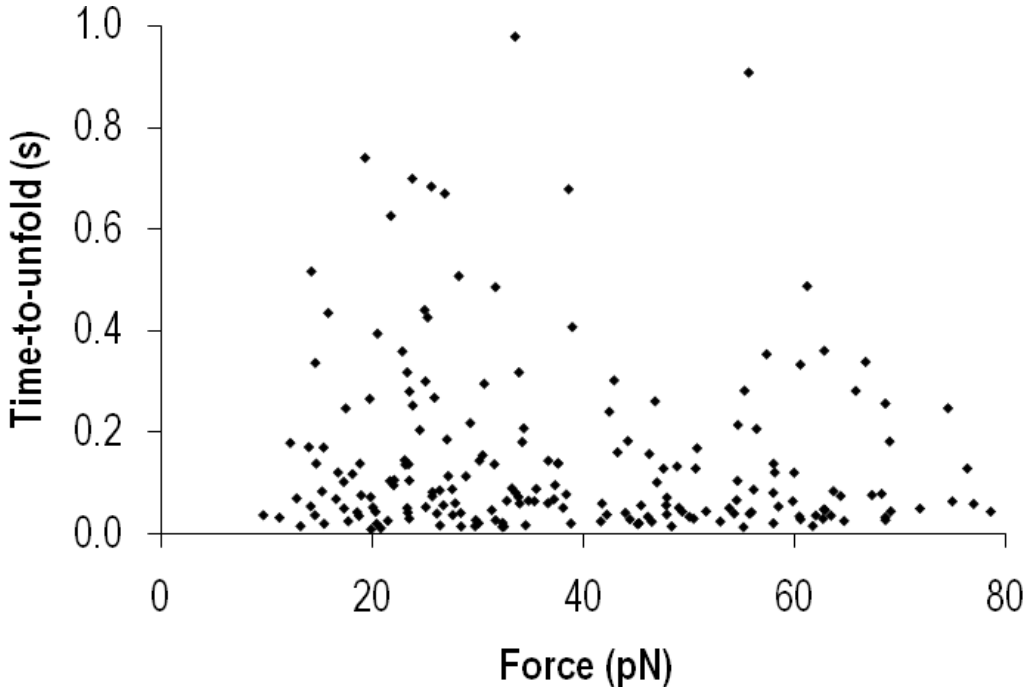

Figure 7.25: Scatter plot of 207 measurements for GPIbα-A1A2A3 two-force-drop time-to-unfold t_{21} in the absence of ADAMTS13. As in Figure 7.19, we use one second cutoff line to filter out the outliers.

After examining the effects of ADAMTS13 on time-to-rupture t_{22}, we analyzed whether the enzyme also had any effect on time-to-unfold t_{21}. The word "unfold" was used to represent universal catastrophic structural change, including the possibilities of A2 domain unfolding, of A1A2 uncoupling, or more. Figure 7.25 shows the scatter plot of 207 measurements of "waiting time before structural change" t_{21} with the absence of ADAMTS13. Figure 7.26 shows the averaged t_{21} based on random force bin. From both the raw data and the averaged results, we found that t_{21} had an even lower value than t_{22} in the whole force range, not to mention t_{11}. It was most difficult to harvest this time-to-unfold t_{21}, compared with t_{11} and t_{22}.

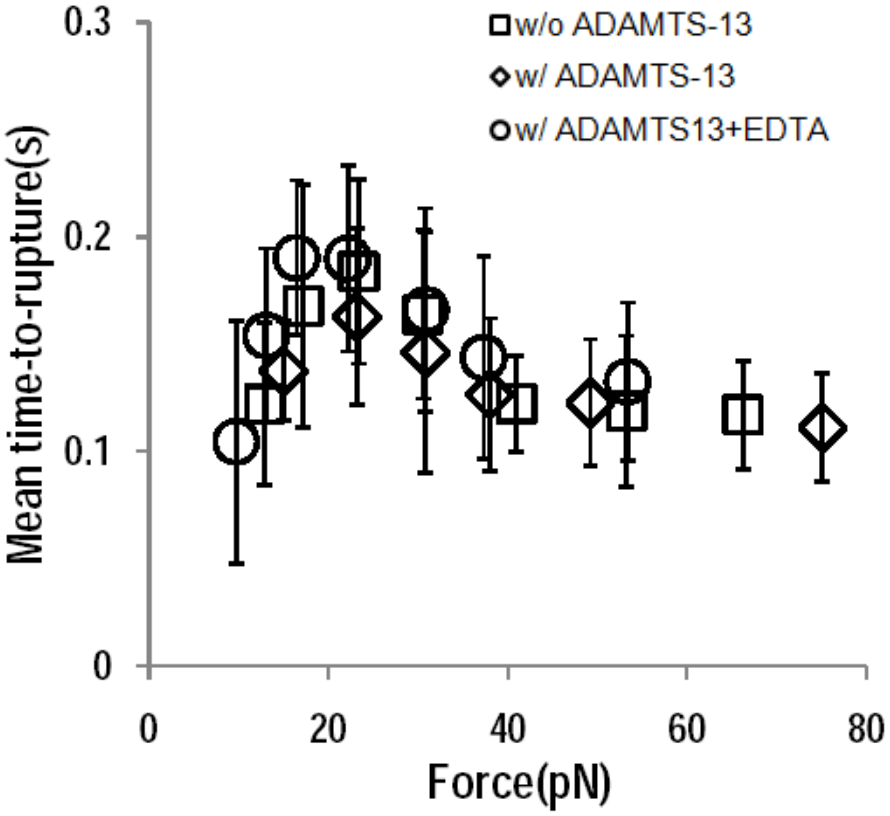

Figure 7.26: Average time-to-unfold t_{21} in the absence (square) and presence (diamond) of ADAMTS13, and EDTA (circle). Error bars are stand errors of the mean.

Discussions for The Above Data

Both figures show that t_{21} behaved as a catch-slip transitional bond, which is similar to t_{11} and t_{22}. Adding ADAMTS13 and EDTA does not affect the binding kinetics qualitatively or quantitatively. It is interesting for us to find the catch-slip transitional bond behavior for the waiting time before catastrophic structural change. The structural change inside the A1A2A3 molecule possibly results from the inter-domain hydrogen bonds breaking between A1 and A2, or from the intra-domain hydrogen bonds breaking between secondary structures (eg: α-helix and β-sheet) inside the A2 domain. The former one would lead to A1A2 uncoupling and the latter one would cause putative A2 unfolding. Currently, the t_{21} data shows the combinational behavior of these two possible

structural changes, which could also be the response of the A1A2A3 molecule to the external shear stress in the blood stream. In the last chapter, we showed the catch-slip transitional bonds for ADAMTS13 binding to A1A2A3. This is another example of combinational effects for multi-domain interaction. Putting in the schematic of the molecular mechanism for catch bonds, there could be several possibilities, including the sliding-rebinding model, the induce-fitting model, and more (120, 121). Most of these explanations include the breaking or formation of hydrogen bonds in the binding pocket. Essentially, structural change inside the molecule retains all the features of protein-protein non-covalent interaction but only on a smaller scale. Currently, there are still no reports for the catch bond behavior for "structural change lifetime" inside a specific molecule. Our findings are uncommon in revealing this possibility and common in explaining the possible mechanism that underlies this behavior.

The catch-slip transitional bond of t_{21} could be a protective mechanism for the A1A2A3 molecule in response to external shear stress. When the ULVWF molecules are first secreted into the blood stream and immobilized on the membranes of endothelial cells, they would be quickly cleaved by ADAMTS13 because the stretching force level is much higher when many platelets bind to these long strings of hyper-adhesive molecules (122). The intensive stretching imposed on the molecules could induce quick structural change inside the molecule, thus facilitating cleavage by ADAMTS13. This cleavage would produce many much smaller pieces of plasma VWF flowing with platelets inside the blood vessel, and these plasma VWF are much less adhesive for platelets than the ULVWF. On the other hand, the human body wants to limit the plasma VWF to a certain amount and size, not losing its normal function to bind platelets in emergency situations (like bleeding). Therefore, the size of plasma VWF would serve as a regulation mechanism to control the extent of cleavage. But how does the ADAMTS13 know that the plasma VWF is in the proper size? The key regulator could be the stretching force on VWF molecule. When the multimer VWF molecule size decreases from cleavage, the

number of platelet binding sites also decreases. A decrease in the number of platelets binding would cause a decrease in the stretching force on A1A2A3, leading to a prolonged time-to-unfold, making it more difficult for ADAMTS13 to access the cleavage site. This protection of the cleavage site at a smaller force level would help preserve the amount of proper size plasma VWF and would prevent further inadvertent cleavage.

The catch bond regime might be another protection against unintentional cleavage. The first step of hemostasis is the recruiting of patrolling platelets to the site of vascular injury. Platelets then bind to VWF that is immobilized on the exposed subendothelium surface on which collagen has been expressed. The binding of the first batch of platelets provides substrates for more platelets to bind to form the blood clotting matrix, which consists of collagen, immobilized VWF, platelets, $\alpha_{IIb}\beta_3$ integrin, plasma VWF, fibrinogen, etc. At this stage, binding of immobilized VWF to collagen serves as the anchoring point for all the above substances. Binding of plasma VWF to activated $\alpha_{IIb}\beta_3$ integrin also creates bridges between platelets. These anchoring and bridging points do not want to be cleaved by ADAMTS13, even inadvertently, because of the stretching force on it. Therefore, increasing force prolongs the time-to-unfold, providing strong protection against the A2 domain from being cleaved by ADAMTS13 when it functions as an anchoring point. One argument for this catch bond is the short time-to-unfold at very small force level (<10pN). We think that at this small force, the A2 domain may unfold. But our studies also showed that ADAMTS13 also had a very short lifetime with A1A2A3 under low force. Consequently, ADAMTS13 may not have a chance to cleave A1A2A3 at low force level. From these discussions we can see that the force regulated cleavage is highly convoluted because of the number of proteins involved and because their functions are different under different shear force conditions (eg: immobilized VWF and plasma VWF).

The analysis for transition time shortening after addition of ADAMTS13 (Figure 7.15) revealed that the possible binding of ADAMTS13 on A1A2A3 affected the duration of the molecular adjustment to the force after the structural changes but did not affect the molecule's ability to have structural changes. This is reasonable because time-to-unfold is a hundred-fold larger than the transition time. And the effects of other protein binding were not pronounced enough to affect the dissociation of strong inter-molecule interaction. But the additional mass change could be involved in the re-structure process after catastrophic structural change happened.

From all the analysis and comparison of t_{11}, t_{22} and t_{21}, we reached the conclusion that only after structural change to A1A2A3 would the ADAMTS13 have effects on GPIbα-A1A2A3 binding, with the most likely the cleavage effects being to shorten the lifetime t_{22}. As for the lifetime analysis depending on force, we continued analyzing the ADAMTS13 effects on t_{22} survival rates and on real molecular extension between two force drops. The rationale for these analyses is to build a correlation of these parameters with force and to provide additional evidence for ADAMTS13 cleavage effects.

Analyzing ADAMTS13 Effects on Force Regulated Extension and t_{22} Survival Rates of GPIbα-A1A2A3 Bonds

I. ADAMTS13 Effects on Force Regulated Extension S_{21} and S_3

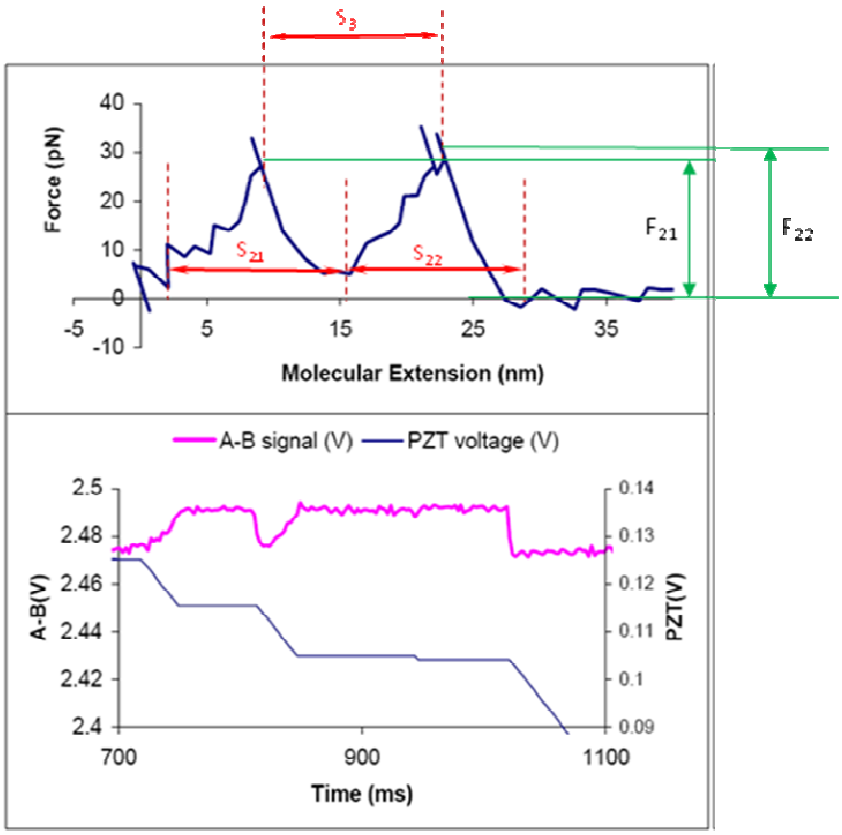

Figure 7.27: Method for measuring S_{21}: the actual molecular extension for the catastrophic structural change (first force drop), and S_3: extension between two force drops. The forces corresponding to S_{21} and S_3 are different: F_{21} for S_{21} and F_{22} for S_3.

Figure 7.27 shows the method we used to analyze S_{21} and S_3, the actual measured molecular extension (not from WLC model fitting) for the catastrophic structural change (first force drop) and the extension between two force drops, respectively. For S_{21}, we picked the lowest point of the force-extension curve after the first force drop and

extrapolated the same force value of that point leftward. The point with same force value would be taken as the initial point to calculate the extension difference.

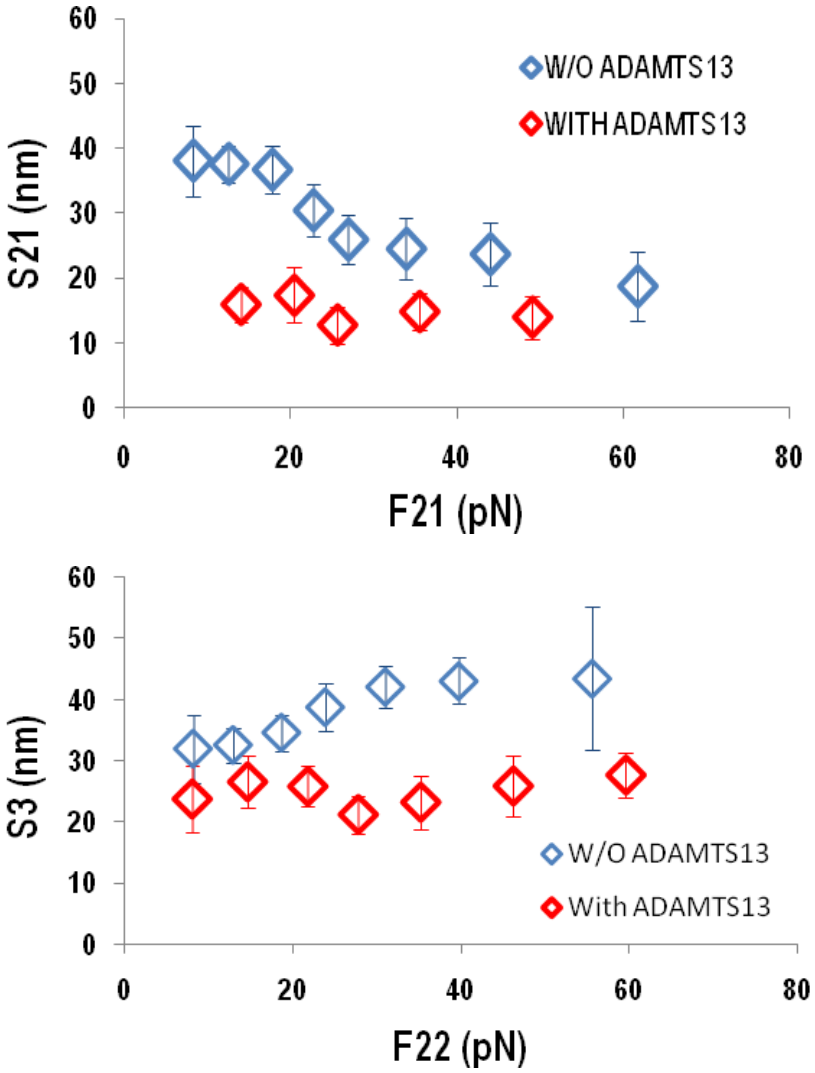

Figure 7.28: Force dependence of S_{21} (upper panel) and S_3 (lower panel), in the absence (navy diamond) and presence (red diamond) of ADAMTS13. S_{21} and S_3 exhibits different dependence on force. ADAMTS13 decreased both extension in the whole force range. The forces corresponding to S_{21} and S_3 are different: F_{21} for S_{21} and F_{22} for S_3. (Refer to Figure 7.27)

For S_3, the extension between two force peaks would be measured. Figure 7.28 gives the analysis results for S_{21} and S_3, both showing decreases after the addition of ADAMTS13. Previous analysis shows there is no effect of ADAMTS13 on t_{21}, but why could we still observe the shortening of S_{21}? One possible explanation might be that

ADAMTS13 preferably cleaves molecules with long S_{21} (thus providing more exposure for the cleavage site); therefore it changes the population in our analysis and we measured those with short S_{21}. A molecular population with short S_{21} will not necessarily give shorter t_{21} than those molecules with long S_{21}; thus there is no difference observed for t_{21}.

Discussions for The Above Data

Most likely, the molecular population with shorter S_{12} has undergone A1A2 uncoupling events. These events would give molecular extensions that are more insensitive to force than the unfolding events because A1A2 uncoupling would only give 15-20nm molecular extension based on our model (Figure 7.10). And this swinging out of the A1 domain from the A2 domain would not be as sensitive to force as the unfolding case because unfolding could have several steps depending on different force levels. This reasoning is also strongly supported by the observation that the S_{12} value falls precisely in the range of 15-20nm in the whole force range after adding ADAMTS13.

S_3 has longer values than S_{21} in the absence/presence of ADAMTS13. The shortening of S_3 after adding ADAMTS13 could come either from the cleavage during ramping (second ascending phase) after unfolding, or from a selected population of the smaller extension group after gradual depletion of the long extension group. Combined with t_{22} and ΔK_{off} data, we found the ADAMTS13 cleavage effects were minimal on S_3 but maximal on t_{22} and thus on ΔK_{off} under low force. This observation suggests that in our analysis, most cleavage happens during the lifetime t_{22} recording. In other words, much less cleavage happened during the second ascending phase ramping, thus leaving S_3 unaffected because cleavage happened during t_{22} recording. Why was there not much cleavage during the second ascending phase (revealed by ADAMTS13 S_3)? Probably because the time was too short for ADAMTS13 to function before A1A2A3 survived the second ramping. Based on the 200nm/s loading rate, a 20nm extension after first force

drop would only take ~0.1 second, similar to the averaged t_{22} at around 10pN in the presence of ADAMTS13. Hence, low force would favor structural change (low t_{21}) but would also cause a reduction in the time for the enzyme to function.

Larger force induced shorter S_{21} but longer S_3. The measurements of S_{21} were based on the force level of the first ascending phase and right before the second ramping started (Figure 7.27). Therefore, it also depends on the starting force level of the second ramping phase. Reductions in the force required for the second ramping to start, coincided with longer measurements for S_{21} (bottom line of the first peak). From the molecular fingerprints for putative uncoupling and unfolding, we found that the residue force (the force at the start of second ramping) level for putative uncoupling was obviously higher than those of unfolding (Figure 7.6). This could result from much less time being allowed for the structure to resume the zero force conformation after the smaller scale structural change of uncoupling than unfolding. The decrease of S_{21} on larger force F_{21} could come from a population shift from "uncoupling" to "unfolding". It is possible that A1A2 coupling can withstand larger force than the A2 domain before structural change happens. Consequently, most of the putative "uncoupling" events would support a large F_{21} but would only give small S_{21}, which was observed as the decrease in S_{21}. This reasoning is consistent with data in the presence of ADAMTS13 in that cleavage does not affect uncoupling because the cleavage site is still buried inside the A2 domain, thereby the shortening effect on S_{21} is not discernible at large F_{21}.

S_3 provided information for the ability of A1A2A3 to change configuration in response to the structural change that was inflicted from the beginning of the first force drop. S_3 had a steeper slope increase between 20pN and 30pN, which could result from an extension population shift from more putative uncoupling to more unfolding events. With a high possibility, the increase of S_3 by larger force value came more from the longer ramping phase than from the longer unfolding. With larger stretching force F_{22} causing longer extension, the percentage of unfolding events increased at the same time.

The consequence of this would be lower residual force that facilitated even longer ramping.

II. ADAMTS13 Effects on Force Regulated t_{22} Survival Rate

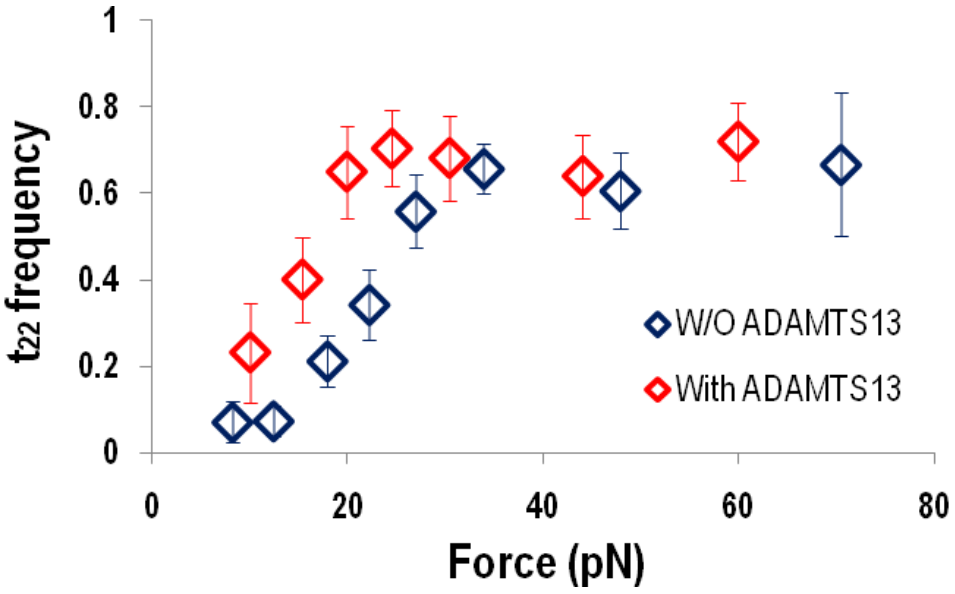

Figure 7.29: t_{22} survival rates vs. force comparison for the condition in absence (navy diamond) and presence (red diamond) of ADAMTS13. Error bars are calculated from standard deviations of binomial distribution in each force bin.

Similar to the lifetime and molecular extension analysis, we tried to look more closely at the force regulated t_{22} survival rate, which could provide additional information on the cleavage effects and could help us understand more about the data from the previous analysis. In Figure 7.13, we analyzed the average t_{22} survival rate for the putative uncoupling and unfolding group (short and long). Again, the survival rate is calculated by counting the percentages of two-force-drop events that have the second lifetime recording as shown in panels B and D of Figure 7.3, that is, the percentage of second ascending phases reaching the clamping force. Figure 7.29 shows the comparison of t_{22} survival rates of GPIbα stretching A1A2A3 when in the absence and presence of ADAMTS13.

Including all the two-force-drop events regardless of giving lifetime t_{22} or not, the t_{22} survival rate indicated the GPIbα-A1A2A3 bonds' ability to survive the ramping. Therefore this could be looked on as another measurement of bond strength. In the absence/presence of ADAMTS13, both conditions gave increasing t_{22} survival rates with increasing force at low force levels. In the absence of ADAMTS13, the curve (navy) reached a plateau at around 30pN, giving maximal survival rate values around 70%. Adding ADAMTS13 shifted the ascending curve (red) towards lower force level, with maximal survival rates at around 20pN. The peak value of the red curve is at the same level as the navy curve, suggesting ADAMTS13 would not affect the survival rates at high force levels. The ascending phase of survival rates was consistent with the observation of t_{22} catch bond behavior. Although more lifetime observations would not guarantee longer lifetime, the ability of the bonds to survive larger force ramping is another indication of increasing bond strength. The lowest force hardly supported lifetime events, thus giving a very low percentage count (near zero). The force level for the ascending phase coincided with that of the slope changing phase for S_3 in the absence of ADAMTS13, indicating the possible population shift of structural change group from uncoupling to unfolding also had positive effects on survival rates. Nevertheless, both the putative uncoupling and unfolding events would not conflict with the catch bond behavior because they were both structural changes happening before the final bond rupture.

Discussions for The Above Data

The interesting observation of the survival rates' increase at low force after adding ADAMTS13 implied that the possible ADAMTS13 binding to A1A2A3 actually "helped" the GPIbα-A1 bonds to survive the ramping and reach the preset force. We still need to bear in mind that all these happened after the A1A2A3 molecule endured catastrophic structural change. Compared with the survival rate data shown in Figure

7.29, the group with long contour length increments (putative unfolding) had much lower t_{22} survival rates averaged from the whole force range, and the group with short contour length increments (putative uncoupling) had about the same level of t_{22} survival rates. Although the t_{22} survival rates for "short" and "long" groups could behave totally differently, there were still fewer possibilities for more "long" group events to happen in the low force range. On the contrary, more putative uncoupling events than unfolding events could survive the second ramping and give t_{22} with force below 20 pN after adding ADAMTS13. And this may be the main reason for the increase in t_{22} survival rates with the presence of enzyme. Combined with t_{21} and t_{22} data, there would be a tentative explanation to cover these data. Because F_{21} will not be larger than F_{22} if there is t_{22} surviving the ramping, a low force value for t_{22} will also correspond to a low F_{21} value, regardless of whether there is any t_{21} recording (Figure 7.3 panel B&D). These low forces would facilitate the structural change because time-to-unfold would also be low. In the situation that ADAMTS13 would shorten t_{22} most but not t_{21} under low force, the possible binding of ADAMTS13 on A1A2A3 would facilitate more uncoupling events of the A1 domain from the A2 domain. And this increased possibility for uncoupling events would enhance the t_{22} survival rates in the low force range. These uncoupling events could also accelerate the dissociation of A1 from GPIbα, causing the observed shortening of t_{22}. With the increasing force, fewer uncoupling and more unfolding events happened, causing more ADAMTS13 cleavage events. These cleavage events would shorten t_{22} but not t_{22} survival rates. From this discussion, we hypothesized that A1 would also form catch bonds with the A2 domain, because increasing force would prolong the coupling lifetime and make it harder to uncouple.

Analyzing ADAMTS13 Effects During CR1 Stretching A1A2A3 Tridomain

I. Loading Rates Effects on CR1 Stretching A1A2A3

After using GPIbα to stretch the A1A2A3 molecule, we also tried the CR1-stretch protocol as depicted in Figure 7.1. This protocol has an advantage in controlling the orientation of A1A2A3 molecules. When using direct physical adsorption, we could not guarantee the position of adsorption right at A3 domain. Another complication would be the partial unfolding of the A1 domain when it was adsorbed on the Petri dish and pulled by GPIbα. GPIbα binding to A1 could also be another factor to affect the unfolding of the A2 domain and the subsequent cleavage process. Using anti-6-His mAb eliminated the complication of direct physical adsorption because A1A2A3 would be captured by the antibody, leaving the target molecule suspended with the petri dish surface. The C-terminal of A1A2A3 was engineered to have a His-tag that could be recognized by anti-6-His mAb only. This could also possibly protect the molecule to remain in more intact state for the stretching test because physical adsorption would also "activate" the A1 domain. This tentative activation might have some effects on A1A2 coupling. The other reason for choosing the CR1-stretch protocol is to eliminate the possibility of GPIbα unfolding. By changing to CR1, we would only focus on A1A2A3 catastrophic structural change because anti-6-His and CR1 antibody would be simple enough to serve only as molecular handler. The CR1-stretch experiments were started by using the same loading rate as GPIbα-stretch (200nm/s). Force vs. molecular extension curves for single- and two-force-drop events are shown below in Figure 7.30. Compared with those shown in Figure 7.3, these curves have much flatter slopes thus causing much longer extension in a given force level (average ~70 nm at around 20 pN). The slope is calculated to be around 0.2 pN/nm, which is about only tenth of the GPIbα-stretch case. It is also hard for the CR1-A1A2A3 bond to survive the ramping at higher force level (<30 pN), implying

much weaker bond strength than the GPIbα-A1A2A3. We could still observe two-force-drop events, giving us the hope of continuing to use this protocol. These features resulted from adding the molecule length in the series of molecules: anti-6-His mAb has a similar length as A1A2A3 (~10 nm) and thus would lead to at least double the length of molecules picked up from the Petri dish surface.

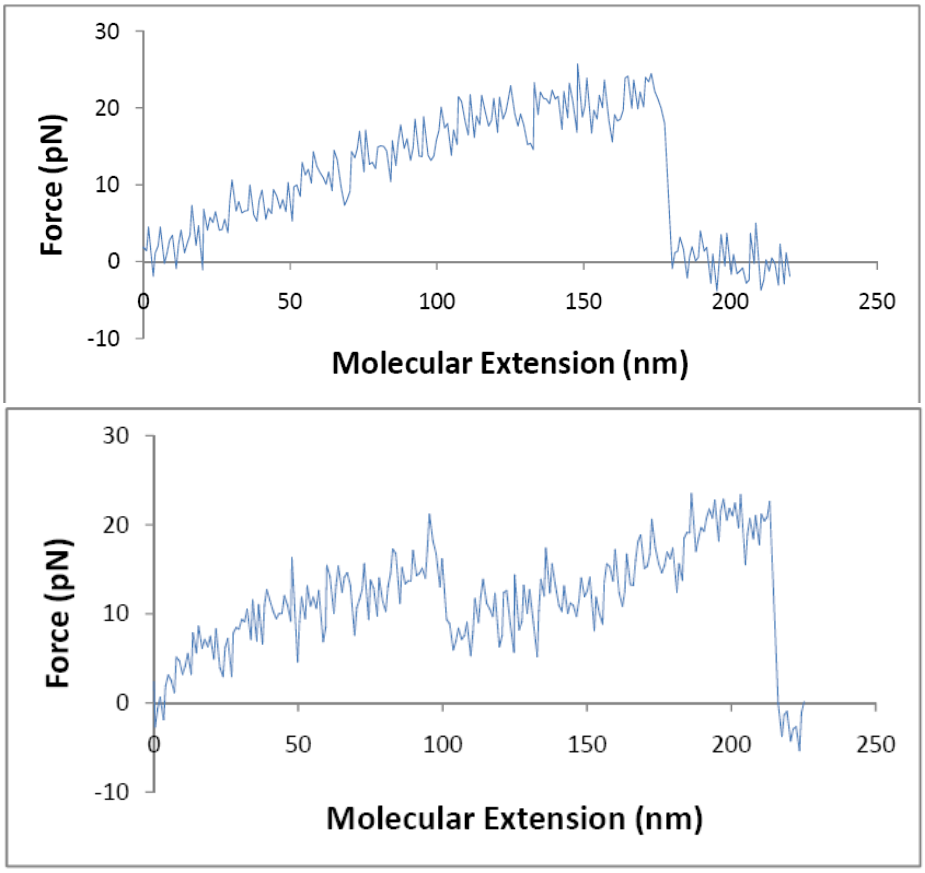

Figure 7.30: Force vs. molecular extension curves for single- and two-force-drop events when anti-6-His captured A1A2A3 was stretched by CR1. Loading rate is 200nm/s, same as GPIbα-stretch protocol. These force scan curves show much flatter slope than GPIbα/A1A2A3 bond.

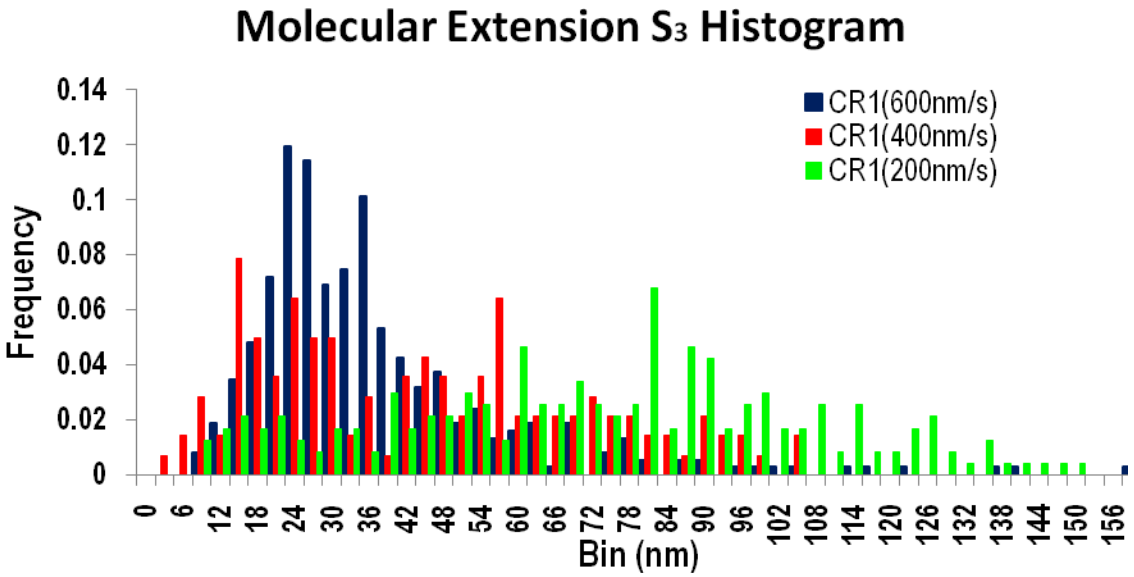

Figure 7.31: Comparison of two-force-drop events S_3 histograms under loading rates of 200 (green bars), 400 (red bars) and 600nm/s (navy bars). All experiments were done by stretching A1A2A3 using CR1 in the absence of ADAMTS13.

To compare with GPIbα-stretch data, we increased the loading speeds from 200nm/s to 400 and 600nm/s, which generated an obvious histogram shift shown in Figure 7.31. The molecular extension values here are S_3, but not those fitted by the WLC model. The loading rate increase from 200nm/s to 400nm/s has a much more obvious effect in this shift than the increase from 400nm/s to 600nm/s. These data suggest that faster loading rates would give less time for the structure to respond to force and less space for conformational rearrangement. To further assess the loading rate effects on lifetime measurement, we compared the scatter plots of t_{11}, t_{21} and t_{22}, which were shown in Figure 7.32 and Figure 7.33. All three measurements showed obvious shifts from 200nm/s to 400nm/s. Consistent with the molecular extension value, changing from 400nm/s to 600nm/s didn't have much effect in these measurements. The shifts of lifetime t_{11}, t_{21} and t_{22} were all towards smaller force and much longer lifetime (upper-left) which was consistent with the previous studies in the Zhu lab.

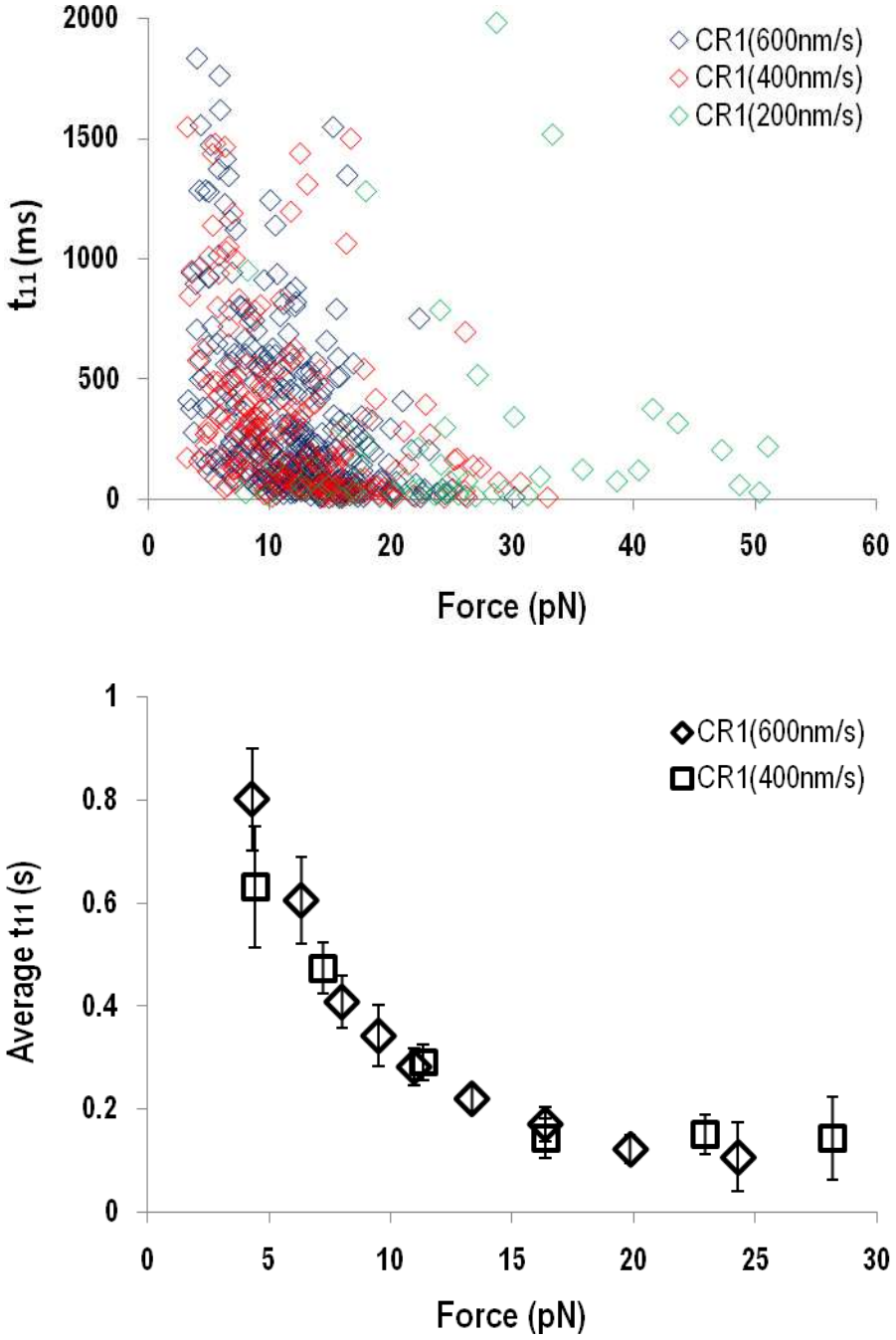

Figure 7.32: Loading rate effects on single-force-drop (single bond) lifetime t_{11} for CR1 stretching A1A2A3 in the absence of ADAMTS13. Upper panel shows t_{11} scatter plots for three loading rates 200 (green), 400 (red) and 600nm/s (navy). Lower panel shows average t_{11} for 400 (square) and 600nm/s (diamond) loading rates.

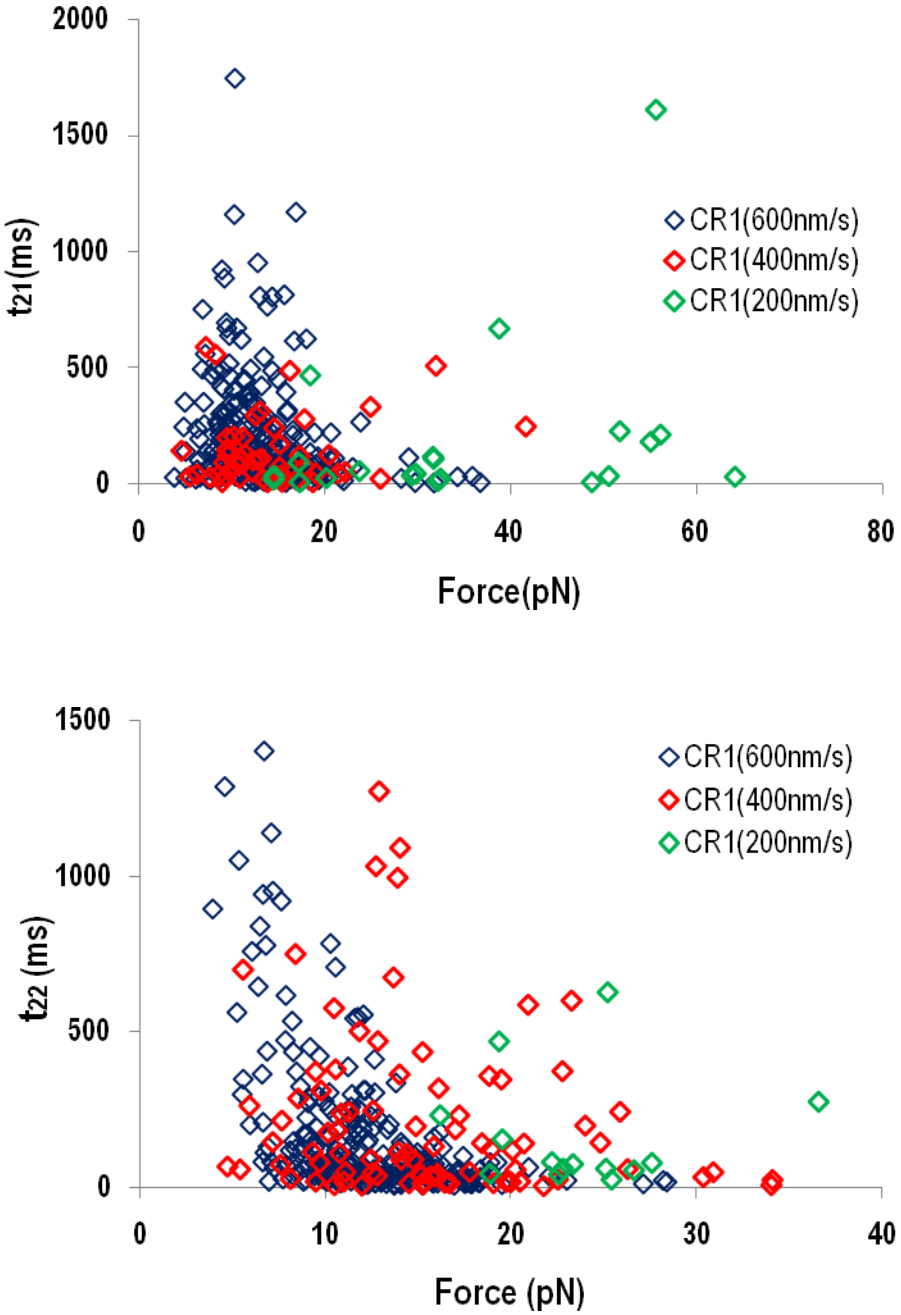

Figure 7.33: Loading rate effects on two-force-drop lifetime t_{21} (upper panel) and t_{22} (lower panel) for CR1 stretching A1A2A3 in the absence of ADAMTS13. Both panels show scatter plots for three loading rates 200 (green), 400 (red) and 600nm/s (navy).

Discussions of The Above Data

The analysis of averaged values of t_{11} shows there were almost no differences between the 400 nm/s and 600 nm/s loading speeds, which confirmed our observation in the scatter plots. t_{11} behaved as a slip bond, which is typical for antigen-antibody interaction (11, 12). One complication of our data is the dissociation of A1A2A3 from its capturing antibody. But this complication would not likely strongly affect the single-force-drop t_{11} quantitatively because it was also an antigen-antibody interaction. Although the data amount for t_{21} and t_{22} were very limited for the 200nm/s loading rate because the bond strength was very weak at that speed, we could still observe the evident population shift towards lower force and higher lifetime value direction. t_{21} showed a clear catch bond shaped distribution for both 400 and 600nm/s loading rates. t_{22} showed a minor distribution shift from 400nm/s to 600nm/s loading speed. This observation is also consistent with previous studies in the Zhu lab, but with a very different loading rate range (Zhu lab unpublished data). Current data suggests that the molecule lifetime population would shift greatly with only a small increase in loading rates from 200nm/s to 400nm/s (or 600nm/s). t_{11} and t_{22}'s quantitative difference in bond behavior imply the strong effects of structural change on CR1-A1A2A3 bond behavior. This impact could come from either the putative A1A2 uncoupling or the putative A2 unfolding. Considering that the only difference between t_{11} and t_{22} involved the loading history, the CR1-A1A2A3 bond had been pre-loaded before giving t_{22} recording. Obviously, this pre-loading history has induced enough structural change in the binding pocket or in its vicinity to change the bond behavior. This reasoning conforms to our previous discussion of the difference between t_{11} and t_{22} for GPIbα-A1A2A3 bonds. Interestingly, comparison of t_{11} and t_{22} at the same loading rate gave the consistent observation that t_{22} was lower on average than t_{11} in the whole force range. Faster loading could result in higher "most probable rupture force", which has been revealed by dynamic force spectroscopy (32, 33). Under the schematic of this discussion, faster stretching by CR1 from 200nm/s to

400nm/s or 600nm/s could also enhance the bond strength at low force regime because CR1-A1A2A3 bond rupture lifetime was much higher.

II. CR1-stretch Induced A1A2A3 Structural Change

Because there was not much difference for t_{11}, t_{21}, and t_{22} between 400nm/s and 600nm/s loading speed, we chose 400 nm/s as the standard loading rate for more experiments to harvest data for all the following analyses. Lower loading speeds were preferred for the AFM system in order to avoid possible hydrodynamic drag and signal delay in the system. As with the analysis we did for GPIbα-stretch protocol, we started by analyzing the contour length increments for CR1-A1A2A3 two-force-drop events. Figure 7.34 shows the histogram of contour length increments from worm-like-chain fitting of each two-force-drop event and its comparison with GPIbα-stretch data. The histogram distribution doesn't have much difference for both, giving a minor shift of the first peak from 15-20nm for GPIbα-stretch to 20-25nm. The position for the second peak was unchanged. This similarity in contour length increment strongly supported our hypothesis for the A1A2A3's catastrophic structural change model, regardless of the stretching protocol used. This similarity also ruled out the possibility for GPIbα unfolding in our previous discussion. The small shift of first peak could result from the interference of additional length of anti-6-His mAb.

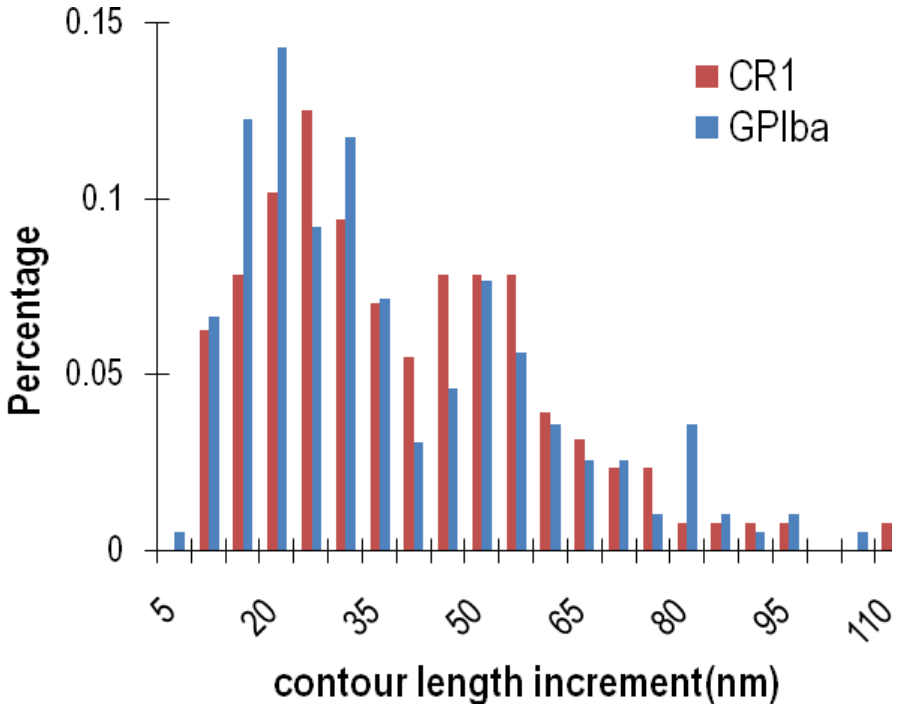

Figure 7.34: Contour length increments histogram of CR1 stretching A1A2A3 (red bars), in comparison with GPIbα-stretch data (blue bars). Contour length increments were obtained from worm-like-chain model fitting of the original two-force-drop events.

Figure 7.35 compares the putative "uncoupling" and "unfolding" force-extension fingerprints with those of GPIbα-stretch data. Force-extension curves were chosen from the same bin of contour length increments fitted by WLC model, and they were from the same bar of the histogram shown in Figure 7.34. We still chose 15-20nm and 45-50nm contour length increments values for comparison. And they showed patterns with strong similarity to the GPIbα data. One observation is that CR1's fingerprint for 15-20nm extension gave a much lower peak force at the first force drop than the GPIbα data. However, the second peak force was comparable to that of GPIbα. So the antibody capturing affected the A1A2A3 structure's ability to resist the first force drop for the first type of structural change ("uncoupling"). The second type of structural change

("unfolding") gave a similarity in not only the pattern but also the first peak force value. The second peak force was lower for CR1 data than GPIbα.

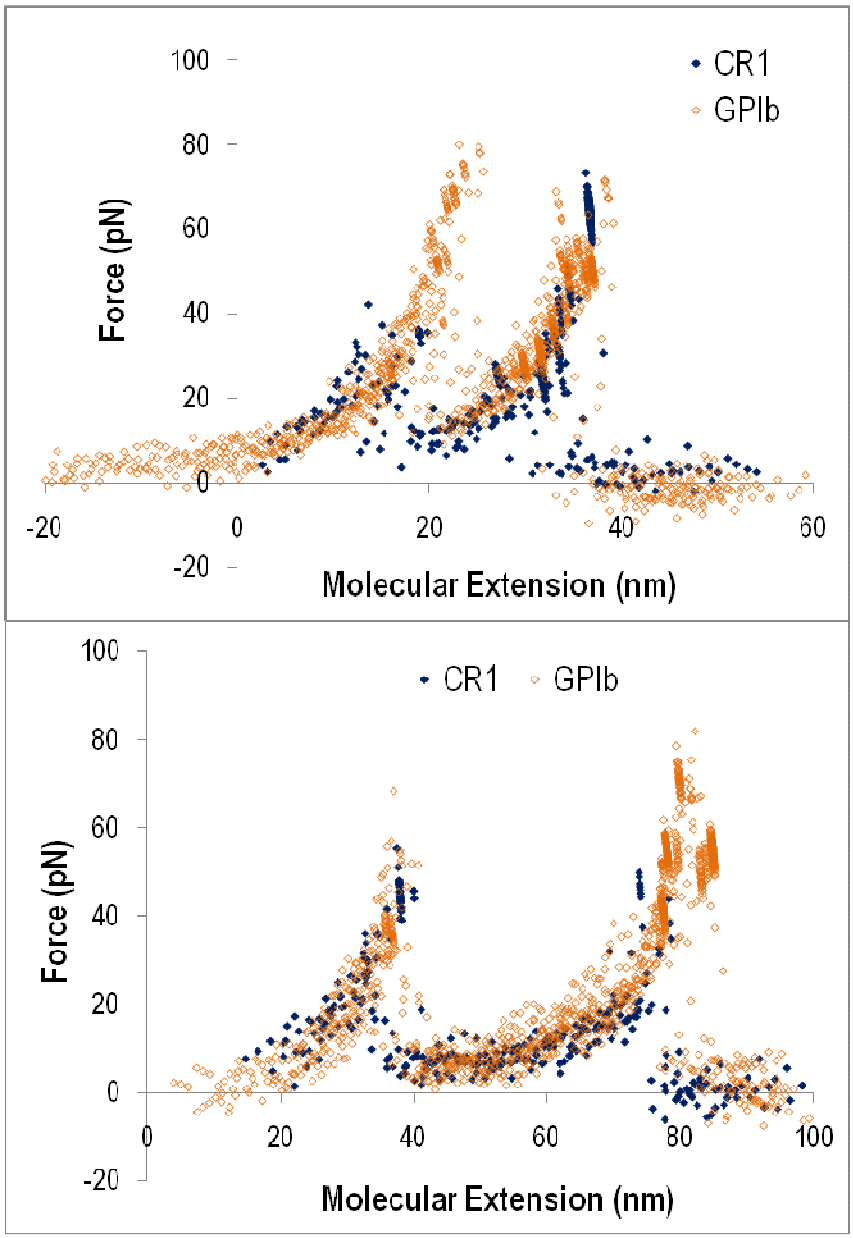

Figure 7.35: Comparison of CR1 "uncoupling" and "unfolding" force-extension fingerprints (navy dots) with GPIbα-stretch data (yellow dots).

III. ADAMTS13 Effects on CR1 Stretching A1A2A3 Tridomain

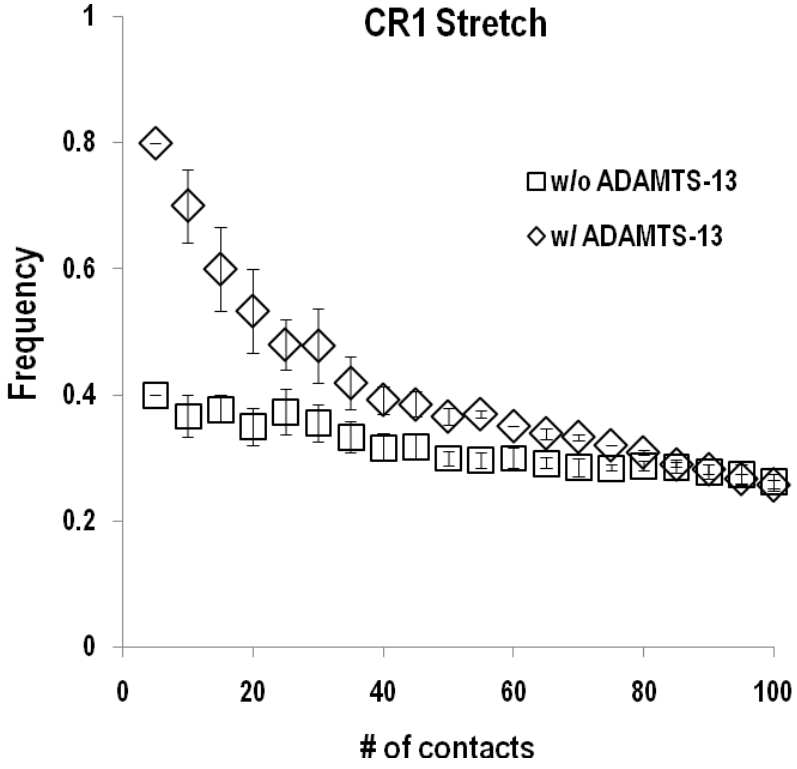

Figure 7.36: Running frequency of CR1 binding to (stretching) A1A2A3, in the absence (square) and presence (diamond) of ADAMTS13. Error bars are standard error of the Binomial distribution.

Similar to the analysis for GPIbα-stretch data, we analyzed the running binding frequency, t_{22} survival rate, average t_{22}, transition time and rupture time for short and long contour length increment groups and the ADAMTS13 effects on these measurements. Figure 7.36 shows a typical experimental observation of running binding frequency. Similar to the GPIbα data, there was a slow and steady decrease in the binding frequency for more contacts between CR1 coated AFM tip and petri dish coated with anti-6-His captured A1A2A3. After adding ADAMTS13 in the buffer, an experiment with the same level of total binding frequency as before (~25%) would have much higher initial binding frequency, exhibiting a fast decrease in the binding frequency with more

contacts. This behavior illustrated the effects of ADAMTS13 in quickly decreasing the binding frequency by possible cleavage.

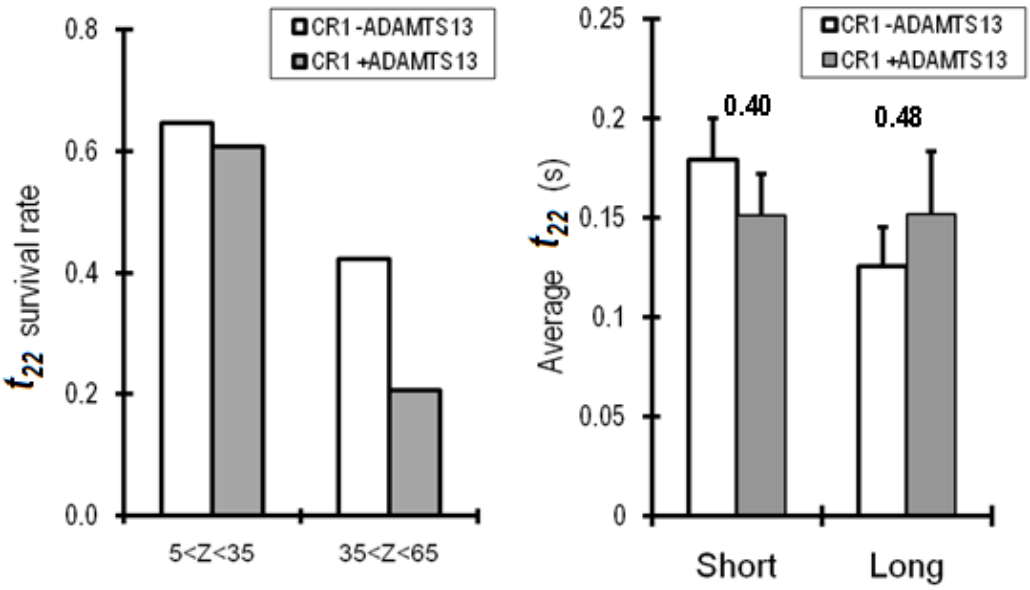

Figure 7.37: t_{22} survival rates (left panel) and average t_{22} (right panel) comparison of short and long contour length increment groups, with the absence (open bars) and presence (grey bars) of ADAMTS13. Number labeled are p-value of paired t-test.

Figure 7.37 shows the t_{22} survival rate and the average t_{22} results for both conditions with the absence and presence of ADAMTS13. For the "short" contour length increment group, there were no significant differences between the two conditions, while there were significant differences for the "long" group. With the putative unfolding events, the t_{22} survival percentage had decreased by more than half after the addition of ADAMTS13. Interestingly, like the putative uncoupling events, the decrease in t_{22} survival rates had not affected the average t_{22} value for the putative unfolding events. Therefore, the possibilities would be that the decrease in survival rates resulted from the accelerated dissociation or that cleavage occurred during the ramping phase instead of the bond lifetime recording phase.

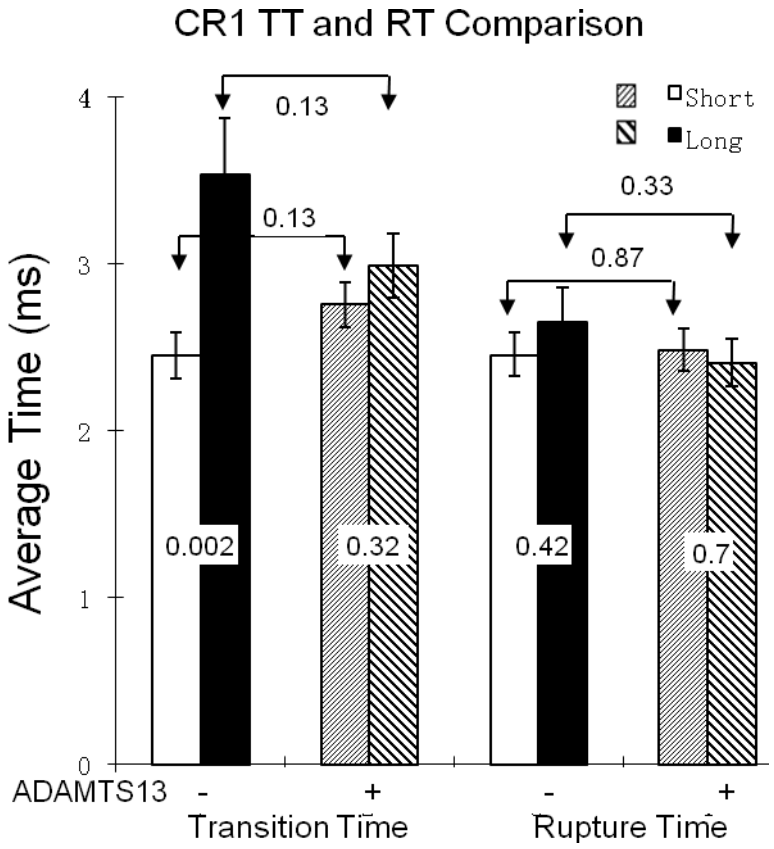

Figure 7.38: Transition time (1st and 2nd pairs from left) and rupture time (3rd and 4th pairs from left) comparison for putative "uncoupling" (or short) and putative "unfolding" (or long) groups in the absence and presence of ADAMTS13. 1st and 3rd pairs are in the absence of ADAMTS13; 2nd and 4th pairs are in the presence of ADAMTS13. Numbers labeled are p-value of each paired t-test.

Figure 7.38 shows the analysis for transition time and rupture time of CR1 stretching A1A2A3 two-force-drop events in the absence and presence of ADAMTS13. In the eight paired t-test, there is only one pair showing significant difference with 0.002 p-value, which is transition time comparison between short (putative "uncoupling") and long (putative "unfolding") groups. Data shows the "unfolding" events have significantly longer transition time and more "uncoupling" events. This difference was abolished by adding ADAMTS13 in the system. GPIbα-stretch data shows "uncoupling" events have longer transition time than "unfolding" events (Figure 7.16), which is the reverse of CR1-stretch data. The differences in the transition time and rupture time for GPIbα-stretch and

CR1-stretch protocols indicate that the duration of instantaneous structural transition of A1A2A3 could be affected by the ligand that binds to and stretches it.

IV. ADAMTS13 Effects on one-force-drop events t_{11}, two-force-drop events t_{21} and t_{22}

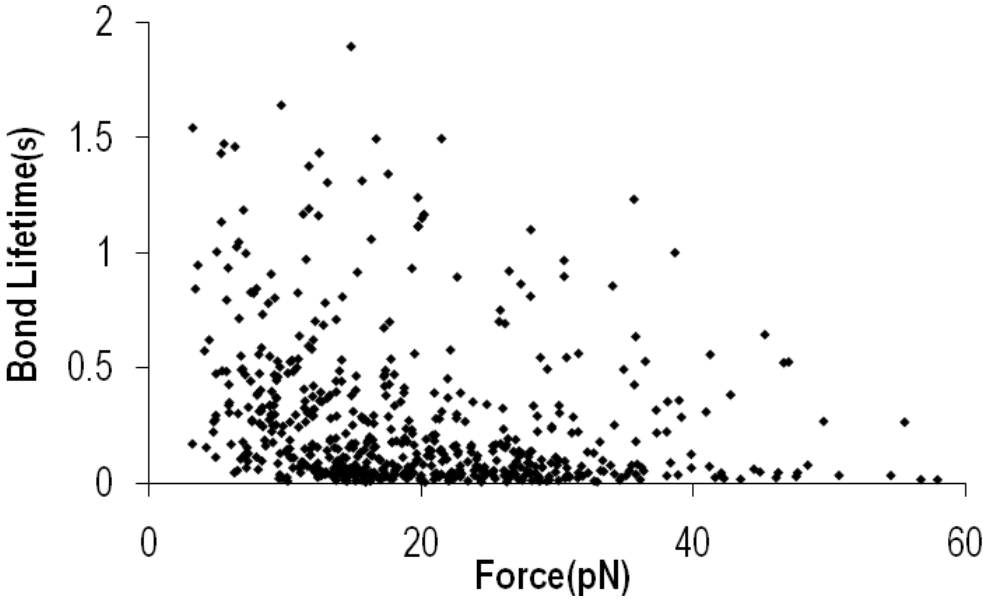

Figure 7.39: Scatter plot of 593 single-force-drop lifetime t_{11} of CR1-A1A2A3 bond. All experiments were done in the absence of ADAMTS13. Loading rate was 400nm/s.

To further elucidate the force regulation on the binding kinetics of CR1-A1A2A3 bond based on one-force-drop and two-force-drop analysis when in the absence/presence of ADAMTS13, we continued analyzing the force dependence of the t_{11}, t_{21}, t_{22}, t_{22} survival rates, and molecular extension S_3. Figure 7.39 shows the scatter plot of t_{11} distribution on the range force in the absence of ADAMTS13 and Figure 7.40 shows the averaged t_{11} from scatter plots and the comparison for with and without adding ADAMTS13.

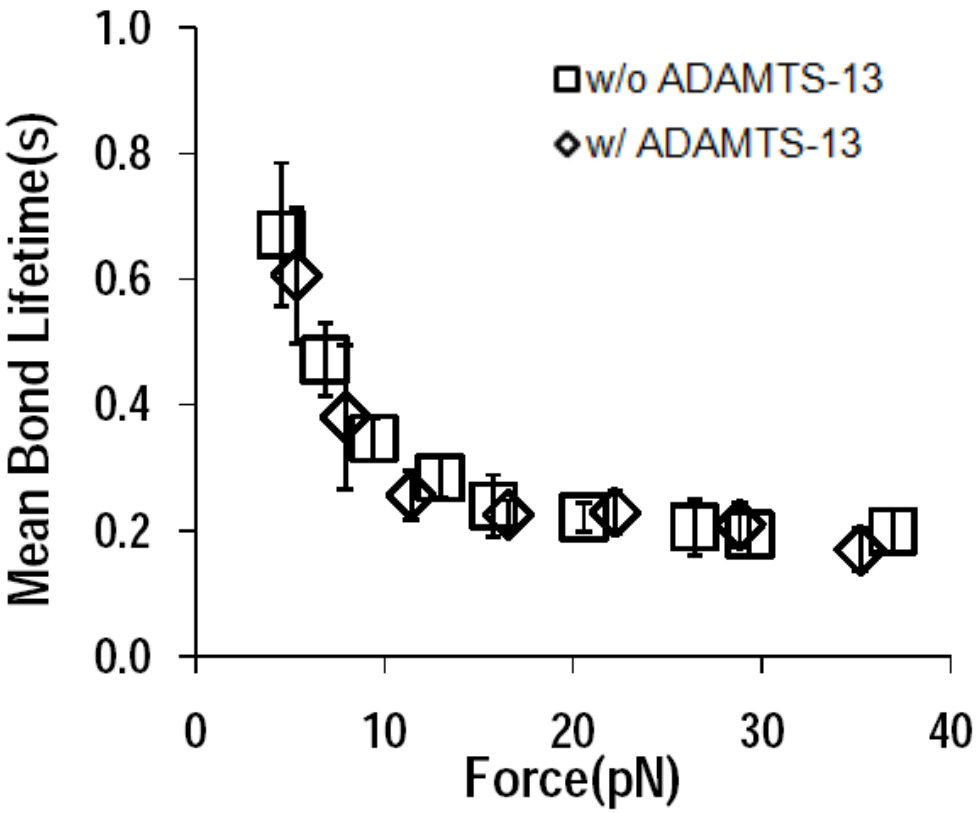

Figure 7.40: Average single-force-drop lifetime (time-to-rupture) t_{11} in the absence (square) and presence (diamond) of ADAMTS13.

Compared with the t_{11} measurements of GPIbα-stretch protocol, CR1-A1A2A3 bonds gave lifetime measurements in a much smaller force range. The more compact data in the less than 40pN range exhibited a clear trend of slip bonds, which was typical of antigen-antibody interaction. Adding ADAMTS13 did not change the bond behavior either qualitatively or quantitatively. This was consistent with the observation from the GPIbα-stretch protocol. Because of the limited supply of CR1 antibody, we have not done the EDTA control as for GPIbα-stretch. And as discussed previously, we used 400nm/s loading rate for all these lifetime experiments.

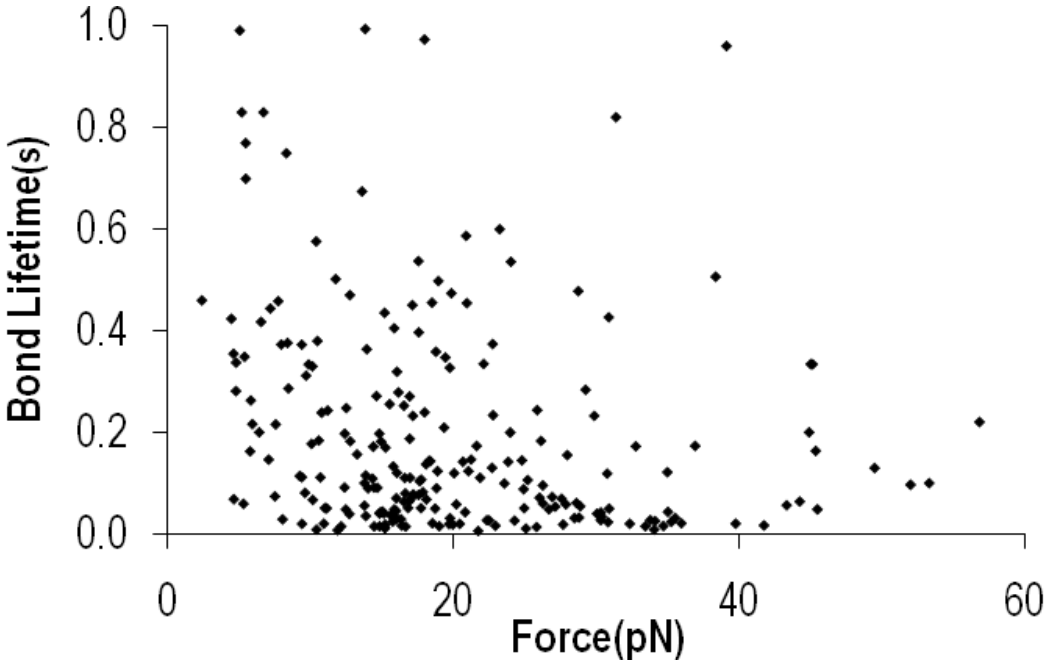

Figure 7.41: Scatter plot of 229 two-force-drop time-to-rupture t_{22} measurements for CR1-A1A2A3 in the absence of ADAMTS13. One second cutoff line was set for filtering outliers.

Figure 7.41 shows the scatter plots of two-force-drop t_{22} in the absence of ADAMTS13 and Figure 7.42 shows the comparison of force drop results before and after adding the enzyme. In the absence of ADAMTS13, t_{22} also showed a clear trend of slip bonds, which kept the feature of CR1-A1A2A3 bond but with quantitative differences. The difference implied the effects of catastrophic structural change. In sharp contrast to the t_{11} data, adding ADAMTS13 shortened the t_{22} value to only about one third of its original level and the curve of exponential decay became a flattened line, indicating insensitivity to force. The maximum shortening happened at the minimum force level, and this shortening decreased with increasing force until reaching near-zero difference at around 15pN. To further quantify this t_{22} shortening effect versus force, we did the analysis for averaged t_{22} again for a set force bin size, and we calculated the off-rate increase versus force as shown in Figure 7.43.

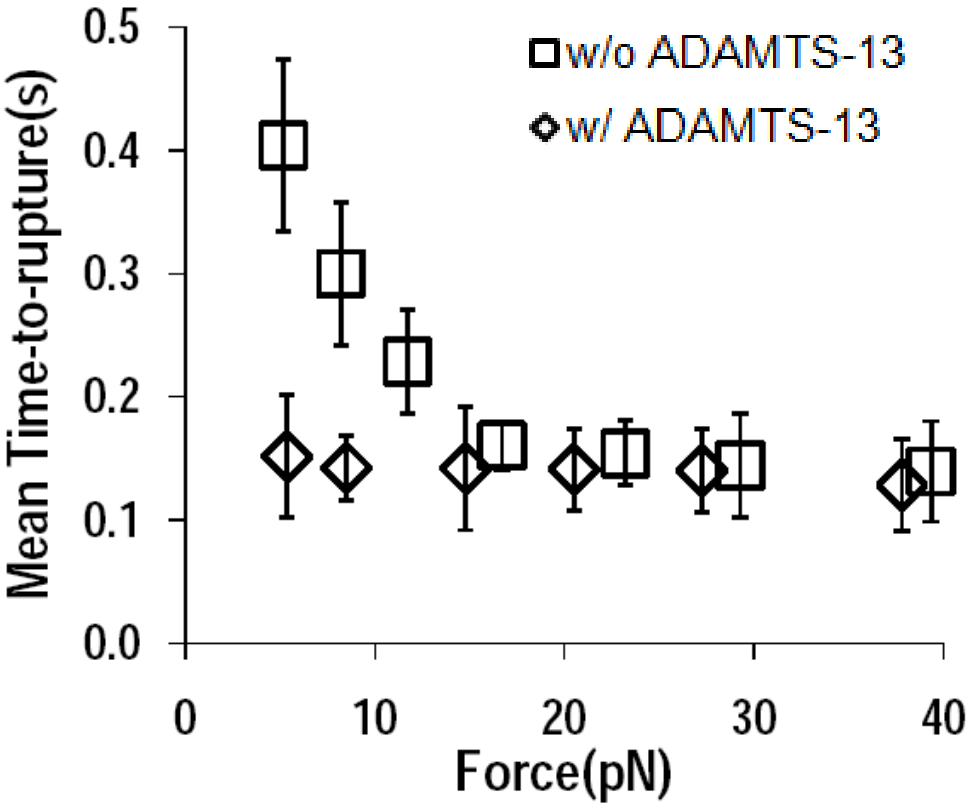

Figure 7.42: Average two-force-drop t_{22} for CR1 stretching A1A2A3 in the absence (square) and presence (diamond) of ADAMTS13. Error bars are standard errors of the mean.

Figure 7.43 shows the averaged lifetime analysis from 10pN force bin interval, and each data point was calculated at a 4pN increment from 2pN to 26pN. The ΔK_{off} value decreased from ~4.2/s at 2pN to near zero at 26pN, confirming our observation from the mean t_{22} data. The decrease of off-rate also had very similar trend as the GPIbα-stretch data but at a much faster rate to reach near zero at a smaller force range. This similarity in the off-rate decrease dependence on force confirmed this unusual observation and also strongly implied the effects of ADAMTS13 on A1A2A3 regardless of the stretching methods used.

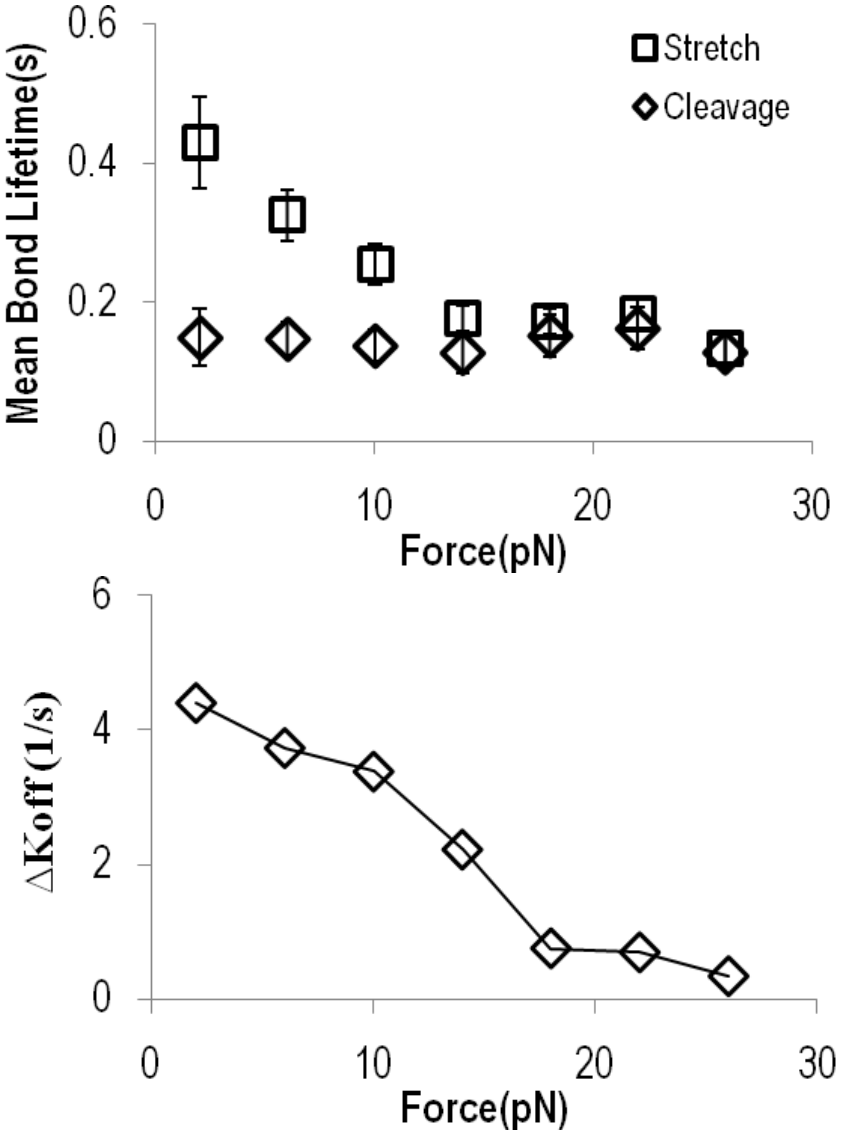

Figure 7.43: Comparison of averaged t_{22} vs. force based on same bin size (10pN) analysis (upper panel) for the data of in the absence (square) and presence (diamond) of ADAMTS13. Lower panel shows off-rate difference vs. force calculated from the reciprocal of averaged t_{22}.

As discussed previously, the stretching force on A1A2A3 might have negative effects in facilitating the cleavage favored conformation of the cleavage site in the A2 domain after catastrophic structural change. It was confirmed from repeated observations that higher stretching force on A1A2A3 resulted in smaller ΔK_{off} regardless of the stretching protocol before and after adding ADAMTS13. There might be differences

between the initial conformations of A1A2A3 because of different immobilization methods. But these possible conformation differences had not changed the effects of force in regulating ADAMTS13's effects of changing the binding kinetics. At low stretching force levels, the possible binding of ADAMTS13 on A1A2A3 might show that it is easier to cut the Tyr1605-Met1606 bond or to accelerate the dissociation of CR1-A1A2A3 bond. Also because of the longer t_{22} at low force level, the effects from the enzyme could easily be observed. At higher force levels, t_{22} might have already been too short for ADAMTS13 to function, either from cleavage or from accelerated dissociation of CR1 from A1A2A3. Comparing Figures 7.20 and 7-43, with adding ADAMTS13 in the system, we found the lowest t_{22} values at maximal force level (~80pN and ~30pN for GPIbα and CR1-stretch, respectively) for both stretching protocols were very similar, giving ~0.15 second value. For GPIbα-stretch, t_{22} was brought down from ~0.2 second. For CR1-stretch, t_{22} was already down to this level from the exponential decay. This similarity implied that 0.15 seconds might be the t_{22} threshold for observing the cleavage effect at large force. At the low force end, the even lower t_{22} value for GPIbα-stretch data might be the result of accelerated dissociation, as discussed previously.

After analyzing the ADAMTS13 effects on time-to-rupture t_{22}, we continue analyzing whether the time-to-unfold t_{21} has also been affected. Figure 7.44 shows a catch-slip transitional bond behavior for t_{21}, which is consistent with GPIbα data.

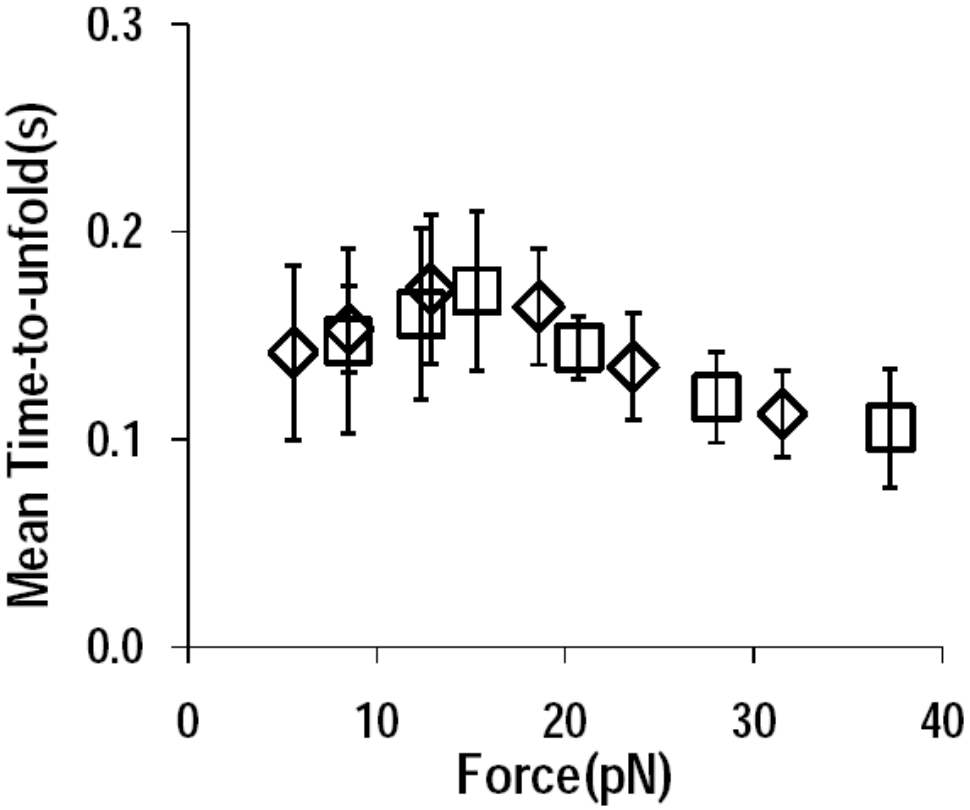

Figure 7.44: Average two-force-drop events time-to-unfold t_{21} in the absence (square) and presence (diamond) of ADAMTS13 for CR1 stretching A1A2A3.

Discussion of The Above Data

This interesting finding that the t_{21} catch-slip transitional bond remained unchanged for different immobilization and stretching protocols implied that the ability for A1A2A3 to resist the catastrophic structural change had not changed qualitatively because of protocols. This finding also confirmed our observation for GPIbα-stretch t_{21}. The quantitative difference of t_{21} between GPIbα and CR1-stretch could come from three causes. First, the loading speed for CR1-stretch was 400nm/s while GPIbα-stretch was 200nm/s. The faster loading rate could result in a quantitative shift of time-to-unfold. Second, different conformations of the A1A2A3 molecule because of different immobilization methods could cause the value difference. Third, different stretching positions because of different binding pockets on A1 for GPIbα and CR1 could result in

the t_{21} value difference. The conformation and binding pocket difference of A1A2A3 could affect the way force was propagated through the A1A2A3 molecule to affect the strength of uncoupling or unfolding. For the uncoupling pathway, the above effects could be more obvious than the unfolding pathway, because the possible A1A2 coupling interface is located closer to the pulling site. The immobilization and stretching position difference could have less direct impact on the unfolding pathway because A1A2 coupling might provide some shielding effect for the unfolding core. ADAMTS13 also had no effects in t_{21} for CR1-stretch protocol, implying the necessity of structural change before observing ADAMTS13's effect. The possible binding of ADAMTS13 to A1A2A3 seemed to have negligible effects on the catastrophic structural change t_{21}. Most likely, both the uncoupling pathway and the unfolding pathway would not be affected.

V. ADAMTS13 Effects on Force Regulated S_3 and t_{22} Survival Rate

To further dissect ADAMTS13 effects with two-force-drop observation, we analyzed the histogram and force dependence of molecular extension S_3 as shown in Figure 7.45. The upper panel shows the shift of S_3 from longer extension to shorter ones after adding ADAMTS13. The lower panel shows an obvious extension increase at force range 10-20pN. This extension increase could result from more unfolding events happening at larger force level. The extension increase was totally abolished by adding ADAMTS13, indicating the possible cleavage at A2 domain in the presence of ADAMTS13.

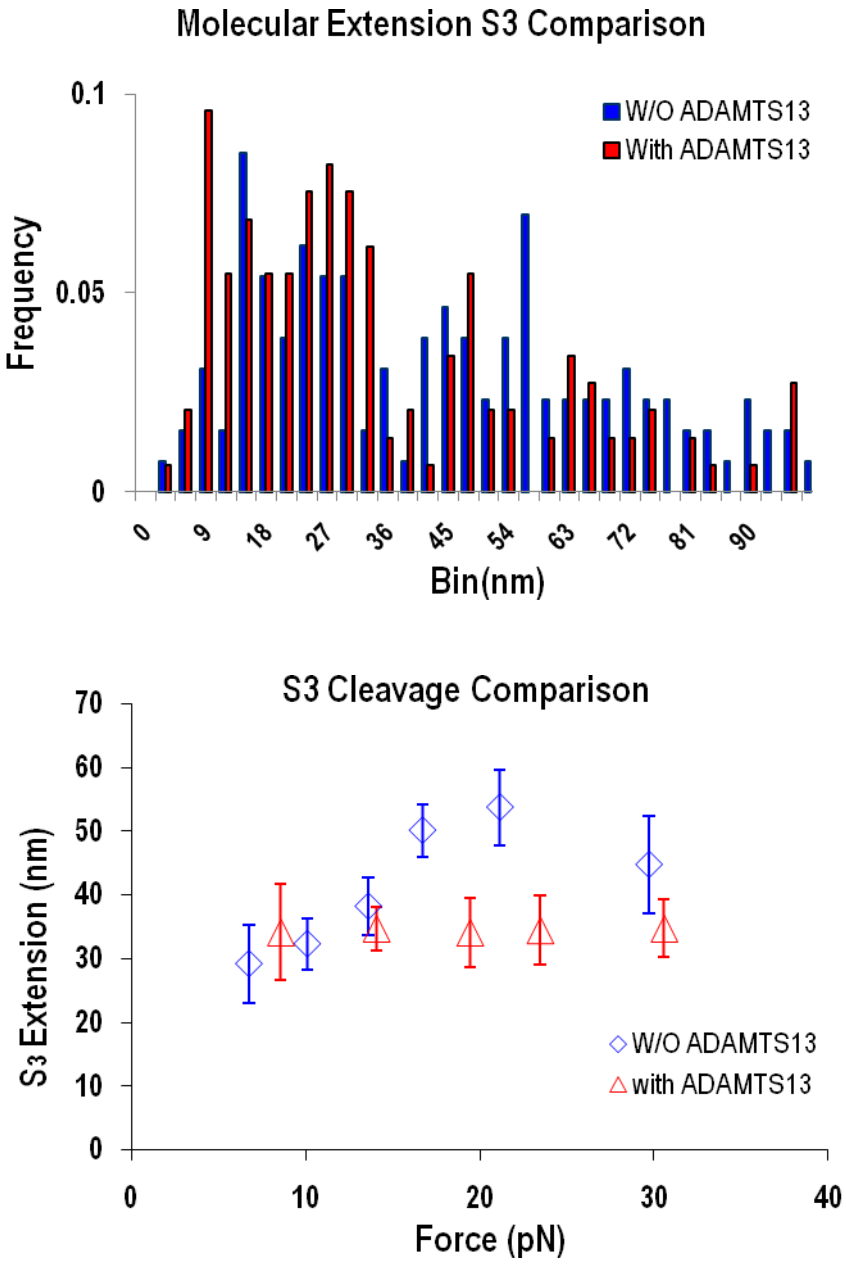

Figure 7.45: Histogram (upper panel) and force dependence (lower panel) of molecular extension S_3 in the absence (blue bars and diamond) and presence (red bars and diamonds) of ADAMTS13. All experiments were done by using 400nm/s loading rate to stretch A1A2A3 molecule.

Combined with t_{22} and ΔK_{off} data, low force test observations indicated more shortening of t_{22} and higher ΔK_{off}, but minimal extension S_3 shortening; large force

induced minimal t_{22} shortening (near zero) but maximal shortening of extension S_3. These observations implied that ADAMTS13 affected t_{22} duration but not the first force drop phase or the second ramping phase at low force. It is still not clear what percentage of t_{22} events are impacted here. At larger force, ADAMTS13 would mainly target the ramping phase instead of the t_{22} recording phase. Therefore, t_{22} remained almost untouched, but the extension S_3 had been shortened greatly. The reason why ADAMTS13 had this preference change for targeting at different force levels could be several fold. The first possibility would be the t_{22} percentage change: fewer t_{22} events at higher force level would result in fewer t_{22} shortening effects, but much more extension shortening effects would be observed. The second explanation could be in the time requirement for ADAMTS13 to function: if ADAMTS13 needed certain time duration to function, then the time before t_{22} triggering at low force would not be enough for the enzyme. At higher force levels, F_{22} was set to be much higher, so the ramping needed longer time, causing a longer extension S_3 to reach the preset force and trigger the lifetime recording. The longer second ramping phase provided enough time for ADAMTS13 to function. For the second explanation, we do not have data to support it. However, for the first one, we quantified the t_{22} survival rate vs. force to support it.

Figure 7.46 shows a clear decrease of t_{22} percentage with increasing force at 600nm/s loading rate (green diamonds). The t_{22} survival rate was 100% at about 5pN and decreased to about 50% at 25pN. This decrease was in accordance with the bond lifetime t_{22} decrease with larger force, indicating the weakening of bond strength. Yellow diamonds are data from 200nm/s loading rates. As discussed previously, increasing loading rates would affect bond behavior quantitatively as the lifetime value shifted towards smaller force. This force history effect created a sharp contrast between 200nm/s and 600nm/s stretching speeds. Because of the limited data amount, we have not got the averaged t_{22} curve at 200nm/s loading rate yet. But the t_{22} survival rates suggest a catch-bond-like behavior. It is still unclear yet whether this survival rates increase came from

the bond strength increase. It would be interesting to make more measurements at 200nm/s loading speed and confirm this possible catch bond. Slower pulling could result in more opportunities for new hydrogen bond formation along the sliding-rebinding interface.

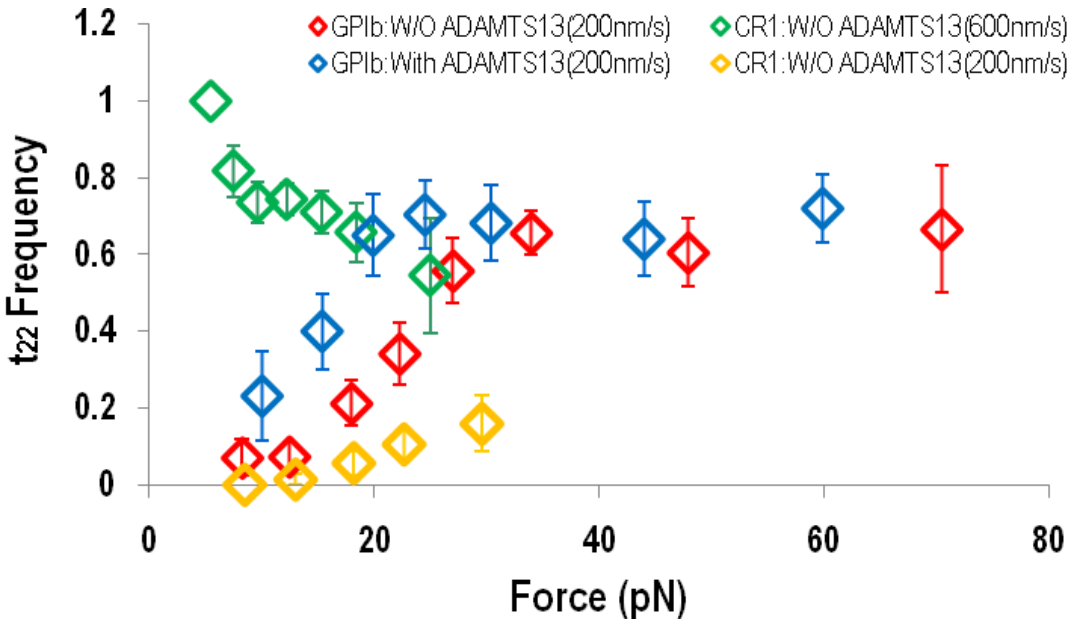

Figure 7.46: Two-force-drop t_{22} survival rate vs. force for 200nm/s (yellow) and 600nm/s (green) loading rate of CR1-stretch. GPIbα-stretch data (200nm/s loading rate) in the absence (red) and presence (blue) of ADAMTS13 was for comparison.

The above observation confirmed our hypothesis for the maximal t_{22} change at the lowest force. Because the preset clamping force was low, almost all the two-force-drop events could give t_{22} recording. Consequently, the effects of ADAMTS13 would almost solely contribute to t_{22} shortening. With increasing force, the percentage of t_{22} events decreased, thus increasing the percentage of two-force-drop events which had not survived the ramping. t_{22} shortening effects also decreased with larger force, suggesting that the effects of ADAMTS13, if any, would target mostly on the ramping phase from either cleavage or accelerated dissociation. Recollecting the t_{22} shortening vs. force data for GPIbα-stretch, the effect of ADAMTS13 on t_{22} was maximal at low force even though t_{22} was minimal under softest stretching. Furthermore, the t_{22} percentage was also

the lowest at minimal force value (Figure 7.46 red diamond). Combining this with the observation that extension S_3 was minimal at low force, we could draw the conclusion that the ADAMTS13 still mainly targeted at t_{22} even though there were fewer t_{22} events than in the CR1-stretch case.

Therefore, the ADAMTS13 effects shared most similarities on t_{11}, t_{21}, t_{22}, ΔK_{off}, S_3, for GPIbα and CR1-stretch protocol. And the most differences came from t_{11} and t_{22} behavior and the t_{22} survival rates for both pulling methods. These similarities may come from the specific requirement for ADAMTS13 to take effects, and the differences may come from different bond behavior obtained by using different binding counterparts for A1A2A3. Nevertheless, all these similarities and differences complemented the whole observation and provided us more details about the function of ADAMTS13.

BIBLIOGRAPHY

[1] McEver, R.P. 2001. Selectins from Cell Adhesion, Chapter 2, ed. by Mary C. Beckerle. *Oxford University Press*:30-61.

[2] Springer, T.A. 1990. Adhesion receptors of the immune system. *Nature* **346**:425-434.

[3] McEver, R.P., and R.D. Cummings. 1997. Role of PSGL-1 binding to selectins in leukocyte recruitment. *J Clin Invest* **100**:485-492.

[4] McEver, R.P. 1994. Selectins. *Curr. Opin. Immunology* **6**:75-84.

[5] McEver, R.P. 2002. Selectins: lectins that initiate cell adhesion under flow. . *Curr Opin Cell Biol* **14**:581-586.

[6] Konstantopoulos, K., Kukreti S., McIntire L. V. 1998. Biomechanics of cell interactions in shear fields. *Advanced Drug Delivery Reviews* 33:141-164.

[7] Savage, B., E. Saldívar, and Z.M. Ruggeri. 1996. Initiation of platelet adhesion by arrest onto fibrinogen or translocation on von Willebrand factor. *Cell* **84**:289-297.

[8] Dong, J.F. 2005. Cleavage of ultra-large von Willebrand factor by ADAMTS-13 under flow conditions. *J Thromb Haemost* 3:1710-1716.

[9] Dong, J.F., J. L. Moake, L. Nolasco, A. Bernardo, W. Arceneaux, C. N. Shrimpton, A. J. Schade, L. V. McIntire, K. Fujikawa, and J. A. Lopez. 2002. ADAMTS-13 rapidly cleaves newly secreted ultralarge von Willebrand factor multimers on the endothelial surface under flowing conditions. *Blood* 100:4033-4039.

[10] Liu, L., H. Choi, A. Bernardo, A. L. Bergeron, L. Nolasco, C. Ruan, J. L. Moake, and J. F. Dong. 2005. Platelet-derived VWF-cleaving metalloprotease ADAMTS-13. *J Thromb Haemost.* 3:2536-2544.

[11] Marshall, B.T., M. Long, J.W. Piper, T. Yago, R.P. McEver, and C. Zhu. 2003. Direct observation of catch bonds involving cell-adhesion molecules. . *Nature* **423**:190-193.

[12] Sarangapani, K.K., T. Yago, A.G. Klopocki, M.B. Lawrence, C.B. Fieger, S.D. Rosen, R.P. McEver, and C. Zhu. 2004. Low force decelerates L-selectin dissociation from P-selectin glycoprotein ligand-1 and endoglycan. *J Biol Chem* **279**:2291-2298.

[13] Marshall, B.T., K. K. Sarangapani, J. Wu, M. B. Lawrence, R. P. McEver, and C. Zhu. 2006. Measuring molecular elasticity by atomic force microscope cantilever fluctuations. *Biophys J* 90:681-692.

[14] Yago, T., A. Leppanen, H. Qiu, W.D. Marcus, M.U. Nollert, C. Zhu, R.D. Cummings, and R.P. McEver. 2002. Distinct molecular and cellular contributions to stabilizing selectin-mediated rolling under flow. *J Cell Biol* **158**:787-799.

[15] Yago, T., J. Wu, C.D. Wey, A.G. Klopocki, C. Zhu, and R.P. McEver. 2004. Catch bonds govern adhesion through L-selectin at threshold shear. *J Cell Biol* **166**:913-923.

[16] Vestweber, D., and J. E. Blanks. 1999. Mechanisms that regulate the function of the selectins and their ligands. *Physiol Rev* **79**:181-213.

[17] Bell, G.I. 1978. Models for the specific adhesion of cells to cells: A theoretical framework for adhesion mediated by reversible bonds between cell surface molecules. *Science* **200**.

[18] Dembo, M., D.C. Torney, K. Saxman, and D. Hammer. 1988. The reaction-limited kinetics of membrane-to-surface adhesion and detachment. *Proc R Soc Lond B Biol Sci* **234**:55-83.

[19] Evans, E., and K. Ritchie. 1997. Dynamic strength of molecular adhesion bonds. *Biophys J* **72**:1541-1555.

[20] Marshall, B.T., Sarangapani K. K., Lou J., McEver R.P. and Zhu C. 2005. Force history dependence of receptor-ligand dissociation. *Biophys J* 88:1458-1466.

[21] Alon, R., D.A. Hammer, and T.A. Springer. 1995. Lifetime of the P-selectin: carbohydrate bond and its response to tensile force in hydrodynamic flow. *Nature* **374**:539-542.

[22] Alon, R., S.Q. Chen, K.D. Puri, E.B. Finger, and T.A. Springer. 1997. The kinetics of L-selectin tethers and the mechanics of selectin-mediated rolling. *J Cell Biol* **138**:1169-1180.

[23] Alon, R., S. Chen, R. Fuhlbrigge, K. D. Puri, and T. A. Springer. 1998. The kinetics and shear threshold of transient and rolling interactions of L-selectin with its ligand on leukocytes. *Proc Natl Acad Sci USA* **95**:11631-11636.

[24] Ramachandran, V., M. U. Nollert, H. Qiu, W. J. Liu, R. D. Cummings, C. Zhu, and R. P. McEver. 1999. Tyrosine replacement in P-selectin glycoprotein ligand-1 affects distinct kinetic and mechanical properties of bonds with P- and L- selectin. *Proc Natl Acad Sci USA* **96**:13771- 13776.

[25] Ramachandran, V., T. Yago, T.K. Epperson, M.M.A. Kobzdej, M.U. Nollert, R.D. Cummings, C. Zhu, and R.P. McEver. 2001. Dimerization of a selectin and its ligand stabilizes cell rolling and enhances tether strength in shear flow. *Proc Natl Acad Sci USA* **98**:10166-10171.

[26] Chen, S., and T. A. Springer. 2001. Selectin receptor-ligand bonds: Formation limited by shear rate and dissociation governed by the Bell model. *Proc Natl Acad Sci USA* **98**:950-955.

[27] Dwir, O., G.S. Kansas, and R. Alon. 2001. Cytoplasmic anchorage of L-selectin controls leukocyte capture and rolling by increasing the mechanical stability of the selectin tether. *J Cell Biol* **155**:145-156.

[28] Klopocki, A.G., Yago T., Mehta P., Yang J., Wu T., Leppanen A., Bovin N. V., Cummings R. D., Zhu C., and McEver R. P. 2008. Replacing a lectin-domain residue in L-selectin enhances binding to P-selectin Glycoprotein ligand-1 but not to 6-sulfo-sialyl Lewis X. *J Biol Chem* 283:11493-11500.

[29] Yago, T., Lou J., Wu T., Yang J., Miner J. J., Coburn L., Lopez J. A., Cruz M. A., Dong J., McIntire L. V., McEver R. P., and Zhu C. 2008. Platelet glycoprotein Ib〈 forms catch bonds with human WT vWF but not with type 2B von Willebrand disease vWF. *J Clin Invest In press*.

[30] Lou, J., Yago T., Klopocki A. G., Metha P., Chen W., Zarnitsyna V. I., Bovin N. V.,Zhu C., and McEver R. P. 2006. Flow-enhanced adhesion regulated by a selectin interdomain hinge. *J Cell Biol* 174:1107-1117.

[31] Merkel, R., P. Nassoy, A. Leung, K. Ritchie, and E. Evans. 1999. Energy landscapes of receptor-ligand bonds explored with dynamic force spectroscopy. *Nature* **397**:50-53.

[32] Evans, E., A. Leung, D. Hammer, and S. Simon. 2001. Chemically distinct transition states govern rapid dissociation of single L-selectin bonds under force. *Proc Natl Acad Sci USA* **98**:3784-3789.

[33] Evans, E., A. Leung, V. Heinrich, and C. Zhu. 2004. Mechanical switching and coupling between two dissociation pathways in a P-selectin adhesion bond. *Proc Natl Acad Sci USA* **101**:11281-11286.

[34] Sassetti, C., Van Zante, A., and Rosen, S. D. 2000. Identification of endoglycan, a member of the CD34/Podocalyxin family of sialomucins. *J Biol Chem* **275**:9001-9010.

[35] Fieger, C.B., Sassetti, C. M., and Rosen, S. D. 2003. Endoglycan, a member of the CD34 family, functions as an L-selectin ligand through modification with tyrosine sulfation and sialyl lewis x. *J Biol Chem* **278**:27390-27398.

[36] Finger, E.B., K.D. Puri, R. Alon, M.B. Lawrence, U.H. Von Andrian, and T.A. Springer. 1996. Adhesion through L-selectin requires a threshold hydrodynamic shear. *Nature* **379**:266-269.

[37] Lawrence, M.B., G.S. Kansas, E.J. Kunkel, and K. Ley. 1997. Threshold levels of fluid shear promote leukocyte adhesion through selectins (CD62L,P,E). *J Cell Biol* **136**:717-727.

[38] Doggett, T.A., G. Giridhar, A. Lawshe, J. L. Miller, I. J. Laurenzi, S. L. Diamond, T. G. Diacovo. 2003. Alterations in the intrinsic properties of the GPIbα-vWF tether bond define the kinetics of the platelet-type von Willebrand disease mutation. *Blood* 102:152-160.

[39] Chang, K.-C., and D.A. Hammer. 1999. The forward rate of binding of surface-tethered reactants: effect of relative motion between two surfaces. *Biophys J* **76**:1280-1292.

[40] Chen, S.Q., and T.A. Springer. 1999. An automatic braking system that stabilizes leukocyte rolling by an increase in selectin bond number with shear. *J Cell Biol* **144**:185-200.

[41] Zhang, X., D. F. Bogorin, and V. T. Moy. 2004. Molecular basis of the dynamic strength of the sialyl Lewis X-selectin interaction. *Chemphyschem* **5**:175-182.

[42] Zhao, Y., S. Chien, and S. Weinbaum. 2001. Dynamic contact forces on leukocyte microvilli and their penetration of the endothelial glycocalyx. *Biophys J* **80**:1124-1140.

[43] Evans, E.A. 2001. Probing the relation between force-lifetime-and chemistry in single molecular bonds. *Annu Rev Biophys Biomol Struct* **30**:105-128.

[44] Hammer, D.A. 2005. Leukocyte adhesion: what's the catch? *Curr Biol* **15**:R96-R99.

[45] Kishimoto, T.K., Jutila, M. A., and Butcher, E. C. 1990. Identification of a human peripheral lymph node homing receptor: a rapidly down-regulated adhesion molecule. *Proc Natl Acad Sci USA* **87**:2244-2248.

[46] Moore, K.L., Patel, K. D., Bruehl, R. E., Fugang, L., Johnson, D. A., Lichen- stein, H. S., Cummings, R. D., Bainton, D. F., and McEver, R. P. 1995. P-selectin glycoprotein ligand-1 mediates rolling of human neutrophils on P-selectin. *J Cell Biol* **128**:661-671.

[47] Bovin, N.V. 1998. Ployacrylamide-based glycoconjugates as tools in glycobiology. *Glycoconj J* **15**:431-446.

[48] Leppaen, A., T. Yago, V.I. Otto, R.P. McEver, and R.D. Cummings. 2003. Model glycosulfopeptides from P-selectin glycoprotein ligand-1 require tyrosine sulfation and a core 2-branched O-glycan to bind to L-selectin. . *J Biol Chem* **278**:26391-26400.

[49] Springer, T.A. 1995. Traffic signals on endothelium for lymphocyte recirculation and leukocyte emigration. *Ann Rev Physiol* **57**:827-872.

[50] Johnston, G.I., Cook, R. G., and McEver, R. P. 1989. Cloning of GMP-140, a granule membrane protein of platelets and endothelium: sequence similarity to proteins involved in cell adhesion and inflammation. *Cell* 56:1033-1044.

[51] Tedder, T.F.e.a. 1989. Isolation and chromosomal localization of cDNAs encoding a novel human lymphocyte cell surface molecule, LAM-1. Homology with the mouse lymphocyte homing receptor and other human adhesion proteins. *Journal of Experimental Medicine* 170:123-133.

[52] Yang, J., T. Hirata, K. Croce, G. Merrill-Skoloff, B. Tchernychev, E. Williams, R. Flaumenhaft, B.C. Furie, and B. Furie. 1999. Targeted gene disruption demonstrates that P-selectin glycoprotein ligand 1 (PSGL-1) is required for P-selectin-mediated but not E-selectin-mediated neutrophil rolling and migration. *J Exp Med* **190**:1769-1782.

[53] Sperandio, M., M.L. Smith, S.B. Forlow, T.S. Olson, L. Xia, R.P. McEver, and K. Ley. 2003. P-selectin glycoprotein ligand-1 mediates L-selectin-dependent leukocyte rolling in venules. *J Exp Med* **197**:1355-1363.

[54] Epperson, T.K., K.D. Patel, R.P. McEver, and R.D. Cummings. 2000. Noncovalent association of P-selectin glycoprotein ligand-1 and minimal determinants for binding to P-selectin. *J Biol Chem* **275**:7839-7853.

[55] Leppanen, A., S.P. White, J. Helin, R.P. McEver, and R.D. Cummings. 2000. Binding of glycosulfopeptides to P-selectin requires stereospecific contributions of individual tyrosine sulfate and sugar residues. *J Biol Chem* **275**:39569-39578.

[56] Leppanen, A., L. Penttil, O. Renkonen, R.P. McEver, and R.D. Cummings. 2002. Glycosulfopeptides with O-glycans containing sialylated and polyfucosylated polylactosamine bind with low affinity to P-selectin. *J Biol Chem* **277**:39749-39759.

[57] Leppanen, A., T. Yago, V.I. Otto, R.P. McEver, and R.D. Cummings. 2003. Model glycosulfopeptides from P-selectin glycoprotein ligand-1 require tyrosine sulfation and a core 2-branched O-glycan to bind to L-selectin. . *J Biol Chem* **278**:26391-26400.

[58] Leppanen, A., Mehta, P., Ouyang, Y.B., Ju, T., Helin, J., Moore, K.L., van Die, I., Canfield, W.M., McEver, R.P., and Cummings, R.D. 1999. A novel glycosulfopeptide binds to P-selectin and inhibits leukocyte adhesion to P-selectin. *J Biol Chem* 274:24838-24848.

[59] Rosen, S.D. 2004. Ligands for L-selectin: homing, inflammation, and beyond. *Annu Rev Immunol* **22**:129-156.

[60] Auton, M., A. A. Cruz, and J. L. Moake. 2006. Conformational stability and domain unfolding of the von Willebrand factor A domains. *J Mol Biol* 366:986-1000.

[61] Fuster, V., Badimon, L., Badimon, J.J., and Chesebro, J.H. 1992a. The pathogenesis of coronary artery disease and the acute coronary syndromes I. *N. Engl. J. Med.* 326:242-250.

[62] Fuster, V., Badimon, L., Badimon, J.J., and Chesebro, J.H. 1992b. The pathogenesis of coronary artery disease and the acute coronary syndromes II. *N. Engl. J. Med.* 326:310-318.

[63] Miller, J.L., and A. Castella. 1982. Platelet-type von Willebrand's disease: characterization of a new bleeding disorder. *Blood* 60:790-794.

[64] Miller, J.L., et al. 1991. Mutation in the gene encoding the alpha chain of platelet glycoprotein Ib in platelet-type von Willebrand disease. *Proc Natl Acad Sci U S A* 88:4761-4765.

[65] Tangelder, G.J., Slaaf, D.W., Arts, T., and Reneman, R.S. 1988. Wall shear rate in arterioles in vivo: least estimates from platelet velocity profiles. *Am. J. Physiol.* 254:H1059-H1064.

[66] Weiss, H.J. 1975. Platelet physiology and abnormalities of platelet function. *N. Engl. J. Med.* 293:580-588.

[67] Dumas, J.J., R. Kumar, T. McDonagh, F. Sullivan, M. L. Stahl, W. S. Somers, L. Mosyak. 2004. Crystal structure of the wild-type von Willebrand factor A1-glycoprotein Ibalpha complex reveals conformation differences with a complex bearing von Willebrand disease mutations. *J. Biol. Chem.* 279:23327-23334.

[68] Huizinga, E.G., Tsuji, S., Romijn, R.A., Schiphorst, M.E., de Groot, P.G., Sixma, J.J., and Gros, P. 2002. Structures of glycoprotein Ibα and its complex with von Willebrand factor A1 domain. *Science* 297:1176-1179.

[69] Berndt, M.C., Shen, Y., Dopheide, S.M., Gardiner, E.E., and Andrews, R.K. 2001. The vascular biology of the glycoprotein Ib-IX-V complex. *Thromb Haemost* 86:178-188.

[70] Nachman, R., R. Levine, E. A. Jaffe. 1977. synthesis of factor VIII antigen by cultured guinea pig megakaryocytes. *J. Clin. Invest.* 60:914-921.

[71] Yamamoto, K., V. De Waard, C. Fearns, D. J. Loskutoff. 1998. Tissue distribution and regulation of murine von Willebrand factor gene expression in vivo. *Blood* 92:2791-2801.

[72] Sadler, J.E. 1998. Biochemistry and genetics of von Willebrand factor. *Annu. Rev. Biochem.* 67:395-424.

[73] Wagner, D.D., J. B. Olmsted, V. J. Marder. 1982. Immunolocalization of von Willebrand protein in Weibel-Palade bodies of human endothelial cells. *J. Cell Biol.* 95:355-360.

[74] Moake, J.L. 1998. von Willebrand factor in the pathophysiology of thrombotic thrombocytopenic purpura. *Clin. Lab Sci.* 11:362-364.

[75] Wagner, D.D. 1990. Cell biology of von Willebrand factor. *Annu. Rev. Cell Biol.* 6:217-246.

[76] Dong, J.F., M. C. Berndt, A. Schade, L. V. McIntire, R. K. Andrews, J. A. Lopez. 2001. Ristocetin-dependent, but not botrocetin-dependent, binding of von Willebrand factor to the platelet glycoprotein Ib-IX-V complex correlates with shear-dependent interactions. *Blood* 97:162-168.

[77] Matsuhita, T., J. E. Sadler. 1995. Identification of amino acid residues essential for von Willebrand factor binding to platelet glycoprotein Ib. *J. Biol. Chem.* 270:13406-13414.

[78] Budde, U., R. Schneppenheim. 2001. von Willebrand Factor and von Willebrand Disease. *Rev.Clin.Exp.Hematol.* 5:335-368.

[79] Ginsburg, D., J. E. Sadler. 1993. von Willebrand disease: a database of point mutations, insertions, and deletions. For the Consortium on von Willebrand Factor Mutations and Polymorphisms, and the Subcommittee on von Willebrand Factor of the Scientific and Standardization Committee of the International Society on Thrombosis and Haemostasis. *Thromb. Haemost.* 69:177-184.

[80] Ruggeri, Z.M., R. Lombardi, L. Gatti, R. Bader, C. Valsecchi, T. S. Zimmerman. 1982. Type IIB von Willebrand's disease: Differential clearance of endogenous versus transfused large multimer von Willebrand Factor. *Blood* 60:1453-1456.

[81] Celikel, R., Ruggeri, Z. M., and Varughese, K. I. 2000. Modulation of von Willebrand factor conformation and adhesive function by an internalized water molecule. *Nat Struct Biol* 7:881-884.

[82] Kroll, M.H., J. D. Hellums, L. V. McIntire, A. I. Schafer, and J. L. Moake. 1996. Platelets and shear stress. *Blood*:1525-1541.

[83] Fredrickson, B.J., J. F. Dong, L. V. McIntire, and J. A. Lopez. 1998. Shear-dependent rolling on von Willebrand factor of mammalian cells expressing the platelet glycoprotein Ib-IX-V complex. *Blood* 92:3684-3693.

[84] Doggett, T.A., G. Giridhar, A. Lawshe, D. W. Schmidtke, I. J. Laurenzi, S. L. Diamond, T. G. Diacovo. 2002. Selectin-like kinetics and biomechanics promote rapid platelet adhesion in flow: the GPIbα-vWF tether bond. *Biophys. J.* 83:194-205.

[85] Federici, A.B., P. M. Mannucci, F. Stabile, M. T. Canciani, N. DiRocco, S. Miyata, J. Ware, and Z. M. Ruggeri. 1997. A type 2b von Willebrand disease mutation (Ile546 3 Val) associated with an unusual phenotype. *Thromb Haemost* 78:1132-1137.

[86] Kumar, R.A., J. F. Dong, J. A. Thaggard, M. A. Cruz, J. A. Lopez, L. V. McIntire. 2003. Kinetcs of GPIbα-vWF-A1 tether bond under flow: effect of GPIbα mutations on the association and dissociation rates. *Biophys. J.* 85:4099-4109.

[87] Miura, S., C. Q. Li, Z. Cao, H. Wang, M. R. Wardell, J. E. Sadler. 2000. Interaction of von Willebrand factor domain A1 with platelet glycoprotein Ib α-(1-289): slow intrinsic binding kinetics mediate rapid platelet adhesion. *J. Biol. Chem.* 275:7539-7546.

[88] Luca, M.D., Facey D. A., Favaloro E. J., Hertzberg M. S., Whisstock J. C., McNally T., Andrews R. K., and Berndt M. C. 2000. Strcture and function of the von Willebrand factor A1 domain: analysis with monoclonal antibodies reveals distinct binding sites involved in recognition of the platelet membrane glycoprotein Ib-IX-V complex and ristocetin-dependent activation. *Blood* 95:164-172.

[89] Lankhof, H., Damas, C., Schiphorst, M.E., MJ, I.J., Bracke, M., Sixma, J.J., Vink, T., and de Groot, P.G. 1997. Functional studies on platelet adhesion with recombinant von Willebrand factor type 2B mutants R543Q and R543W under conditions of flow. *Blood* 89:2766-2772.

[90] Yago, T., Zarnitsyna, V.I., Klopocki, A.G., McEver, R.P., and Zhu, C. 2007. Transport governs flow-enhanced cell tethering through L-selectin at threshold shear. *Biophys J* **92**:330-342.

[91] Ulrichts, H., *et al.* 2006. Shielding of the A1 domain by the D'D3 domains of von Willebrand factor modulates its interaction with platelet glycoprotein Ib-IX-V. *J Biol Chem* **281**:4699-4707.

[92] Siedlecki, C.A., B. J. Lestini, K. K. Kottke-Marchant, S. J. Eppell, D. L. Wilson, and R. E. Marchant. 1996. Shear-dependent changes in the three-dimensional structure of human von Willebrand factor. *Blood* 88:2939-2950.

[93] Moake, J.L., and Chow, T.W. 1998. Increased von Willebrand factor (vWf) binding to platelets associated with impaired vWf breakdown in thrombotic thrombocytopenic purpura. *J Clin Apher* **13**:126-132.

[94] Hulstein, J.J., *et al.* 2005. A novel nanobody that detects the gain-of-function phenotype of von Willebrand factor in ADAMTS13 deficiency and von Willebrand disease type 2B. *Blood* **106**:3035-3042.

[95] Ruggeri, Z.M., Pareti, F.I., Mannucci, P.M., Ciavarella, N., and Zimmerman, T.S. 1980. Heightened interaction between platelets and factor VIII/von Willebrand factor in a new subtype of von Willebrand's disease. *N Engl J Med* **302**:1047-1051.

[96] Romo, G.M., J.F. Dong, A.J. Schade, E.E. Gardiner, G.S. Kansas, C.Q. Li, L.V. McIntire, M.C. Berndt, and J.A. Lopez. 1999. The glycoprotein Ib-IX-V complex is a platelet counterreceptor for P-selectin. *J Exp Med* **190**:803-813.

[97] Tao, Z., *et al.* 2005. Recombinant CUB-1 domain polypeptide inhibits the cleavage of ULVWF strings by ADAMTS13 under flow conditions. *Blood* **106**:4139-4145.

[98] Phillips, J.C., *et al.* 2005. Scalable molecular dynamics with NAMD. *J Comput Chem* **26**:1781-1802.

[99] MacKerell, A.D., Jr., *et al.* 1998. All-atom empirical potential for molecular modeling and dynamics studies of proteins. *J Phys Chem B* **102**:3586-3616.

[100] Ajzenberg, N., Ribba A.-S., Rastegar-Lari G., Meyer D., and Baruch D. 2000. Effect of recombinant von Willebrand factor reproducing type 2B or type 2M mutations on shear-induced platelet aggregation. *Blood* 95:3796-3803.

[101] Zanardelli, S., Crawley, J.T., Chion, C.K., Lam, J.K., Preston, R.J., and Lane, D.A. 2006. ADAMTS13 substrate recognition of von Willebrand factor A2 domain. *J Biol Chem* 281:1555-1563.

[102] Zheng, X., D. Chung, T. K. Takayama, E. M. Majerus, J. E. Sadler, and K. Fujikawa. 2001. Structure of von Willebrand factor-cleaving protease (ADAMTS13), a metalloprotease involved in thrombotic thrombocytopenic purpura. *J Biol Chem* 276:41059-41063.

[103] Majerus, E.M., P. J. Anderson, and J. E. Sadler. 2005. Binding of ADAMTS13 to von Willebrand factor. *J Biol Chem* 280:21773-21778.

[104] Zhang, W., Motto, D., and Ginsburg, D. 2004. ADAMTS13 Binds VWF Via its C-Terminal CUB2 Domain. *ASH Annual Meeting Abstracts* 104:126-.

[105] Nishio, K., Anderson P. J., Zheng X. L., Sadler J. E. 2004. Binding of platelet glycoprotein Ibalpha to von Willebrand factor domain A1 stimulates the cleavages of the adjacent domain A2 by ADAMTS13. *Proc Natl Acad Sci U S A* 101:10578-10583.

[106] Gao, W., Anderson, P.J., Majerus, E.M., Tuley, E.A., and Sadler, J.E. 2006. Exosite interactions contribute to tension-induced cleavage of von Willebrand factor by the antithrombotic ADAMTS13 metalloprotease. *Proc Natl Acad Sci U S A* 103:19099-19104.

[107] Minghetti, L. 2007. Role of COX-2 in inflammatory and degenerative brain diseases. *Subcell Biochem* 42:127-141.

[108] Ferrario, C.M. 1998. Angiotension-(1-7) and antihypertensive mechanisms. *J Nephrol* 11:278-283.

[109] Tsai, H.M. 1996. Physiologic cleavage of von Willebrand factor by a plasma protease is dependent on its conformation and requires calcium ion. *Blood* 87:4235-4244.

[110] Furlan, M., Robles R., Lammle B. 1996. Parital purification and characterization of a protease from human plasma cleaving von Willebrand factor to fragments produced by in vivo proteolysis. *Blood* 87:4223-4234.

[111] Dong, J.F., Whitelock J., Bernardo A., Ball C., Cruz M. A. 2004. Variations among normal individuals in the cleavage of endothelial-derived ultra-large von Willebrand factore under flow. *J Thromb Haemost* 2.

[112] Cruz, M.A., Whitelock J., Dong J. F. 2003. Evaluation of ADAMTS-13 activity in plasma using recombinant von Willebrand Factor A2 domain polypeptide as substrate. *Thromb Haemost* 90:1204-1209.

[113] Whitelock, J.L., Nolasco L., Bernardo A., Moake J., Dong J. F., Cruz M. A. 2004. ADAMTS-13 activity in plasma is rapidly measured by a new ELISA method that uses recombinant VWF-A2 domain as substrate. *J Thromb Haemost* 2:485-491.

[114] Tsai, H.M., Sussman, II, and R. L. Nagel. 1994. Shear stress enhances the proteolysis of von Willebrand factor in normal plasma. *Blood* 83:2171-2179.

[115] Long, M., H. Zhao, K. S. Huang, and C. Zhu. 2001. Kinetic measurements of cell surface E-selectin/carbohydrate ligand interactions. *Ann Biomed Eng* 29:935-946.

[116] Zhu, C., M. Long, and P. Bongrand. 2002. Measuring receptor/ligand interaction at the single bond level: experimental and interpretive issues. *Ann Biomed Eng* 30:305-314.

[117] Martin, C., Morales, L.D., and Cruz, M.A. 2007. Purified A2 domain of von Willebrand factor binds to the active conformation of von Willebrand factor and blocks the interaction with platelet glycoprotein Ibalpha. *J Thromb Haemost* 5:1363-1370.

[118] Wiita, A.P., Perez-Jimenez R., Walther K. A., Grater F., Berne B. J., Holmgren A., Sanchez-Ruiz J. M., and Fernandez J. M. 2007. Probing the chemistry of thioredoxin catalysis with force. *Nature* 450:124-127.

[119] Li, H.B.L., W. A.; Oberhauser, A. F.; Carrion-Vazquez, M.; Kerkvliet, J. G.; Lu, H.; Marszalek, P. E.; Fernandez, J. M. 2002. Reverse engineering of the giant muscle protein titin. *Nature* 418:998-1002.

[120] Lou, J., and Zhu, C. 2007. A structure-based sliding-rebinding mechanism for catch bonds. *Biophys J* 92:1471-1485.

[121] Zhu, C., and McEver, R.P. 2005. Catch bonds: physical models and biological functions. *Mol Cell Biomech* 2:91-104.

[122] Dong, J.F., Moake, J.L., Nolasco, L., Bernardo, A., Arceneaux, W., Shrimpton, C.N., Schade, A.J., McIntire, L.V., Fujikawa, K., and Lopez, J.A. 2002. ADAMTS-13 rapidly cleaves newly secreted ultralarge von Willebrand factor multimers on the endothelial surface under flowing conditions. *Blood* 100:4033-4039.